The Role of the Equation of State in Core-Collapse Supernovae, Neutron Stars and their Mergers

A dissertation presented to

the faculty of

the College of Arts and Sciences of Ohio University

In partial fulfillment

of the requirements for the degree

Doctor of Philosophy

Sudhanva S. Lalit

August 2019

This dissertation titled

The Role of the Equation of State in Core-Collapse Supernovae, Neutron Stars and their Mergers

by

SUDHANVA S. LALIT

has been approved for

the Department of Physics and Astronomy

and the College of Arts and Sciences by

Madappa Prakash

Professor of Physics and Astronomy

Florenz Plassmann

Dean of the College of Arts and Sciences

Abstract

LALIT, SUDHANVA S., Ph.D., August 2019, Physics

The Role of the Equation of State in Core-Collapse Supernovae, Neutron Stars and their Mergers (185 pp.)

Director of Dissertation: Madappa Prakash

The equation of state (EOS) of dense matter is a crucial input in simulations of core-collapse supernovae, evolution of neutron stars from their birth to old age and binary neutron star mergers. The EOS is required over wide ranges of density and temperature, as well as under conditions in which neutrinos are trapped, and in the presence of intense magnetic field, and rapid differential and subsequent rigid rotation. In the three research projects included in this dissertation, I have made several advances in the EOS modeling.

In the first project, I employed the formalism of next-to-leading order Fermi Liquid Theory to calculate the thermal properties of symmetric nuclear and pure neutron matter. The advantage here is that only the single-particle energy spectrum at zero temperature is required to calculate the thermal properties under conditions of high degeneracy. The method was applied to a relativistic many-body theory beyond the mean field level which includes exchange (two-loop) effects. For all thermal variables, the semi-analytical next-to-leading order corrections reproduced results of the exact numerical calculations for entropies per baryon up to $2k_B$, where k_B is the Boltzmann constant. Excellent agreement was found down to subnuclear densities for temperatures up to 20 MeV. In addition to gaining physical insights, a rapid evaluation of the EOS in the homogeneous phase of hot and dense matter was achieved through the use of the zero-temperature Landau effective mass function and its derivatives.

The second project I was a part of was concerned with neutron star mergers, the first of which in the observed astronomical event termed GW170817 [A$^+$17c] has been recently reported through the detection of gravitational waves. Here, a critical assessment

of the current status of dense matter theory was made. In addition, I and my collaborators have pointed out the successes and limitations of the approaches currently in use along with suggestions made for improvements in several areas. The new development in this project was the generalization of the excluded volume approach to include multiple clusters such as deuteron (d), triton (^{3}H) and helium-3 (^{3}He) in addition to α-particles previously considered. This inclusion is necessary to properly account for electron capture and neutrino scattering in subnuclear-density matter as observable signals are formed in this region. The role of trapped neutrinos, magnetic fields and rotation (rigid and differential) were also highlighted in this work.

The third project addressed the issue of the hadron-to-quark transition within neutron stars. First principle calculations of this transition are not yet available, hence several scenarios such as first- and second-order phase transitions and crossover transitions have been explored in the literature. In this work, a detailed comparative study was performed by examining the results pertaining to neutron structure; that is, the masses and radii of neutron stars which depend on the treatment of the transition employed. Hadronic EOSs consistent with the nuclear systematics at nuclear densities were employed and several models of the quark matter EOS were explored. In all cases, consistency with the observational constraints provided by well-measured neutron star masses, estimates of radii from x-ray observations and bounds on tidal deformations set by the recent gravitational wave detection in GW170817 was sought. This work has enabled us to identify the class of EOSs in both the hadronic and quark sectors as well as specify the conditions in which one or the other treatment of the transition to quark matter may be appropriate.

The published papers stemming from the first two projects and the manuscript of the third project submitted for publication are reproduced verbatim in this thesis. The abstracts and contents therein provide additional technical details.

Dedication

To my parents

Rekha Lalit and Shriram Lalit,

who taught me the difference between

knowledge and education.

Acknowledgements

In the past six years, I have worked towards my Ph.D. in Physics. I have had many ups and downs during this journey. I was fortunate to have mentors, friends, and family who supported me throughout.

First and foremost, I express deep gratitude to Dr. Madappa Prakash who has been my research adviser, mentor and a source of inspiration. Thank you very much for all of your time and effort in teaching me so much and for all of your advice. I thank Dr. Constantinos Constantinou in particular, for his invaluable help throughout the years, and also Md. Abdullah Al Mamun and Dr. Sophia Han for their contributions to parts of this work. I extend my gratitude to former and present members of the nuclear theory group for helpful discussions. I am very grateful to my dissertation advisory committee members: Dr. Alexander Neiman, Dr. Hee-Jong Seo, and Dr. Jessica White. I very much appreciate their time and guidance.

I would also like to thank Dr. Zach Meisel for providing me an opportunity to work with him in experimental/computational techniques in nuclear astrophysics and helping me learn more about the crust of neutron stars and accretion phenomena.

Special thanks are due to Drs. Akshay Vaghani, Kavita Mishra and Pratik Dhuvad for their support and encouragement. I would also like to thank Abhishek Hingrajiya, Kaushal Patel for all the help extended to me and my family. I extend my gratitude to my friends Dr. Javad Anjum, Proma Basu, Matthew Burrows, Dr. Rekam Giri, Martin Graham, Reza Katebi, Bhishan Poudel, Alexandra Semposki and Sneha Upadhyay who have made graduate life easier to deal with. Finally, I thank my siblings Smita, Dipti and Siddhartha, and my brother in law Kiran for their love and faith in my abilities.

This work was performed in part under the auspices of the U. S. Department of Energy under contract No. DE-FG02-93ER40756 with Ohio University.

Table of Contents

List of Tables

List of Figures

1 Introduction

The statement "We have tentatively suggested that the super-nova process represents the transition of an ordinary star into a neutron star" by Baade and Zwicky in 1934 [BZ34b] appeared in the literature soon after the discovery of the neutron by Chadwick in 1932 [Cha32]. Although several historical supernovae were known at the time [BZ34a], the interpretation that the regular radio pulses from PSR B1919+21 first observed by Jocelyn Bell were due a rotating neutron star was made by Hewish et al. in 1967 [HBP+68]. Since then, about 2700 pulsars have been discovered, many of which are in a binary system[1]. X-ray emission from many isolated neutron stars and also from those accreting mass from a companion star have also been observed [MDK+18], and are commonly used nowadays to shed light on the internal structure of a neutron star [PLPS04b].

The detection of neutrinos from supernova SN 1987A [H+87, KMS+87] has lent support the prescient statement made by Baade and Zwicky although the neutron star left behind in the wake of the explosion is still to be observed. Theoretical studies made prior to SN 1987A had indicated a burst of neutrinos to be emitted in the explosion as well as during the evolution of the proto-neutron star for about a minute [Wil85, Eps78]. Understanding the precise mechanism of the explosion of progenitor stars in the mass range 10-30 $M_\odot$ through a combination of microphysical (equation of state of hot and dense matter, electron and neutrino interactions in such environments, etc.) and macrophysical (general relativistic magento-hydrodynamics, rotation, etc.) effects has been an area of research that has received much attention recently [MDK+18].

An intimately related issue is the question "How were the elements heavier than iron, the most stable element in the periodic table, synthesized in our Universe?" Two suggestions for the astrophysical settings in which they could have been synthesized –

[1] For a catalogue of pulsars, see https://www.atnf.csiro.au/people/pulsar/psrcat/

through rapid capture of neutrons on nuclei – have been put forth: (i) the outer expanding layers of core-collapse supernovae [Wil85] and (ii) the ejected matter in binary mergers involving neutrons stars and black holes [LS74, LS76]. In the former case, the required conditions of entropy per baryon and the neutron-to-proton seed ratio have been difficult to achieve in simulations of core-collapse supernova evolution. The recent detection of electromagnetic signals in the binary neutron star merger GW170817 [A$^+$17c] and their interpretation has strongly suggested that the latter site could well be the site of heavy element nucleosynthesis.

The two basic characteristics of a neutron star are its gravitational mass and radius. Figure 1.1 shows the available data on masses to date. From the perspective of microphysics, the most massive stars observed play an important role as they provide a lower limit on the maximum gravitational mass of a neutron star. This limit also has bearing on the number of stellar mass black holes harbored in our Universe. The largest well-measured masses are $1.97 \pm 0.04\ M_\odot$ for PSR J1614-2330 [DPR$^+$10], $2.01 \pm 0.04\ M_\odot$ for PSR J034+0432 [AFW$^+$13], and more recently $2.17^{+0.23}_{-0.008}\ M_\odot$ (95.4% credibility) and $2.17^{+0.11}_{-0.10}\ M_\odot$ (68.3% credibility) for PSR J0740+6620 [C$^+$19]. Unfortunately, the radius of a neutron star for which the mass is well known is not yet available. From x-ray observations, estimates of radii for $1.4M_\odot$ have been inferred with the result $R_{1.4} \lesssim 13 \pm 1$ km [GGR19]. From a study of hot spots on neutron stars for which the masses are known, x-ray observations utilizing NASA's NICER mission are expected to yield $R_{1.4}$ at a 5-10% level [ML16, Mil16].

Combining the electromagnetic (EM) [A$^+$17a] and gravitational wave (GW) information from the binary neutron star merger GW170817, ref. [MM17] has provided constraints on the radius $R_{\rm ns}$ and maximum gravitational mass $M^g_{\rm max}$ of a neutron star:

$$\begin{aligned} M^g_{\rm max} &\lesssim 2.17 M_\odot\,, \\ R_{1.3} &\gtrsim 3.1 G M^g_{\rm max} \simeq 9.92\ {\rm km}\,, \end{aligned} \tag{1.1}$$

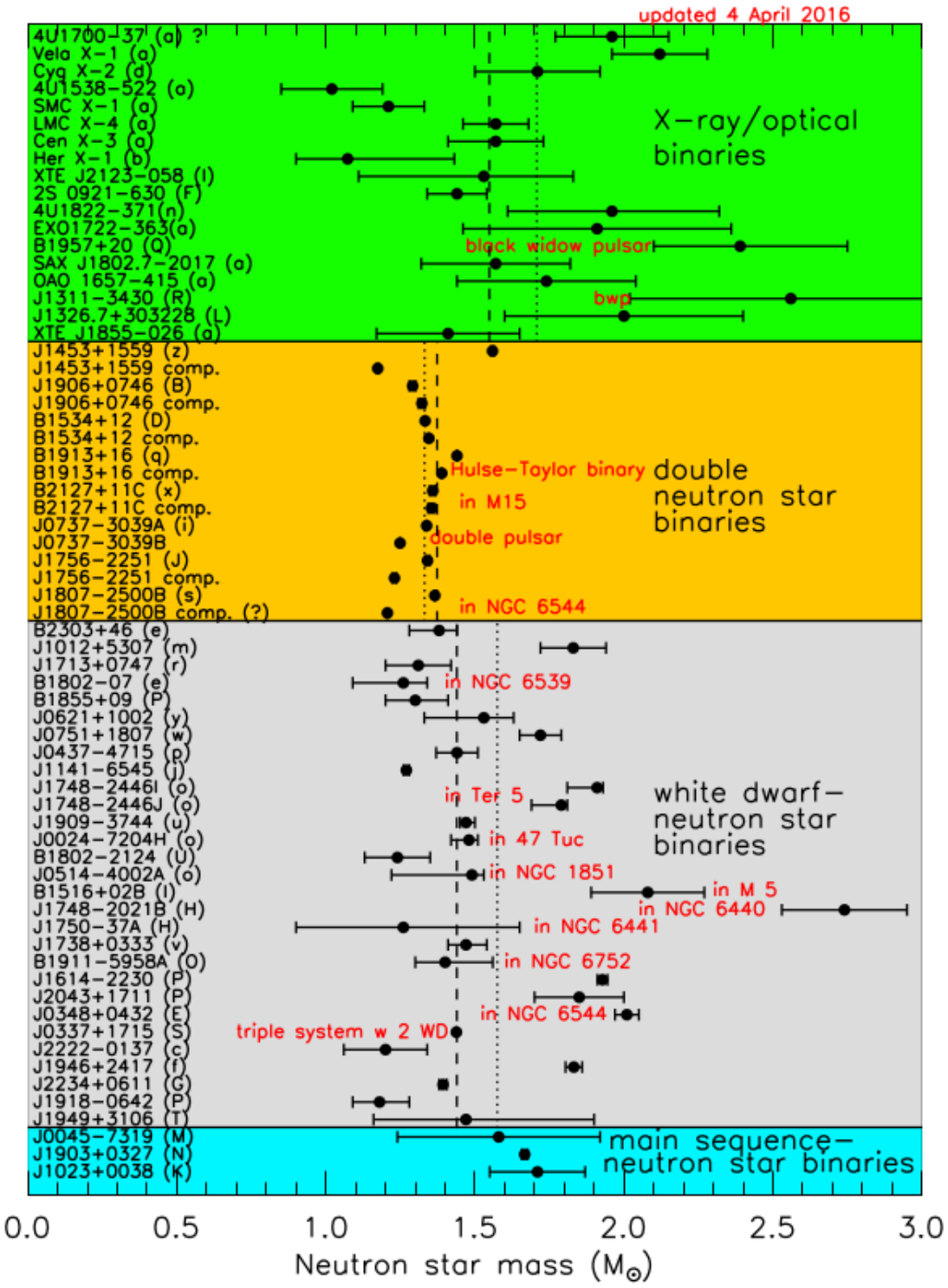

Figure 1.1: Neutron star gravitational masses. Figure taken from https://www.stellarcollapse.org/nsmasses maintained and updated by J. M. Lattimer.

where $R_{1.3}$ is the radius of a 1.3 $M_\odot$ neutron star and its numerical value above corresponds to $M^g_{\rm max} = 2.17\ M_\odot$. A recent reanalysis of the same data has yielded the much weaker constraint on $M^g_{\rm max} \lesssim 2.3 M_\odot$ [DFL$^+$18, Rai19].

The detection of gravitational waves from the merger GW170817 has also yielded bounds on the tidal deformations of the merging neutron stars during their inspiralling phase. With high accuracy, the chirp mass $\mathcal{M} = (m_1 m_2)^{3/5}/(m_1 + m_2)^{1/5}$, where $m_{1,2}$ are the masses of the merging neutron stars, was determined to be $\mathcal{M} = 1.186^{+0.001}_{-0.001} M_\odot$.

This event also revealed information on the binary tidal deformability,

$$\tilde{\Lambda} = \frac{16}{13} \frac{(m_1 + 12 m_2) m_1^4 \Lambda_1 + (m_2 + 12 m_1) m_2^4 \Lambda_2}{(m_1 + m_2)^5}. \tag{1.2}$$

For each star, the tidal deformability (or induced quadrupole polarizability) is given by [Lov09]

$$\Lambda_{1,2} = \frac{2}{3} k_2^{1,2} \left(\frac{R_{1,2}\, c^2}{G\, m_{1,2}} \right)^5 , \tag{1.3}$$

where the dimensionless Love number $k_2^{1,2}$ depends on the structure of the star, and therefore on the mass. Here, G is the gravitational constant, and $R_{1,2}$ are the radii. The high sensitivity of $\Lambda(M)$ to the radius of the star makes it a valuable constraining tool. For GW170817, the bounds placed were: $\tilde{\Lambda}(\mathcal{M} = 1.186^{+0.001}_{-0.001} \mathrm{M}_\odot) = 300^{+420}_{-230}$ for low-spin priors (using a 90% highest posterior density interval). Furthermore, by assuming a linear expansion of $\Lambda(M)$, which holds fairly well for normal stars without sharp transitions, limits on the dimensionless tidal deformability of a 1.4 $\mathrm{M}_\odot$ NS were updated in ref. [A$^+$19]: $70 \leq \Lambda_{1.4} \leq 580$ for low spin priors (at 90% confidence level). If future merger events yield better accuracy on $\Lambda(M)$, the potential exists to constrain the radii of the neutron stars involved more firmly.

Importance of the equation of state of hot and dense matter

Simulations of astrophysical phenomena, such as core-collapse supernovae, evolution of neutron stars from their birth to old age and binary mergers of compact stars in which

gravitational waves are emitted, involve general relativistic hydrodynamics and neutrino transport with special relativistic effects. Convection, turbulence, magnetic fields, etc., also play crucial roles. The macroscopic evolution in each case is governed by microphysics involving strong, weak and electromagnetic interactions. Central to an understanding of the above astrophysical phenomena is the equation of state (EOS) - the relationship between the pressure $P(n)$ vs energy density $\epsilon(n)$ - of matter as a function of baryon density, n, temperature, T, and lepton fraction, $Y_{L\ell}$. The EOS is as an integral part of hydrodynamical evolution, and also controls electron capture and neutrino interactions in ambient matter.

In this thesis, we explore regions having densities as low as $10^{-4} n_0$ to as high as 8-10 n_0, where $n_0 = 0.16 \pm 0.01$ fm^{-3} is the equilibrium density of isospin symmetric nuclear matter. The density region can be divided into (i) sub-nuclear densities ($n \lesssim 0.1$ fm^{-3}) (ii) near-nuclear densities ($n \gtrsim 0.1$ fm^{-3}) and (iii) supra-nuclear densities ($n \gtrsim 0.32$ fm^{-3}). For sub-nuclear densities and temperatures $T \lesssim 20$ MeV, different inhomogeneous phases are encountered. A homogeneous phase of nucleonic and leptonic matter is encountered at near ($n \gtrsim 0.1 - 0.32$ fm^{-3}) at all temperatures. With progressively increasing density, homogeneous matter may contain quark matter and Bose condensates. Table 1 summarizes the physical conditions encountered in each of the phenomena mentioned above [LP16].

The research work presented in this thesis is aimed at making advances in the calculation of the EOS of relevance to core-collapse supernovae, evolution of neutron stars and binary mergers involving neutron stars. Two of the three completed projects have been published in peer-reviewed journals, while the third one has been submitted for publication:

1. “Thermal effects in dense matter beyond mean field theory”, C. Constantinou, S. Lalit and M. Prakash, *Int. Jl. of Mod. Phys. E*, **26**, 174005 (2016); also reproduced

Table 1.1: Ranges of baryon number density n, temperature T , net electron fraction $Y_e = n_e/n$, and entropy per baryon S encountered in the indicated astrophysical phenomena.

	Core-collapse supernovae	Proto-neutron stars	Mergers of compact binary stars
n/n_0	$10^{-8} - 10$	$10^{-8} - 10$	$10^{-8} - 10$
T(MeV)	0 – 30	0 – 50	0 – 100
Y_e	0.35 – 0.45	0.01 – 0.3	0.01 – 0.6
$S\,(k_B)$	0.5 – 10	0 – 10	0 – 100

as a chapter for Gerry Brown's 90th Birthday Memorial Book,"Quarks, Nuclei and Stars," World Scientific, (2016),

2. "Dense matter equation of state for neutron star mergers, S. Lalit, M. A. A. Mamun, C. Constantinou, and M. Prakash, *Eur. Phys. J. A*, **55** 10, (2009), and

3. "Treating quarks within neutron stars", S. Han, M. A. A. Mamun, S. Lalit, C. Constantinou, and M. Prakash, submitted to *Phys. Rev. D*, http://arxiv.org/abs/1906.04095.

The organization of this thesis is as follows. The above three projects each form a chapter along with a brief introduction. The published papers are reproduced verbatim as they appear in the journals and in its submitted form for project 3. Each chapter ends by noting the specific contributions made by me.

In chap. 2, thermal effects in dense matter are studied utilizing the next-to-leading order Fermi Liquid Theory developed in refs. [BP91, CMPL15b]. The analytical formulas developed in this work yield results in excellent agreement with the exact numerical calculations [ZP16] of thermal effects (entropy per baryon of up to $2k_B$ of relevance to

core-collapse supernovae and proto-neutron stars) in a field-theoretical model that goes beyond mean field theory with the inclusion of exchange (two-loop) effects.

Chapter 3 contains a critical assessment of the sweet and sour points of the various approaches adopted in the literature to calculate the EOS relevant for core-collapse supernovae and mergers of neutron stars. The new element of this work is the generalization of the commonly used excluded volume approach [LS91] with only α-particles in the subnuclear region to include multiple clusters of light nuclei such as d, ^{3}H, and ^{3}He and ^{4}He. Their inclusion significantly affects electron capture and neutrino scattering processes at sub-nuclear (low) densities and hence the observable signals. This chapter also points out the effects of trapped neutrinos, magnetic fields and rotation (rigid and differential) in the remnants of neutron star mergers.

On the physical basis that quarks, the elementary particles that are confined within hadrons (baryons and mesons) at low densities, may be liberated at supra-nuclear densities within neutron stars was first suggested by Collins and Perry [CP75]. A detailed comparison of the various approaches taken to treat the hadron-to-quark transitions (first- and second-order phase transitions and crossover transitions) in the literature is made in Chap. 4. Special emphasis is placed on the calculated results in view of the observational constraints imposed by the lower limit of $\simeq 2M_\odot$ for the gravitational mass of a neutron star as well as the bounds placed on the tidal deformability of binary neutron stars via the merger event GW170817.

An outlook into extensions of the work performed in this thesis is provided in Chap. 5.

2 Thermal Effects in Dense Matter Beyond Mean Field Theory

The content of this chapter is largely drawn from the peer reviewed, published paper "Thermal effects in dense matter beyond mean field theory" [CLP17a, CLP17b], which will be reproduced verbatim in this chapter after an introduction to Mean Field theory and Landau's Fermi Liquid theory. My specific contributions to this paper will be detailed at the end of this chapter.

2.1 Mean Field Theory

A challenge encountered in many areas of physics is the problem of understanding the properties of many-body systems possessing large or infinite numbers of degrees of freedom. The calculation of the ground state (or zero temperature) properties of a many-body system (often referred to as a homogeneous or bulk system), such as its energy, pressure, spin susceptibility, etc., becomes a formidable task when non-trivial interactions are present between its constituents. Examples of exact solutions, such as for the one-dimensional Ising model with spin-spin interactions [LL80a], are rare. In view of its complexity, various approximation schemes at increasing levels of complexity have been devised [LL80a, PB11].

In the context of dense matter physics, both non-relativistic potential and relativistic field theoretical models have been developed to calculate properties of the ground state and thermally excited states of matter. As the calculations are organized (seemingly) differently in each of these approaches, a brief introduction is given below to highlight the strategies adopted. Details of the latter approach, which is used to demonstrate the application of the next-to-leading order Fermi Liquid Theory (see Sec. 2.4), is contained in the published paper mentioned above and is reproduced in Sec. 2.5.

2.1.1 Potential Models

In first approximation, the effect of all the other particles on any given particle is approximated by a single averaged effect, the so-called mean field. Interactions are included by arranging them in clusters whereby two-body, three-body, etc., interactions are counted and treated separately. This procedure reduces the many-body problem to solving a one-body problem [Neg82], albeit with a complicated average interaction whose form depends on the interaction with the clusters. Spin and isospin dependent short-ranged interactions (such as strong interactions between nucleons) and long-ranged interactions (the Coulomb force, for example) introduce their own characteristic average or mean fields. The total effect, say for example on the ground state energy, is then obtained by summing over the effect on all the so-affected single particles in the system.

Hartree Approximation

The concept of the mean field is illustrated at its simplest level in the analysis by Hartree [Har28]. Here, the many-body wave function for a system of N non-relativistic particles (fermions or bosons) is represented by a product wave function

$$\Psi = u_1(\boldsymbol{r}_1)u_2(\boldsymbol{r}_2)\ldots u_N(\boldsymbol{r}_N)\,, \tag{2.1}$$

where each particle i is described by its own wave function $u_i(\boldsymbol{r}_i),\ i = 1, 2, \ldots, N$. The ground state energy of the system is then given by

$$\begin{aligned} E = \langle H\rangle &= \langle\Psi\,|H|\,\Psi\rangle \\ &= \sum_i \int d\mathcal{V}\; u_i^*(\boldsymbol{r})\left(-\frac{\hbar^2}{2m}\nabla^2\right)u_i(\boldsymbol{r}) \\ &+ \sum_{i<j}\int\int d\mathcal{V}_1 d\mathcal{V}_2\; V_{12}\,|u_i(\boldsymbol{r}_1)|^2\left|u_j(\boldsymbol{r}_2)\right|^2\,, \end{aligned} \tag{2.2}$$

where, $H = T + V_{12}$ is the total Hamiltonian, V_{12} denoting the pairwise interaction between two particles. The wave functions $u_i(\boldsymbol{r})$ are normalized to unity, but need not be orthogonal.

The ground state energy is then obtained using the variational principle [Sla28, Gau28]. Allowing arbitrary variations in the functions u_i and u_i^* in eq. (2.2), one obtains

$$-\frac{\hbar^2}{2m}\nabla^2 u_i + V_i u_i = \epsilon_i\, u_i, \qquad i = 1, 2, \ldots, N\,, \tag{2.3}$$

where the effective potential, or mean field, on particle i is

$$V_i(\boldsymbol{r}_1) = \sum_{j\neq i} \int d\mathcal{V}_2\, V_{12} \left|u_j(\boldsymbol{r}_2)\right|^2 \,. \tag{2.4}$$

The set of N Schroedinger equations in eq. (2.3) is known as the Hartree equation, which is solved for the u_i's and the energy eigenvalues ϵ_i's self-consistently. The self-consistent aspect of the procedure resides in the fact that the mean field $V_i(\boldsymbol{r}_1)$ depends on the densities of all other particles in the system. The total energy $E = \sum_i \epsilon_i$ is generally calculated by using initial guess trial wave functions, which are iteratively improved to obtain better estimates.

Hartree-Fock Approximation

The assumed product form of Ψ in eq. (2.1) does not include the effects of spin or of particle correlations since the wave function of particle i is u_i regardless of the position of the other particles. This omission of spin effects was rectified by Fock [Foc30a, Foc30b] resulting in the so-called the Hartree-Fock approach. Correlation effects are separately included by introducing correlation functions into the Hartree-Fock wave function Ψ. This wave function for an N-fermion system is anti-symmetric under the interchange of any

pair of particles and is written in the form of a Slater determinant:

$$\Psi = \frac{1}{(N!)^{1/2}} \begin{vmatrix} u_1(1) & u_1(2) & \dots & u_1(N) \\ u_2(1) & u_2(2) & \dots & u_2(N) \\ \vdots & & \ddots & \vdots \\ u_N(1) & u_N(2) & \dots & u_N(N) \end{vmatrix}, \tag{2.5}$$

where the single-particle wave functions in the determinant above are of the form

$$u_i(j) = u_i(\boldsymbol{r}_j)\,\chi_i(\sigma_j)\,. \tag{2.6}$$

The spinor $\chi(\sigma)$ is either χ_1 (spin-up) or χ_2 (spin-down) and is given by

$$\chi_1 = \begin{pmatrix} 1 \\ 0 \end{pmatrix}, \qquad \chi_2 = \begin{pmatrix} 0 \\ 1 \end{pmatrix}. \tag{2.7}$$

Unlike in the Hartree approach, the wave functions in eq. (2.6) are required to be orthonormal. The variational condition

$$\delta \langle \Psi | H | \Psi \rangle = 0 \tag{2.8}$$

yields the *Hartree-Fock* (HF) equations

$$\begin{aligned} \epsilon_i u_i(\boldsymbol{r}_1) &= -\frac{1}{2}\nabla^2 u_i(\boldsymbol{r}_1) + V_i(\boldsymbol{r}_1) u_i(\boldsymbol{r}_1) \\ &- \int d\mathcal{V}_2\, U(\boldsymbol{r}_1, \boldsymbol{r}_2) u_i(\boldsymbol{r}_2) \end{aligned} \tag{2.9}$$

where,

$$V_i(\boldsymbol{r}_1) = \sum_{j \neq i} \int d\mathcal{V}_2\, V_{12}(\boldsymbol{r}_{12}) \left| u_j(\boldsymbol{r}_2) \right|^2 \tag{2.10}$$

is the effective local potential for the i^{th} particle and

$$\begin{aligned} U(\boldsymbol{r}_1, \boldsymbol{r}_2) &= \sum_j \delta_{\sigma_i \sigma_j} V_{ij}\, u_j^*(\boldsymbol{r}_2) u_j(\boldsymbol{r}_1) \\ &= U^*(\boldsymbol{r}_2, \boldsymbol{r}_1) \end{aligned} \tag{2.11}$$

is the nonlocal potential generated by anti-symmetrization of the wave function.

In the case of the Yukawa potential, nonlocal term is half of the Hartree term and opposite in sign. The reason is that in the limit when the inter-particle separation is much larger than the interaction range, only particles with opposite spins can get close enough to interact by the Pauli exclusion principle. Thus the total interaction energy is half of what it would be without spin effects.

The physical effect of the exchange term is to lessen the role of particle interactions and thus to lower the energy for a repulsive force and increase the energy for an attractive force. Even so, HF terms cannot properly account for *additional correlations* between fermions. Such correlations are generally included by modifying the trial wave functions to contain effects of correlations beyond those of anti-symmetrization (e.g. Jastrow wave functions that incorporate short-range correlations [MS76, Jas55]). The parameters entering these correlation functions are optimized to yield the best possible estimate of the upper bound for the ground state energy.

Alternative approaches to the variational scheme described above have also been suggested and used to solve the many-body problem exactly given a Hamiltonian. An example of such an approach is the Green Function Monte Carlo method [Kal62]. These calculations are usually numerically intensive. A description of this method is beyond the scope of this work, but can be found in refs. [Kal62, And02].

2.1.2 Relativistic Field Theoretical Models

The starting point of field theories is the Lagrangian density $\mathcal{L}$ which specifies how the constituents of the system interact with one another. For baryons B, such as neutrons and protons, interacting via the exchange of mesons, such as $\pi, \sigma, \omega, \rho$, etc., $\mathcal{L}$ is generally written as

$$\mathcal{L} \equiv \mathcal{L}(B, \pi, \sigma, \omega, \rho) = \mathcal{L}_B(B, \pi, \sigma, \omega, \rho) + \mathcal{L}_{meson}(\pi, \sigma, \omega, \rho)\,, \tag{2.12}$$

where $\mathcal{L}_B$ contains terms involving the kinetic energies of the B fields and interactions of the B fields with the various meson fields. The structure of $\mathcal{L}_{meson}$ is similar, but involves only the individual meson fields. The source currents involve the fermion fields B and the mediators of interactions between the B fields involve the various boson (meson) fields. The values of the various fields are determined by the Euler-Lagrange equations of motion (EOM's)

$$\partial_\mu \frac{\partial \mathcal{L}}{\partial(\partial_\mu q)} = \frac{\partial \mathcal{L}}{\partial q}\,, \tag{2.13}$$

where q denotes any of the fields. In general, the EOMs couple the baryon source currents to the meson fields in a non-linear manner. In static (time independent), uniform and isotropic matter, these EOMs simplify considerably, but remain coupled which requires a self-consistent determination of the fields. The *mean field approximation* amounts to replacing all of the fluctuating fields q by their ground state expectation values $\langle q \rangle$. Having determined the values of the fields from the coupled non-linear EOM's, the energy density and pressure of the system is given by the diagonal elements of the energy-momentum tensor

$$T_{\mu\nu} = \frac{\partial \mathcal{L}}{\partial(\partial_\mu q)}\,\partial_\nu q - g_{\mu\nu}\,\mathcal{L}\,, \tag{2.14}$$

where $g_{\mu\nu}$ is the metric chosen.

In going *beyond the mean field approximation*, fluctuations of the various fields are included. This extension gives rise to what are termed as vacuum fluctuation energies, exchange energies, ring diagram energies, correlation energies, etc. Sec 2.5 details how the exchange energy contributions are calculated exactly at zero and finite temperatures T. This section also contrasts the exact numerical results with those of the next-to-leading order Fermi Liquid Theory (FLT) at finite T. In the following section, a brief review of FLT is presented.

2.2 Fermi Liquid Theory

Landau's Fermi-Liquid theory (FLT) [Lan57a, Lan57b] enables the determination of the low temperature properties of some interacting systems of fermions even when the calculation of its ground state (temperature $T = 0$) properties is difficult. Framed in terms of elementary excitations, the starting point of the theory is the one-to-one correspondence between the thermal excitations of an ideal (non-interacting) Fermi gas system and those of the corresponding interacting system. The states of the interacting system are obtained by adiabatically turning on particle-particle interactions between states of the noninteracting system. This process ensures that momentum and internal degrees of freedom such as spin and isospin remain good quantum numbers in the description of interacting particles, often called quasi-particles. The results for thermal variables, such as entropy, excitation energy, specific heat, thermal pressure, etc., so obtained agree with those obtained using many-body diagrammatic techniques.

The main application of the concept of elementary excitations in FLT is for non-superfluid Fermi systems under degenerate conditions when $T/T_F \ll 1$, where T_F is the Fermi temperature (or Fermi energy $\epsilon_F = k_B T_F$). Superfluid and/or superconducting systems involve collective modes and break the one-to-one correspondence essential in FLT. Under special circumstances in which the elementary excitation is deduced from measurements in the normal phase above the superfluid transition temperature, FLT techniques have been used to account for properties of superfluid ^{4}He. Here the elementary excitations are phonons (lattice vibrations) and rotons (see [BP91, LL80b, PN66] and references therein). In dilute solutions of ^{3}He in superfluid ^{4}He [BP91, PN66], both phonons and rotons, and ^{3}He quasiparticles become elementary excitations.

In the discussion below, the basic results of FLT are presented following closely the lucid exposition in [BP91]. This serves as an introduction to the material presented in the

next section where next-to-leading order FLT developed in ref. [CMPL15b] is applied to nucleonic matter encountered in astrophysical phenomena such as core-collapse supernovae, port-neutron stars and mergers of binary neutron stars.

By Pauli's exclusion principle, the ground state Ψ_0 of a Fermi gas consists of fermions occupying all momentum states corresponding to momentum $p < p_{\rm F}$, where p_F is the Fermi momentum, with all higher momentum states unoccupied. As the interaction is turned on adiabatically, the spin, charge and momentum of the fermions corresponding to the occupied states remain unchanged, while dynamical properties, such as their mass, magnetic moment etc. acquire new values. The one-to-one correspondence between the elementary excitations of the ideal (non-interacting) Fermi gas system and those of the interacting system assures that the number density n and entropy density s retain their ideal gas forms as for both quantities only counting the momentum (or wave number) and spin (and isospin in nucleonic systems) degrees of freedom is involved. Thus, for a single component gas of interacting particles, n and s are given by

$$n = \frac{1}{V}\sum_{k,\sigma} n_{k\sigma} \tag{2.15}$$

$$s = -\frac{1}{V}\sum_{k,\sigma}\left[n_{k\sigma}\log n_{k\sigma} + (1-n_{k\sigma})\log(1-n_{k\sigma})\right] \tag{2.16}$$

where

$$n_{k\sigma} = \frac{1}{e^{(\epsilon_{k\sigma}-\mu)/T}+1} \tag{2.17}$$

is the Fermi-Dirac distribution function, k is the wave number and σ counts the two spin projections for a spin-$\frac{1}{2}$ fermion. The quasi-particle density of states at $T = 0$ at the Fermi surface is given by

$$N(0) = \frac{1}{V}\sum_{k,\sigma}\delta(\epsilon^0_{k\sigma} - \epsilon_F) \tag{2.18}$$

where, $\epsilon^0_{k\sigma}$ is the energy spectrum at $T = 0$ and ϵ_F is the Fermi energy. Passing to the continuum limit,

$$N(0) = 2\int_0^{k_F} \frac{d^3k}{(2\pi)^3}\,\delta(\epsilon_k - \epsilon_F) = \frac{1}{\pi^2}\int_0^{\epsilon_F} dk\,k^2\delta(\epsilon_k - \epsilon_F) \tag{2.19}$$

$$\tag{2.20}$$

The properties of delta function,

$$\delta[g(x)] \;=\; \frac{\delta(x - x_0)}{|g'(x_0)|} \quad \text{and} \quad \int dx\, f(x)\,\delta(x - x_0) = f(x_0) \tag{2.21}$$

can now be used to get

$$N(0) \;=\; \frac{1}{\pi^2}\int_0^{\epsilon_F} dk\,k^2\frac{\delta(k - k_F)}{v_F} = \frac{k_F^2}{\pi^2 v_F}\,, \tag{2.22}$$

where

$$v_F = \left.\frac{\partial\epsilon^0_{k\sigma}}{\partial k}\right|_{k=k_F} \tag{2.23}$$

is the velocity at the Fermi surface.

From eq. (2.16), the variation of the entropy density, δs, takes the form

$$\delta s = \frac{1}{V}\sum_{k,\sigma}\delta n_{k\sigma}\left(\frac{\epsilon_{k\sigma} - \mu}{T}\right) \tag{2.24}$$

where

$$\delta n_{k\sigma} = \frac{\partial n_{k\sigma}}{\partial\epsilon_{k\sigma}}\left[-\left(\frac{\epsilon_{k\sigma} - \mu}{T}\right)\delta T + \delta\epsilon_{k\sigma} - \delta\mu\right] \tag{2.25}$$

To lowest order in temperature, use of Sommerfeld's expansion yields

$$\delta s = -\frac{1}{V}\sum_{k,\sigma}\frac{\partial n_{k\sigma}}{\partial\epsilon_{k\sigma}}\left(\frac{\epsilon_{k\sigma} - \mu}{T}\right)^2\delta T \tag{2.26}$$

In a small neighborhood of ϵ_F, the derivative $\frac{\partial n_{k\sigma}}{\partial\epsilon_{k\sigma}}$ is non-zero for small T ($T \ll \epsilon_F$) as the Fermi distribution function differs only slightly from a step-function. This restricts momenta in a narrow region around k_F to give

$$\delta s = -\delta T N(0)\int_{-\infty}^{\infty}\left(\frac{x}{e^x + 1}\right)^2 e^x dx \tag{2.27}$$

where

$$x = \frac{\epsilon - \mu}{T}. \tag{2.28}$$

The integral in (2.27) has the value $\frac{\pi^2}{3}$, so that

$$s = \frac{\pi^2}{3} N(0) T = 2anT \tag{2.29}$$

where a is the so-called level density parameter, and is given by

$$a = \frac{\pi^2}{2k_F v_F} = \frac{\pi^2 N(0)}{6n} \tag{2.30}$$

The other thermodynamic quantities, such as the chemical potential, free energy, thermal energy, pressure, etc., can be obtained from Maxwell relations [LL80a], and are summarized below.

The free energy, F, is the relevant thermodynamic potential as it captures the conflicting demands of minimum energy and maximum entropy. Explicitly,

$$F(E, T, S) = E - TS \tag{2.31}$$

From the thermodynamic identity, the energy functional is obtained by

$$E(S, V, N) = TS - pV + \sum_i \mu_i N_i \tag{2.32}$$

In differential form,

$$dF = -S\,dT - p\,dV + \sum_i \mu_i dN_i \tag{2.33}$$

$$\implies -\frac{dF}{dT} = S, \quad -\frac{dF}{dV} = p, \quad \frac{dF}{dN_i} = \mu_i. \tag{2.34}$$

Using the above relations, the thermal variables in the degenerate limit $T/T_F \ll 1$ for a multi-component system of fermions are:

- Thermal energy

$$E_{th} = \frac{T^2}{n} \sum_i a_i n_i\,, \tag{2.35}$$

- Thermal pressure

$$p_{th} = \frac{2nT^2}{3} \sum_i a_i \left(1 - \frac{3}{2} \frac{n}{m_i^*} \frac{dm_i^*}{dn}\right), \tag{2.36}$$

- Thermal chemical potentials

$$\mu_{ith} = -T^2 \left[\frac{a_i}{3} + \sum_j \frac{n_j a_j}{m_j^*} \frac{dm_j^*}{dn_i}\right]. \tag{2.37}$$

Note that effects of interactions enter in the various quantities above through the effective mass m^* and it's derivative with respect to density. When m^* is independent of density, the various expressions above resemble those of ideal gases but with $m \to m^*$.

Thermal Effects in Dense Matter Beyond Mean Field Theory

Constantinos Constantinou

Institute for Advanced Simulation, Institute für Kernphysik, and Jülich Center for Hadron Physics, Forschungszentrum Jülich, D-52425 Jülich, Germany

c.constantinou@fz-juelich.de

Sudhanva Lalit* and Madappa Prakash†

Department of Physics and Astronomy,

Ohio University, Athens, Ohio 45701, United States

**sl897812@ohio.edu*

†*prakash@ohio.edu*

Abstract

The formalism of next-to-leading order Fermi Liquid Theory is employed to calculate the thermal properties of symmetric nuclear and pure neutron matter in a relativistic many-body theory beyond the mean field level which includes two-loop effects. For all thermal variables, the semi-analytical next-to-leading

order corrections reproduce results of the exact numerical calculations for entropies per baryon up to 2. This corresponds to excellent agreement down to subnuclear densities for temperatures up to 20 MeV. In addition to providing physical insights, a rapid evaluation of the equation of state in the homogeneous phase of hot and dense matter is achieved through the use of the zero-temperature Landau effective mass function and its derivatives.

2.3 Introduction

Core-collapse supernovae, neutron stars from their birth to old age, and binary mergers involving neutron stars all pass through stages in which there are considerable variations in the baryon density, temperature, and lepton content. Simulations of these astrophysical phenomena involve general relativistic hydrodynamics and neutrino transport with special relativistic effects. Convection, turbulence, magnetic fields, *etc*., also play crucial roles. The macroscopic evolution in each case is governed by microphysics involving strong, weak and electromagnetic interactions. Depending on the baryon density n, temperature T, and the lepton content of matter (characterized by $Y_{Le} = n_{Le}/n$ when neutrinos are trapped or by the net electron concentration $Y_e = n_e/n$ in neutrino-free matter), various phases of matter are encountered. For sub-nuclear densities ($n \lesssim 0.1$ fm^{-3}) and temperatures $T \lesssim 20$ MeV, different inhomogeneous phases are encountered. A homogeneous phase of nucleonic and leptonic matter prevails at near- and supra-nuclear densities ($n \gtrsim 0.1$ fm^{-3}) at all temperatures. With progressively increasing density, homogeneous matter may contain hyperons, quark matter and Bose condensates.

Central to an understanding of the above astrophysical phenomena is the equation of state (EOS) of matter as a function of n, T, and Y_{Le} (or Y_e) as it is as an integral part of hydrodynamical evolution, and controls electron capture and neutrino interactions in ambient matter. The EOS of dense matter has been investigated in the literature

extensively, but for the most part those for use in the diverse physical conditions of relevance to astrophysical applications have been based on mean field theory in both non-relativistic potential or relativistic field-theoretical approaches. A recent article honoring Gerry Brown reviews the current status and advances made to date in the growing field of neutron star research [LP16].

The objective of this work is to assess the extent to which the model independent formalism of Fermi Liquid Theory (FLT) [BP91] is able to accurately describe thermal effects in dense homogeneous nucleonic matter under degenerate conditions for models beyond mean field theory (MFT). Recently, a next-to-leading order (NLO) extension of the leading-order FLT and its relativistic generalization in ref. [BC76b] was developed in ref. [CMPL15a]. The FLT+NLO formalism was applied to nonrelativistic potential models with contact and finite-range interactions as well as to relativistic models of dense matter at the mean field level in ref. [CMPL15a] . Excellent agreement with the results of exact numerical calculations for all thermal variables was found with the semi-analytical FLT+NLO results. In this contribution, we present similar excellent agreement with the exact numerical results of a relativistic field-theoretical model beyond the MFT level that includes two-loop (exchange) effects recently reported in ref. [ZP16]. The gratifying result is that the FLT+NLO formalism extends agreement with the exact numerical results for all n and T for which the entropy per baryon $S \leq 2k_B$. This means that, for $T \lesssim 20$ MeV, the method can adequately describe state variables down to a density of ~ 0.1 fm^{-3}. For densities below ~ 0.1 fm^{-3}, inhomogeneous phases occur for which a separate treatment is required. This development not only provides a check of time-consuming many-body calculations of dense matter at finite temperature, but also serves to accurately (and, to rapidly) calculate thermal effects from a knowledge of the zero-temperature single-particle spectra for S up to $2k_B$ for which effects of interactions are relatively important.

The organization of this contribution is as follows. In Sec. 2.4, we summarize the NLO formalism of FLT recently developed in ref. [CMPL15a]. Section 2.5 contains a brief description of the relativistic field-theoretical model that extends mean-field theory (MFT) to include two-loop (TL) effects as implemented in ref. [ZP16]. Working formulas required for the evaluation of the degenerate-limit thermal effects (in particular, expressions for the single particle spectra) are given in this section which also includes our results and associated discussion.

2.4 Next-to-Leading Order Fermi Liquid Theory

The thermodynamics of fermion systems entails evaluation of integrals of the type

$$I = \int_0^\infty dp\; g(p) \frac{1}{1+\exp\left[\frac{\epsilon(p,n)-\mu}{T}\right]}\,, \tag{2.38}$$

where T is the temperature, μ is the chemical potential, and ϵ is the single-particle spectrum of the underlying model. The functional form of $g(p)$ is particular to the state property in question. Equivalently, we can write

$$I = \int_0^\infty dy \frac{\phi(y)}{1+\exp(y-\eta)}\,, \tag{2.39}$$

where

$$y = \frac{\epsilon(p,n)-\mathcal{U}(n)}{T}\;,\;\; \eta = \frac{\mu-\epsilon(p=0,n)}{T} \tag{2.40}$$

$$\phi(y) = \frac{\mathcal{M}(p)Tg(p)}{p}\;,\;\; \mathcal{M}(p) = p\left(\frac{\partial\epsilon}{\partial p}\right)^{-1}\,. \tag{2.41}$$

Above, $\mathcal{U}(n)$ is inclusive of all those terms in the spectrum which depend only on the density n. The Landau effective mass function, $\mathcal{M}(p)$, and its derivatives with respect to momentum p play crucial roles in determining the thermal effects.

In the degenerate limit, characterized by large values of the parameter η, Sommerfeld's Lemma

$$I \xrightarrow{\eta\gg 1} \int_0^\eta \phi(y)\,dy + \frac{\pi^2}{6}\left.\frac{d\phi}{dy}\right|_{y=\eta} + \frac{7\pi^4}{360}\left.\frac{d^3\phi}{dy^3}\right|_{y=\eta} + \ldots \tag{2.42}$$

can be used for the approximate evaluation of such integrals. Truncation of the series at the first term recovers results for cold matter; the second term produces the familiar FLT corrections and the third term represents the next-to-leading order (NLO) extension to FLT. Owing to the asymptotic nature of the Sommerfeld formula, the expansion will, in general, diverge at higher orders unless all terms are retained.

The number density of single-species fermions with γ internal degrees of freedom in 3 dimensions is (throughout we use units in which $\hbar = 1$)

$$n = \frac{\gamma}{2\pi^2} \int dp \, \frac{p^2}{1 + \exp\left(\frac{\epsilon - \mu}{T}\right)} \,. \tag{2.43}$$

In the present context, we take n to be an independent variable as is appropriate for a system that does not exchange particles with an external reservoir but whose total volume is allowed to change. Thus

$$n(T = 0) = n(p_F) = \frac{\gamma p_F^3}{6\pi^2} = n(T) \simeq n(p_\mu) \,, \tag{2.44}$$

where p_F is the Fermi momentum and $n(p_\mu)$ is the result of eq. (2.43) evaluated according to eq. (2.42). Perturbative inversion of eq. (2.44) leads to

$$p_\mu = p_F \left[1 - \frac{\pi^2}{6} \frac{m^{*2} T^2}{p_F^4} \left(1 + \frac{p_F}{m^*} \left. \frac{d\mathcal{M}}{dp} \right|_{p_F} \right) + \ldots \right] , \tag{2.45}$$

where

$$m^* = \mathcal{M}(p = p_F) \tag{2.46}$$

is the Landau effective mass. The combination of eq. (2.45) with the Sommerfeld expansion of the entropy density, formally given by

$$s = -\frac{\gamma}{2\pi^2} \int dp \; p^2 \left\{ f(p) \ln f(p) + [1 - f(p)] \ln[1 - f(p)] \right\} \tag{2.47}$$

$$f(p) = \frac{1}{1 + \exp\left[\frac{\epsilon(p) - \mu}{T}\right]} \tag{2.48}$$

yields an expression for s in terms of quantities defined on the Fermi surface:

$$s = \frac{\gamma p_F m^* T}{6} - \frac{\gamma\pi^2}{15}\frac{m^{*3}T^3}{p_F^3}(1 - L_F) \tag{2.49}$$

$$= 2anT - \frac{16}{5\pi^2}a^3 nT^3(1 - L_F)\,, \tag{2.50}$$

where $a = \pi^2 m^*/(2p_F^2) = \pi^2/(4T_F)$ is the level density parameter with T_F denoting the Fermi temperature, and

$$L_F \equiv \frac{7}{12}\left(\frac{p_F}{m^*}\left.\frac{\partial\mathcal{M}}{\partial p}\right|_{p_F}\right)^2 + \frac{7}{12}\frac{p_F^2}{m^*}\left.\frac{\partial^2\mathcal{M}}{\partial p^2}\right|_{p_F} + \frac{3}{4}\frac{p_F}{m^*}\left.\frac{\partial\mathcal{M}}{\partial p}\right|_{p_F}\,. \tag{2.51}$$

Then the entropy per particle is the simple ratio $S = s/n$ whereas the thermal energy, pressure and chemical potential are obtained via Maxwell's relations (the integrals below are performed at constant density):

$$E_{th} = \int T\, dS = aT^2 - \frac{12}{5\pi^2}a^3T^4(1 - L_F) \tag{2.52}$$

$$P_{th} = -n^2\int \frac{dS}{dn}\, dT$$

$$= \frac{2}{3}anQT^2 - \frac{8}{5\pi^2}a^3 nQT^4\left(1 - L_F + \frac{n}{2Q}\frac{dL_F}{dn}\right) \tag{2.53}$$

$$\mu_{th} = -\int \frac{ds}{dn}\, dT$$

$$= -a\left(1 - \frac{2Q}{3}\right)T^2 + \frac{4}{5\pi^2}a^3T^4\left[(1 - L_F)(1 - 2Q) - n\frac{dL_F}{dn}\right]\,, \tag{2.54}$$

where

$$Q = 1 - \frac{3n}{2m^*}\frac{dm^*}{dn}. \tag{2.55}$$

Other quantities of interest such as the specific heats at constant volume and pressure, and the thermal index are given by standard thermodynamics:

$$C_V = T\left.\frac{dS}{dT}\right|_n = 2aT - \frac{48}{5\pi^2}a^3T^3(1 - L_F) \tag{2.56}$$

$$C_P = T\left.\frac{dS}{dT}\right|_P = 2aT + \frac{T}{n^2}\frac{\left(\left.\frac{\partial P_{th}}{\partial T}\right|_n\right)^2}{\left.\frac{\partial P_{total}}{\partial n}\right|_T} \tag{2.57}$$

$$\Gamma_{th} = 1 + \frac{P_{th}}{nE_{th}} = 1 + \frac{2Q}{3} - \frac{4}{5\pi^2}a^2 nT^2\frac{dL_F}{dn}\,. \tag{2.58}$$

Note that while the NLO terms in the thermal quantities above have the same temperature dependences as those of a free Fermi gas, the accompanying density-dependent factors differ reflecting the effects of interactions.

2.5 Application to Models Beyond Mean Field Theory

In this section, we investigate the degenerate-limit thermodynamics of a relativistic field-theoretical model in which the nucleon-nucleon (NN) interaction is mediated by the exchange of σ, ω, ρ and π mesons (scalar, vector, iso-vector and pseudo-vector, respectively). Nonlinear self-couplings of the scalar field are also included. The model is described by the Lagrangian density [ZP16, Wal74, BB77]

$$\begin{aligned}
\mathcal{L} &= \mathcal{L}_N + \mathcal{L}_{meson} && (2.59)\\
\mathcal{L}_N &= \bar{N}\Big[i\gamma^\mu(\partial_\mu + i\frac{g_\rho}{2}\vec{\rho}_\mu\cdot\vec{\tau} + ig_\omega\omega_\mu \\
&- i\frac{g_A}{2f_\pi}\gamma_5\vec{\tau}\cdot\partial_\mu\vec{\pi}) - (M - g_\sigma\sigma)\Big]N && (2.60)\\
\mathcal{L}_{meson} &= \frac{1}{2}\partial_\mu\sigma\partial^\mu\sigma - \left(\frac{1}{2} + \frac{\kappa_3}{3!}\frac{g_\sigma\sigma}{M} + \frac{\kappa_4}{4!}\frac{g_\sigma^2\sigma^2}{M^2}\right)m_\sigma^2\sigma^2 \\
&- \frac{1}{4}V^{\mu\nu}V_{\mu\nu} + \frac{1}{2}m_\omega^2\omega_\mu\omega^\mu \\
&- \frac{1}{4}B_{\mu\nu}B^{\mu\nu} + \frac{1}{2}m_\rho^2\vec{\rho}_\mu\cdot\vec{\rho}^\mu \\
&+ \frac{1}{2}\partial^\mu\vec{\pi}\cdot\partial_\mu\vec{\pi} - \frac{1}{2}m_\pi^2\vec{\pi}\cdot\vec{\pi}\,, && (2.61)
\end{aligned}$$

where

$$\begin{aligned}
V_{\mu\nu} &= \partial_\mu\omega_\nu - \partial_\nu\omega_\mu && (2.62)\\
B_{\mu\nu} &= \vec{\tau}(\partial_\mu\vec{\rho}_\nu - \partial_\nu\vec{\rho}_\mu) + i\frac{g_\rho}{2}[\vec{\rho}_\mu\cdot\vec{\tau}, \vec{\rho}_\nu\cdot\vec{\tau}] && (2.63)
\end{aligned}$$

are the field-strength tensors and τ are the $SU(2)$ isospin matrices. We use the masses $M = 939$ MeV, $m_\sigma = 550$ MeV, $m_\omega = 783$ MeV, $m_\rho = 770$ MeV and $m_\pi = 138$ MeV, the couplings $g_\sigma = 8.604$, $g_\omega = 7.522$, $g_\rho = 7.614$, $\kappa_3 = 4.84$ and $\kappa_4 = -4.47$, the pion decay constant $f_\pi = 93$ MeV and the nucleon axial current constant $g_A = 1.26$ as in ref. [ZP16].

All thermodynamic quantities of interest can be derived from the grand potential density Ω which is related to the pressure by $\Omega = -P$. For an isotropic system in its rest-frame, the pressure is obtained from the diagonal elements of the spatial part of the energy-momentum tensor $T_{\mu\nu} = \partial\mathcal{L}/\partial(\partial_\mu\phi)\,\partial_\nu\phi - g_{\mu\nu}\mathcal{L}$. In mean-field theory (MFT), the result is

$$\begin{aligned} P &= \frac{1}{3}\langle T_{ii}\rangle \\ &= \frac{\gamma_{spin}}{3}\sum_i \int \frac{d^3p}{(2\pi)^3}\frac{p^2}{E^*(p)} f_i(p) + \frac{g_\omega^2}{2m_\omega^2}n^2 + \frac{g_\rho^2}{8m_\rho^2}(n_i - n_j)^2 \\ &- \frac{m_\sigma^2}{g_\sigma^2}(M - M^*)\left[\frac{1}{2} + \frac{\kappa_3}{6M}(M - M^*) + \frac{\kappa_4}{24M^2}(M - M^*)^2\right], \end{aligned} \tag{2.64}$$

where

$$E^*(p) = (p^2 + M^{*2})^{1/2}\,. \tag{2.65}$$

In the mean-field approximation, the spectrum $\epsilon_i(p)$ that enters the Fermi distribution function $f_i(p) = \{1 + \exp[(\epsilon_i(p) - \mu_i)/T]\}^{-1}$ is given by

$$\epsilon_i(p) = \pm E^*(p) + \frac{g_\omega^2}{m_\omega^2}n + \frac{g_\rho^2}{4m_\rho^2}(n_i - n_j)\,. \tag{2.66}$$

The +(-) sign corresponds to particles (antiparticles) and the subscripts i, j to the two nucleon species. The Dirac effective mass M^* results from the minimization of Ω with respect to the expectation value of the scalar field.

The leading corrections to the mean-field Ω arise from two-loop (TL) exchanges of the mesons involved in the model. These corrections are given by (see, e.g.,

[Chi77, ZP16])

$$\Omega_{ex,\sigma} = -\frac{\gamma_{spin}}{4} g_\sigma^2 \int d\tau_p d\tau_q \; f_s(p,q) D(k; m_\sigma^*) \sum_i f_i(p) f_i(q) \tag{2.67}$$

$$\Omega_{ex,\omega} = -\frac{\gamma_{spin}}{4} g_\omega^2 \int d\tau_p d\tau_q \; f_v(p,q) D(k; m_\omega) \sum_i f_i(p) f_i(q) \tag{2.68}$$

$$\begin{aligned} \Omega_{ex,\rho} &= -\frac{\gamma_{spin}}{16} g_\rho^2 \int d\tau_p d\tau_q \; f_v(p,q) D(k; m_\rho) \\ &\times \sum_i f_i(p)[f_i(q) + 2f_j(q)] \end{aligned} \tag{2.69}$$

$$\begin{aligned} \Omega_{ex,\pi} &= -\frac{\gamma_{spin}}{16} \left(\frac{g_A M^*}{f_\pi}\right)^2 \int d\tau_p d\tau_q \; f_{pv}(p,q) D(k; m_\pi) \\ &\times \sum_i f_i(p)[f_i(q) + 2f_j(q)] \,, \end{aligned} \tag{2.70}$$

where

$$d\tau_p = \frac{d^3p}{(2\pi)^3 2E^*(p)} \,, \quad f_s(p,q) = 4(p^\mu q_\mu + M^{*2}) \,, \tag{2.71}$$

$$f_v(p,q) = 8(p^\mu q_\mu - 2M^{*2}) \,, \quad f_{pv}(p,q) = 16(p^\mu q_\mu - M^{*2}) \,, \tag{2.72}$$

$$D(k;m) = \frac{1}{k^\mu k_\mu - m^2} \; ; \; k^\mu = p^\mu - q^\mu \; , \; p^\mu p_\mu = q^\mu q_\mu = M^{*2}. \tag{2.73}$$

The corresponding TL contributions to the single-particle spectrum [via $\epsilon_{ex}^i = \delta\Omega_{ex}/\delta n_i(p)$ with $\delta/\delta n_i(p) \int d^3p/(2\pi)^3 \, f_i(p) = 1$; i=nucleon species] are [Chi77, ZP16] :

$$\epsilon_{ex,\sigma}^i = -\frac{\gamma_{spin}}{8} \frac{g_\sigma^2}{E^*(p)} \int d\tau_q \; f_s(p,q) D(k; m_\sigma^*) f_i(q) \tag{2.74}$$

$$\epsilon_{ex,\omega}^i = -\frac{\gamma_{spin}}{8} \frac{g_\omega^2}{E^*(p)} \int d\tau_q \; f_v(p,q) D(k; m_\omega) f_i(q) \tag{2.75}$$

$$\epsilon_{ex,\rho}^i = -\frac{\gamma_{spin}}{32} \frac{g_\rho^2}{E^*(p)} \int d\tau_q \; f_v(p,q) D(k; m_\rho)[f_i(q) + 2f_j(q)] \tag{2.76}$$

$$\epsilon_{ex,\pi}^i = -\frac{\gamma_{spin}}{32E^*(p)} \left(\frac{g_A M^*}{f_\pi}\right)^2 \int d\tau_q \; f_{pv}(p,q) D(k; m_\pi)[f_i(q) + 2f_j(q)] \tag{2.77}$$

Note that at the TL level, the self-interactions of the scalar field bestow upon it an effective scalar-meson mass

$$m_\sigma^* = m_\sigma \left[1 + \kappa_3 \left(\frac{M - M^*}{M} \right) + \frac{\kappa_4}{2} \left(\frac{M - M^*}{M} \right)^2 \right]^{1/2} , \tag{2.78}$$

which is used in all exchange terms involving the σ- meson.

2.5.1 Two-loop Calculations of Dense Nucleonic Matter

The degenerate limit formalism delineated in Sec. 2.4 requires for its implementation, in principle, only the $T = 0$ parts of the spectrum [for $\mathcal{M}(p)$] and the pressure (for C_P and M^*). Note, however, that for cold matter the statements $dP/d\sigma = 0$ and $d\mathcal{E}/d\sigma = 0$ are equivalent (being that at $T = 0$, $P = -n\, d\mathcal{E}/dn$) and that the energy density $\mathcal{E}$ is somewhat easier to minimize with respect to σ in order to obtain M^*. We therefore opt to work with the latter. Confining ourselves to symmetric nuclear matter (SNM) and pure neutron matter (PNM) in the interest of simplicity, we have for the energy density (in the notation of ref. [Chi77])

$$\mathcal{E}_{TL} = \mathcal{E}_{MFT} + \mathcal{E}_{ex,\sigma} + \mathcal{E}_{ex,\omega} + \mathcal{E}_{ex,\rho} + \mathcal{E}_{ex,\pi} \tag{2.79}$$

$$\begin{aligned} \mathcal{E}_{MFT} &= 2\gamma_{iso} \int_0^{p_F} \frac{d^3p}{(2\pi)^3} E^* + \frac{1}{2} \frac{g_\omega^2}{m_\omega^2} n^2 + \frac{(1 - \gamma_{charge})}{8} \frac{g_\rho^2}{m_\rho^2} n^2 \\ &+ \frac{m_\sigma^2}{g_\sigma^2} (M - M^*)^2 \left[\frac{1}{2} + \frac{\kappa_3}{3!} \left(\frac{M - M^*}{M} \right) + \frac{\kappa_4}{4!} \left(\frac{M - M^*}{M} \right)^2 \right] \end{aligned} \tag{2.80}$$

$$\mathcal{E}_{ex,\sigma} = \gamma_{iso} \frac{g_\sigma^2}{(2\pi)^4} M^{*4} \left[\frac{1}{4} (x\eta - \ln \xi)^2 + \left(1 - \frac{w_\sigma^*}{4} \right) I(w_\sigma^*) \right] \tag{2.81}$$

$$\mathcal{E}_{ex,\omega} = \gamma_{iso} \frac{g_\omega^2}{(2\pi)^4} M^{*4} \left[\frac{1}{2} (x\eta - \ln \xi)^2 - \left(1 + \frac{w_\omega}{2} \right) I(w_\omega) \right] \tag{2.82}$$

$$\mathcal{E}_{ex,\rho} = \frac{(\gamma_{iso} + 4\gamma_{charge})}{4} \frac{g_\rho^2}{(2\pi)^4} M^{*4} \left[\frac{1}{2} (x\eta - \ln \xi)^2 - \left(1 + \frac{w_\rho}{2} \right) I(w_\rho) \right] \tag{2.83}$$

$$\mathcal{E}_{ex,\pi} = \frac{(\gamma_{iso} + 4\gamma_{charge})}{4} \left(\frac{g_A M^*}{f_\pi} \right)^2 \frac{M^{*4}}{(2\pi)^4} \left[(x\eta - \ln \xi)^2 - w_\pi I(w_\pi) \right] \tag{2.84}$$

and for the spectrum [via $\epsilon_{ex,i} = \delta\mathcal{E}_{ex,i}/\delta n$; i=meson]

$$\epsilon_{TL} = \epsilon_{MFT} + \epsilon_{ex,\sigma} + \epsilon_{ex,\omega} + \epsilon_{ex,\rho} + \epsilon_{ex,\pi} \tag{2.85}$$

$$\epsilon_{MFT} = M^* e + \frac{g_\omega^2}{m_\omega^2} n + \frac{(1-\gamma_{charge})}{4}\frac{g_\rho^2}{m_\rho^2} n \tag{2.86}$$

$$\epsilon_{ex,\sigma} = \frac{g_\sigma^2}{(2\pi)^2}\frac{M^*}{2e}\left[\frac{1}{2}(x\eta - \ln\xi) + \left(1 - \frac{w_\sigma^*}{4}\right)\frac{2}{r}J(w_\sigma^*)\right] \tag{2.87}$$

$$\epsilon_{ex,\omega} = \frac{g_\omega^2}{(2\pi)^2}\frac{M^*}{2e}\left[(x\eta - \ln\xi) - \left(1 + \frac{w_\omega}{2}\right)\frac{2}{r}J(w_\omega)\right] \tag{2.88}$$

$$\epsilon_{ex,\rho} = \frac{(\gamma_{iso}+\gamma_{charge})}{4}\frac{g_\rho^2}{(2\pi)^2}\frac{M^*}{2e}\left[(x\eta - \ln\xi) - \left(1 + \frac{w_\rho}{2}\right)\frac{2}{r}J(w_\rho)\right] \tag{2.89}$$

$$\epsilon_{ex,\pi} = \frac{(\gamma_{iso}+\gamma_{charge})}{4}\left(\frac{g_A M^*}{f_\pi}\right)^2\frac{M^*}{2e(2\pi)^2}\left[2(x\eta - \ln\xi) - w_\pi\frac{2}{r}J(w_\pi)\right], \tag{2.90}$$

where

$$\gamma_{iso} = \begin{cases} 1 & \text{PNM} \\ 2 & \text{SNM} \end{cases}, \quad \gamma_{charge} = \begin{cases} 0 & \text{PNM} \\ 1 & \text{SNM} \end{cases} \tag{2.91}$$

$$x = \frac{p_F}{M^*}\ ,\ \eta = (1+x^2)^{1/2}\ ,\ \xi = x + \eta \tag{2.92}$$

$$r = \frac{p}{M^*}\ ,\ e = (1+r^2)^{1/2}\ ,\ t = r + e \tag{2.93}$$

$$w_i = \frac{m_i^2}{M^{*2}}\ ;\ i = \sigma^*, \omega, \rho, \pi \tag{2.94}$$

$$I(w_i) = \int_1^\xi\int_1^\xi dz\, dy\left(1 - \frac{1}{z^2}\right)\left(1 - \frac{1}{y^2}\right)\ln\left[\frac{(zy-1)^2 + w_i zy}{(z-y)^2 + w_i zy}\right] \tag{2.95}$$

$$J(w_i) = \int_1^\xi dz\left(1 - \frac{1}{z^2}\right)\ln\left[\frac{(zt-1)^2 + w_i zy}{(z-t)^2 + w_i zy}\right]. \tag{2.96}$$

With the inclusion of the TL contributions and noting that $M^* = M - g_\sigma\sigma$, the Dirac effective mass M^* is determined by solving

$$\begin{aligned}
\partial\mathcal{E}_{TL}/\partial M^* &= 0 \quad \text{with} && (2.97)\\
\frac{\partial\mathcal{E}_{MFT}}{\partial M^*} &= 2\gamma_{iso}\int_0^{p_F}\frac{d^3p}{(2\pi)^3}\frac{M^*}{E^*} - \frac{m_\sigma^2}{g_\sigma^2}(M-M^*) \\
&\times \left[1 + \frac{\kappa_3}{2}\left(\frac{M-M^*}{M}\right) + \frac{\kappa_4}{6}\left(\frac{M-M^*}{M}\right)^2\right] && (2.98)\\
\frac{\partial\mathcal{E}_{ex,\sigma}}{\partial M^*} &= \frac{4\mathcal{E}_{ex,\sigma}}{M^*} + \gamma_{iso}\frac{g_\sigma^2}{(2\pi)^4}M^{*4} \\
&\times \left[-\frac{x^3}{M^*\eta}(x\eta - \ln\xi) + \left(1 - \frac{w_\sigma^*}{4}\right)\frac{\partial I_{\sigma^*}}{\partial M^*} + \frac{w_\sigma^*}{2M^*}I_{\sigma^*}\right] && (2.99)\\
\frac{\partial\mathcal{E}_{ex,\omega}}{\partial M^*} &= \frac{4\mathcal{E}_{ex,\omega}}{M^*} + \gamma_{iso}\frac{g_\omega^2}{(2\pi)^4}M^{*4} \\
&\times \left[-\frac{2x^3}{M^*\eta}(x\eta - \ln\xi) - \left(1 + \frac{w_\omega}{2}\right)\frac{\partial I_\omega}{\partial M^*} + \frac{w_\omega}{M^*}I_\omega\right] && (2.100)\\
\frac{\partial\mathcal{E}_{ex,\rho}}{\partial M^*} &= \frac{4\mathcal{E}_{ex,\rho}}{M^*} + \frac{(\gamma_{iso}+4\gamma_{charge})}{4}\frac{g_\rho^2}{(2\pi)^4}M^{*4} \\
&\times \left[-\frac{2x^3}{M^*\eta}(x\eta - \ln\xi) - \left(1 + \frac{w_\rho}{2}\right)\frac{\partial I_\rho}{\partial M^*} + \frac{w_\rho}{M^*}I_\rho\right] && (2.101)\\
\frac{\partial\mathcal{E}_{ex,\pi}}{\partial M^*} &= \frac{6\mathcal{E}_{ex,\pi}}{M^*} + \frac{(\gamma_{iso}+4\gamma_{charge})}{4}\left(\frac{g_A M^*}{f_\pi}\right)^2\frac{M^{*4}}{(2\pi)^4} \\
&\times \left[-\frac{4x^3}{M^*\eta}(x\eta - \ln\xi) - w_\pi\frac{\partial I_\pi}{\partial M^*} + \frac{2w_\pi}{M^*}I_\pi\right], && (2.102)
\end{aligned}$$

where

$$\begin{aligned}
\frac{\partial I(w_{\sigma^*})}{\partial M^*} &= \frac{1}{2M^*}\left\{ w_{\sigma^*}\left(1-\frac{M^*}{m^*_\sigma}\frac{dm^*_\sigma}{dM^*}\right)\right. \\
&\times \int_1^\xi\int_1^\xi dy\,dz \frac{1}{yz}\frac{(1-z^2)^2(1-y^2)^2}{[(zy-1)^2+w_{\sigma^*}zy][(z-y)^2+w_{\sigma^*}zy]} \\
&- \left.\frac{x\xi}{\eta}\left(1-\frac{1}{\xi^2}\right)J(w_{\sigma^*};t\to\xi)\right\} \qquad (2.103)\\
\frac{dm^*_\sigma}{dM^*} &= -\frac{m^2_\sigma}{2Mm^*_\sigma}\left[\kappa_3+\kappa_4\left(\frac{M-M^*}{M}\right)\right] \qquad (2.104)\\
\frac{\partial I(w_i)}{\partial M^*} &= \frac{1}{2M^*}\left\{ w_i\int_1^\xi\int_1^\xi dy\,dz \frac{1}{yz}\frac{(1-z^2)^2(1-y^2)^2}{[(zy-1)^2+w_izy][(z-y)^2+w_izy]}\right. \\
&- \left.\frac{x\xi}{\eta}\left(1-\frac{1}{\xi^2}\right)J(w_i;t\to\xi)\right\} \;\;;\;\; i=\omega,\rho,\pi. \qquad (2.105)
\end{aligned}$$

To obtain eqs. (2.103) and (2.105), the 2-dimensional Leibniz rule

$$\begin{aligned}
\frac{d}{dt}\int_{x_0(t)}^{x_1(t)}\int_{y_0(t)}^{y_1(t)} F(x,y,t)dx\,dy &= \int_{y_0}^{y_1}\left[F(x_1)\frac{\partial x_1}{\partial t}-F(x_0)\frac{\partial x_0}{\partial t}\right]dy \\
&+ \int_{x_0}^{x_1}\left[F(y_1)\frac{\partial y_1}{\partial t}-F(y_0)\frac{\partial y_0}{\partial t}\right]dx \\
&+ \int_{x_0}^{x_1}\int_{y_0}^{y_1}\frac{\partial F}{\partial t}dx\,dy \qquad (2.106)
\end{aligned}$$

was employed.

Numerical notes

The various integrals above are readily calculated by using the Gauss-Legendre quadrature method [AS72]. The results reported below were calculated using 32 points and weights in each dimension although use of 16 points and weights was found to be adequate. The derivatives of $\mathcal{M}(p)$ and $L_F(n)$ were calculated using the 5-point rule [AS72]. Root finding was accomplished by the Newton-Raphson scheme. All numerical results of our Fortran code were also verified by using Mathematica.

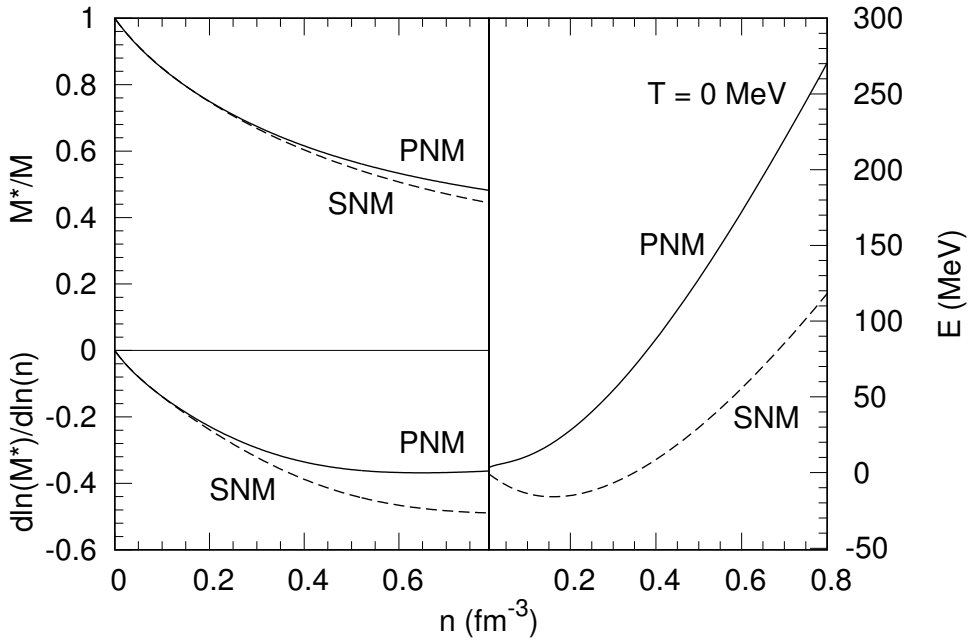

Figure 2.1: Upper left panel: Dirac effective masses M^* [eq. (2.97)] scaled with the vacuum nucleon mass vs density n in symmetric nuclear matter (SNM) and pure neutron matter (PNM) at temperature $T = 0$. Lower left panel: Logarithmic derivatives of M^* w.r.t n. Right panel: Energy per particle $E = \partial\mathcal{E}/\partial n - M$ vs n in SNM and PNM at $T = 0$.

2.5.2 Results and Discussion

The variational procedure $\partial\mathcal{E}_{TL}/\partial M^* = 0$ in eq. (2.97) minimizes the energy density of the system and results in the optimal baryon (Dirac) effective mass M^* at each n. (This minimization condition also yields the expectation value of the scalar field $\sigma = (M - M^*)/g_\sigma$.) The values of M^* in SNM and PNM are shown in the upper left panel of fig. 2.1. Use of these M^*'s in the expressions for the energy density in eq. (2.79) allows for a calculation of the energy per particle, and are shown in the right panel of fig. 2.1 for SNM and PNM at $T = 0$. These results yield good agreement with nuclear and neutron star phenomenology [ZP16]. The TL contributions to the energy density play a significant role in determining $M^*(n)$. The pattern $M^*(\text{PNM}) \geq M^*(\text{SNM})$ for a given baryon density stems from the isospin-invariant nucleon-nucleon interactions employed in the model. An

MFT calculation - that is, without the TL terms in eq. (2.79) - that yields closely resembling E vs. n curves shown here through a readjustment of the various coupling strengths produces M^* curves that vary more steeply with density (not shown here, but see ref. [ZP16]). As $M^*(n)$ and its logarithmic derivative w.r.t. n (lower left panel of fig. 2.1) enter prominently in determining the thermal properties, contrasts between different levels of theoretical approximations (MFT vs MFT+TL in our case here) are afforded.

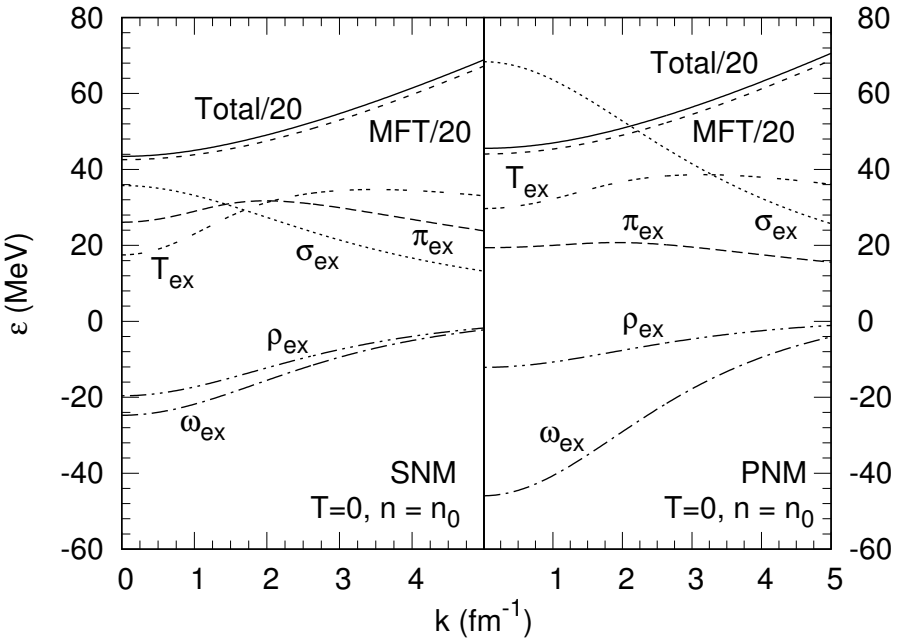

Figure 2.2: Contributions from MFT and TL terms [from eq. (2.85)] involving the exchange of σ, ω, ρ, and π mesons to the total single-particle energy vs. wave number in SNM and PNM at the baryon density $n = n_0 = 0.16$ fm^{-3}.

Under degenerate conditions for which $T/T_F \ll 1$, thermal effects depend sensitively on details of the single-particle spectrum near the Fermi surface. The various contributions to the $T = 0$ single-particle spectra in SNM and PNM are shown in fig. 2.2 at $n = n_0 = 0.16$ fm^{-3}. Note that the dominant contribution from the MFT part in eq. (2.85) has been divided by a factor of 20 to fit within the figure where contributions from the exchange of σ, ω, ρ, and π mesons from eq. (2.85) are also shown. Although

subdominant in their contributions to the spectra, the exchange contributions significantly alter the $M^*(n)$ curves from those of MFT and hence the MFT term of $\epsilon(p)$.

Depending on the density, the magnitude and slope of the single-particle spectrum are also altered from its MFT contribution as can be seen in fig. 2.3 where results for $n = 3n_0$ are shown. Such differences will be reflected in the thermal properties, particularly in the NLO terms of FLT.

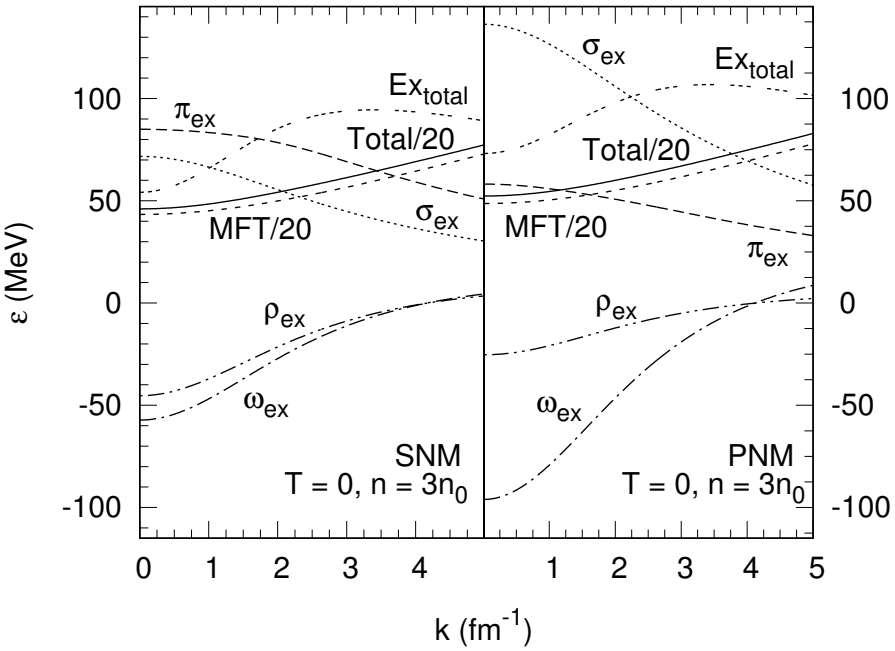

Figure 2.3: Same as fig. 2.2, but for $n = 3n_0$.

The Landau effective masses $m^*(n)$ from eq. (2.46) scaled with the vacuum nucleon mass are shown in the left panel of fig. 2.4 as functions of density in SNM and PNM. The associated logarithmic derivatives are in the right panel of this figure. The TL results are substantially larger than those of MFT for the same n (see ref. [ZP16]). The non-monotonic behaviors and the minima in the $m^*(n)$ curves are characteristic of relativistic field theoretical models in which $M^*(n)$ continually decreases with increasing n. Together with the derivatives of the Landau effective mass function required at NLO in

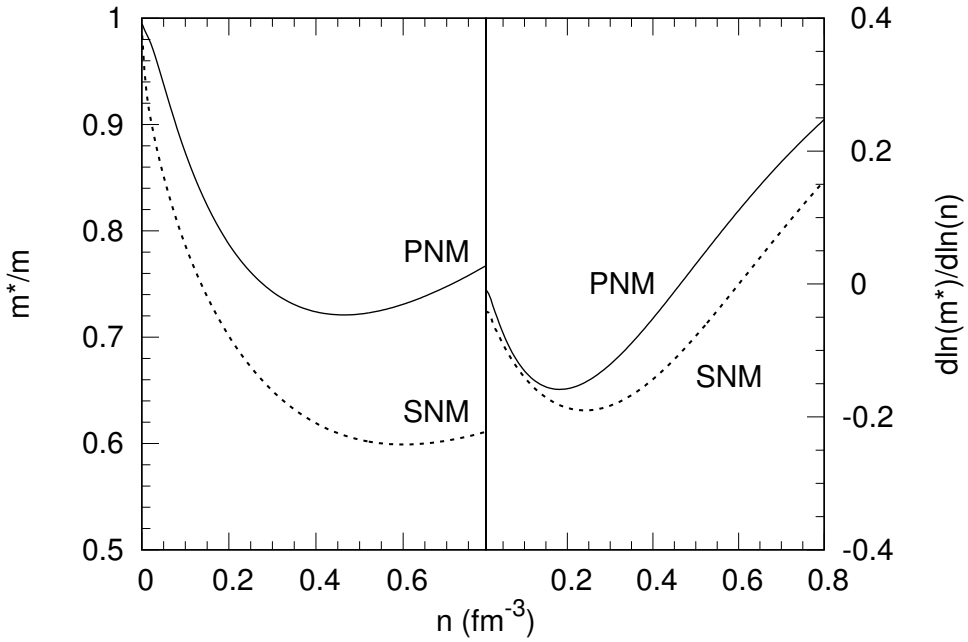

Figure 2.4: Left panel: Landau effective masses from eq. (2.46) scaled with the vacuum nucleon mass vs density in SNM and PNM. Right panel: Logarithmic derivatives of the Landau effective masses w.r.t. density.

FLT, $m^*(n)$ and its logarithmic derivative play important roles in improving the accuracy of the degenerate limit thermodynamics.

We turn now to compare the thermal properties from FLT and FLT+NLO with those from the exact numerical results of ref. [ZP16] for the TL calculations at temperatures of $T = 20$ and 50 MeV, respectively. In all cases, comparisons shown for $T = 50$ MeV highlight the onset of semi- or non-degenerate regions in density for which results of degenerate limit FLT and FLT+NLO begin to become inadequate.

In astrophysical phenomena involving supernovae, neutron stars and binary mergers, the entropy per baryon S serves as a gauge to track hydrodynamical evolution and its consequences [BBAL79]. Figure 2.5 shows S vs n in SNM and PNM at $T = 20$ and 50 MeV, respectively. For both SNM and PNM, the NLO corrections substantially improve agreement with the exact results for S up to 2. For $T = 20$ MeV, the agreement extends to

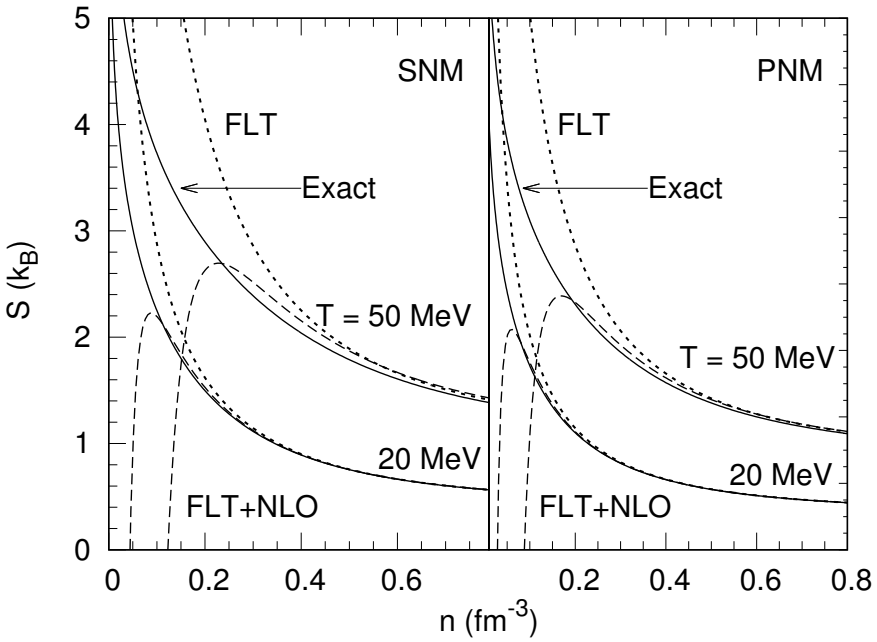

Figure 2.5: Entropies per particle $S = s/n$ vs. baryon number density in SNM and PNM. Results labeled "Exact" are from ref. [ZP16]. The leading order Fermi Liquid Theory results are labeled "FLT" whereas "FLT+NLO" stands for results of next-to-leading-order FLT with s from eq. (2.50). Values of temperatures are as indicated in the figure.

the subnuclear nuclear density of $n = 0.1$ fm^{-3} for both SNM and PNM. This agreement is encouraging as for $n \lesssim 0.1$ fm^{-3} and $T \lesssim 20$ MeV, matter exists in an inhomogeneous phase consisting of heavy nuclei, light nuclear clusters such as α particles, tritons and deuterons, and dripped nucleons (as also leptons and photons) for which a separate treatment is required. The lesson learned is that up to $S = 2$, the thermal properties of bulk homogeneous nucleonic matter is adequately described by a knowledge of the $T = 0$ spectra of nucleons from which all thermal properties can be obtained through the use of FLT carried up to NLO terms.

In fig. 2.6, we show results for the thermal energies. As for S, the NLO corrections extend agreement with the exact results down to $n \simeq 0.1$ fm^{-3} in both SNM and PNM. The agreement for PNM extends to somewhat lower densities because PNM is more

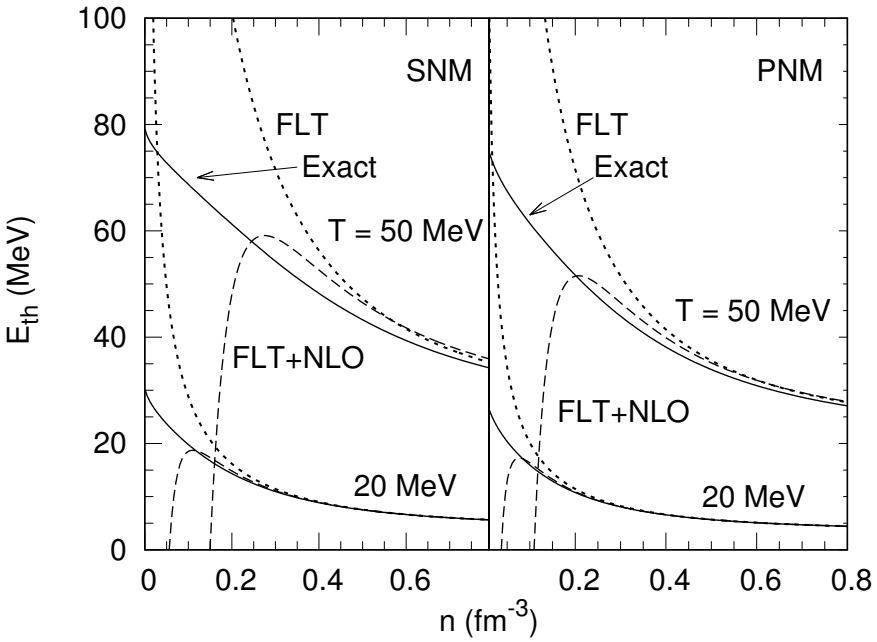

Figure 2.6: Same as fig. 2.5 but for thermal energies from eq. (2.52).

degenerate than SNM at the same n. The results at $T = 50$ MeV indicate the densities for which matter is in the semi- or non-degenerate regions. The substantial improvement offered by the NLO corrections are, however, noteworthy.

Figure 2.7 contains results for the thermal pressures. As for S and E_{th}, agreement of the FLT+NLO results with those of exact numerical calculations extend up to $n \simeq 0.1$ fm^{-3} at $T = 20$ MeV. The situation with the results at $T = 50$ MeV is less satisfactory. The disagreement with the exact results at this temperature is partly owing to the fact that M^* begins to acquire a non-negligible temperature dependence as T increases [PABW87], not considered in the FLT+NLO treatment. Also at work is the fact that the thermodynamic identity $\mathcal{E} + P = Ts + \mu n$ cannot be satisfied even in principle beyond the Hartree level unless the theory is exactly solved.

The thermal parts of the chemical potentials are shown in fig. 2.8. As for S, E_{th}, and P_{th}, the NLO corrections render significant improvement over the FLT results down to

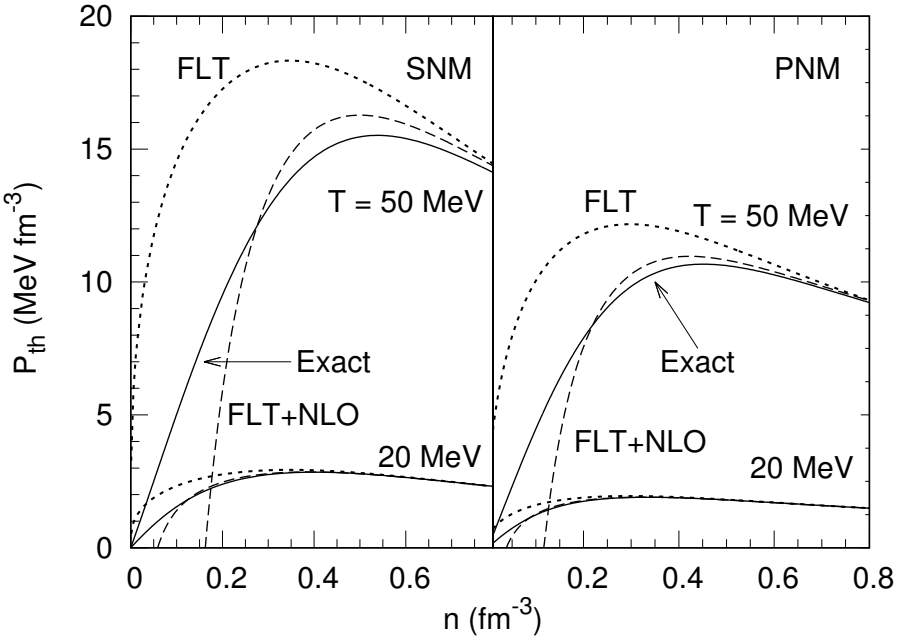

Figure 2.7: Same as fig. 2.5, but for thermal pressure from eq. (2.53).

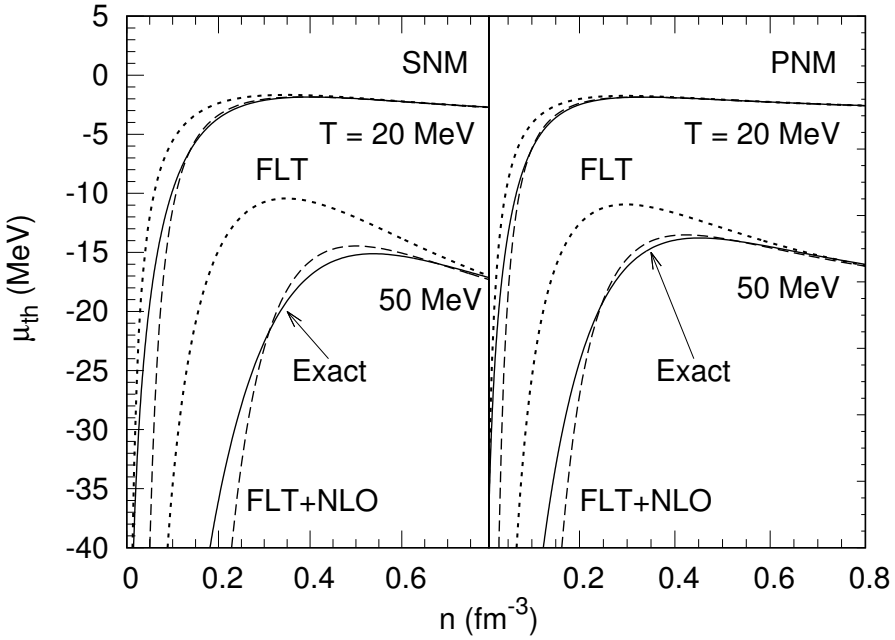

Figure 2.8: Same as fig. 2.5, but for thermal chemical potential from eq. (2.54).

$n \simeq 0.1$ fm^{-3} for $T = 20$ MeV. The agreement of the FLT+NLO results with the exact results is quantitatively better for PNM than for SNM because of its higher degeneracy at this temperature at the same density. The NLO improvements at $T = 50$ MeV are less striking than at 20 MeV, and suffer from the same maladies as the other thermal variables. Analytic expressions for Fermi integrals being asymptotic expansions, this disagreement is unavoidable particularly in the semi-degenerate region. A separate treatment as espoused in ref. [PABW87] is necessary in the non-degenerate region.

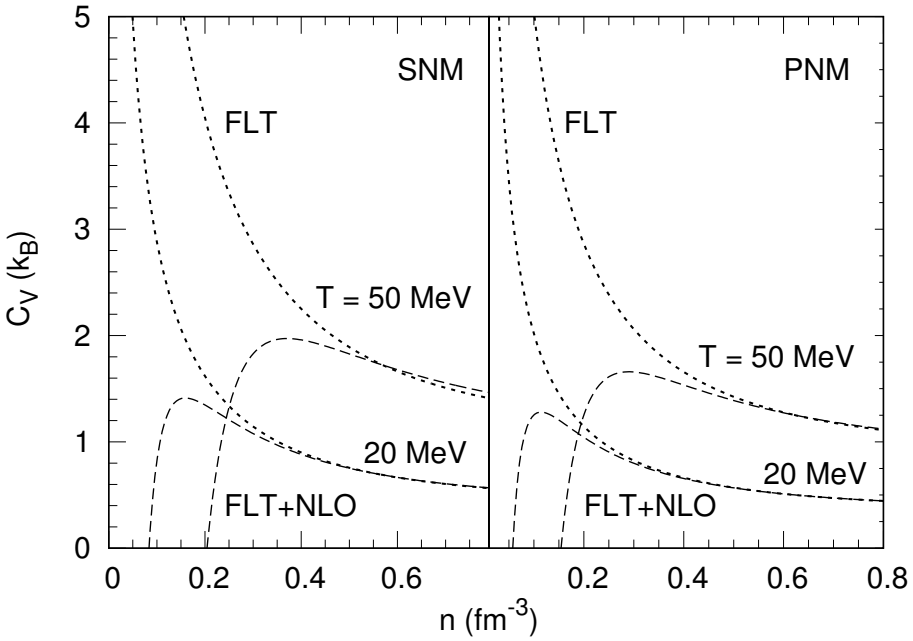

Figure 2.9: Same as fig. 2.5, but for specific heat at constant volume from eq. (2.56).

The specific heat at constant volume C_V is shown in fig. 2.9. Exact results for C_V were not calculated in ref. [ZP16], but we can easily gauge the improvement from NLO corrections at near nuclear densities by recalling that at leading order in FLT, $C_V = S$. The quantity C_V plays a major role in the long-term cooling of a neutron star. For example, the time for a star's center to cool by neutrino emission can be estimated by

$$\Delta t = -\int \frac{nC_V}{\epsilon_\nu}\, dT\,, \tag{2.107}$$

where ϵ_ν is the neutrino emissivity and T is the temperature. At low temperatures ($T \leq 1$ MeV), however, corrections to C_V arising from Cooper-pairing of nucleons must be considered.

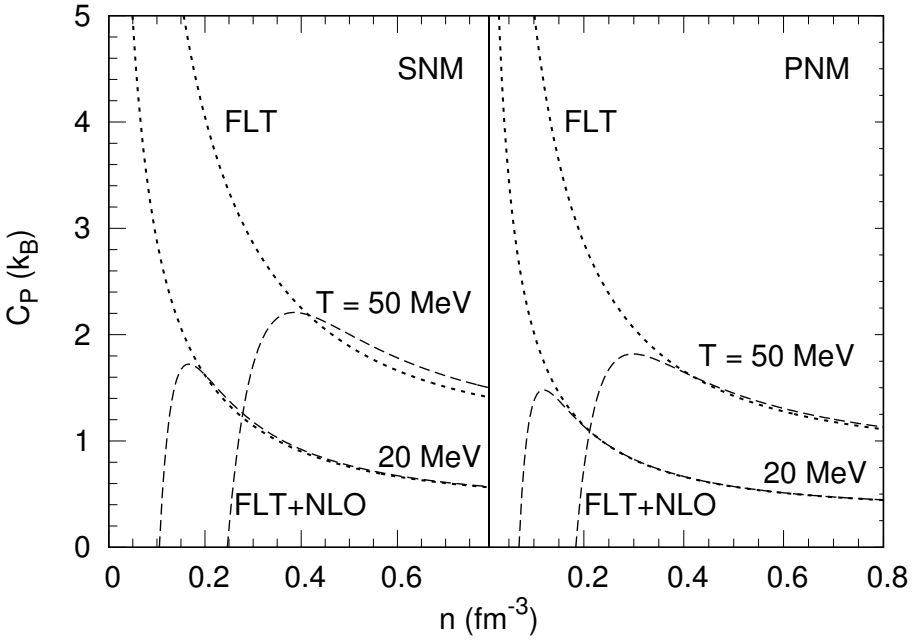

Figure 2.10: Same as fig. 2.5, but for specific heat at constant pressure from eq. (2.57).

Figure 2.10 shows results for the specific heat at constant pressure. As for C_V, exact numerical results for C_P are not yet available, hence only the FLT and FLT+NLO results are shown. At leading order in FLT, $C_P = S$. It is intriguing that at $T = 20$ MeV, the NLO corrections do not alter the leading order FLT result down to near nuclear densities in both SNM and PNM. While the situation is similar for $T = 50$ MeV in PNM for $n \gtrsim 0.35$ fm^{-3}, NLO corrections are apparent in SNM. Exact calculations at $T = 50$ MeV would be necessary to confirm the extent to which NLO corrections improve the FLT results. A relation similar to eq. (2.107) but with C_V replaced by C_P and ϵ_ν replaced by $\epsilon_{\gamma+\nu}$ is often used in the literature for time estimates in astrophysical phenomena.

Results for Γ_{th} are shown in Figure 2.11. At leading order in FLT, $\Gamma_{th} = \frac{5}{3} - \frac{n}{m^*}\frac{dm^*}{dn}$ and is independent of T. This feature is borne out by the results (short dashed curves) in both SNM and PNM, the differences between them stemming from differences in the logarithmic derivatives of the Landau effective masses (see fig. 2.4). At NLO, Γ_{th} acquires a temperature dependence owing to terms proportional to T^4 in both P_{th} and ϵ_{th}. With increasing n, and hence degeneracy, the coefficient of the leading $O(T^2)$ term in Γ_{th} decreases making the NLO corrections to diminish in magnitude. The agreement of the FLT+NLO results with the exact results extends to sub-nuclear densities at $T = 20$ MeV in both SNM and PNM. The $T = 50$ MeV results delineate the regions of density for which a semi-degenerate analysis is warranted. At very low densities, the exact $\Gamma_{th} \rightarrow \frac{5}{3}$ the value for non-relativistic ideal gases.

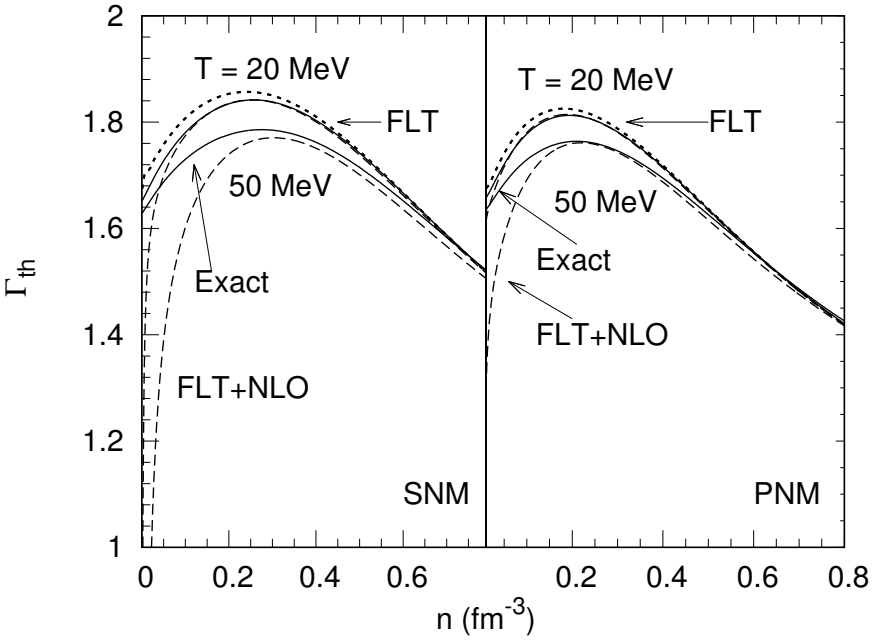

Figure 2.11: Same as fig. 2.5, but for the thermal adiabatic index from eq. (2.58).

From the results shown above in figs. 2.5 through 2.11, it is clear that the lowest density beyond which the FLT+NLO results reproduce the exact numerical results as a function of increasing temperature steadily increases owing to the semi-degenerate region being encountered. The case of $T = 30$ MeV is especially interesting as it happens to be the maximum temperature encountered in core-collapse supernova simulations. Lacking exact numerical results for MFT+TL calculations at $T = 30$ MeV, we performed exact numerical calculations for MFT using the couplings in ref. [ZP16] and compared the ensuing results with those of FLT+NLO (not shown here). For all thermal variables, our findings are: (1) for SNM, very good agreement is found for $n \gtrsim 0.2$ fm^{-3}, and (2) for PNM, the agreement is very good starting from the nuclear density of $n_0 \gtrsim 0.16$ fm^{-3}. We expect a similar behavior for MFT+TL because the total single-particle spectra for both SNM and PNM are predominantly composed of their corresponding MFT parts. For values of Y_e intermediate to those of SNM and PNM, caution must be exercised in carrying the conclusions above as one or the other nucleonic species may be in the non- or semi-degenerate region.

2.6 Summary and Conclusions

In this chapter, the next-to-leading order (NLO) extension of Landau's Fermi Liquid Theory (FLT) developed in ref. [CMPL15a] was utilized to calculate the thermal properties of symmetric nuclear and pure neutron matter (SNM and PNM) for the relativistic model of ref. [ZP16] in which two-loop (TL) corrections to mean field theory (MFT) were included. In FLT, the Landau effective mass m^* and its logarithmic derivative with respect to density n suffice to capture the leading order temperature (T) effects. The NLO corrections, which account for the next-higher-order effects in T, require up to second order derivatives of the generalized Landau effective mass function $\mathcal{M}(p) = p\left(\dfrac{\partial\epsilon}{\partial p}\right)^{-1}$, where $\epsilon \equiv \epsilon(n, p)$ is the density and momentum dependent part of the

$T = 0$ single-particle spectrum. The explicit form of $\epsilon(n, p)$ depends on the specific nature of the $T = 0$ many-body calculation performed. Contrasting examples include models with contact or finite range interactions, MFT vs MFT+TL approximations, Bruekner-Hartree-Fock vs Dirac-Brueckner-Hartree-Fock, effective field-theoretical approaches at various levels of approximation, etc. For all these cases, the NLO extension enables the calculation of the entropy density and specific heats up to $O(T/T_F)^3$ whereas the energy density, chemical potential and pressure to $O(T/T_F)^4$ (where T_F is the Fermi temperature) extending the leading order results of FLT.

Our comparisons of FLT and FLT+NLO results with those of the exact numerical calculations reported in ref. [ZP16] for the relativistic model in which TL effects were included reveal that substantial improvements are achieved by the NLO corrections for all thermal variables (entropy, energy, pressure, chemical potential, and specific heats) for entropy per baryon S of up to 2. It is noteworthy that the NLO corrections extend agreement with the exact results to sub-nuclear densities of $n \sim 0.1$ fm^{-3} for $T = 20$ MeV, whereas the FLT results are valid for densities beyond ~ 0.1 fm^{-3}. Insofar as for $T \lesssim 20$ MeV and $n \lesssim 0.1$ fm^{-3}, an inhomogeneous phase consisting of heavy nuclei, light nuclear clusters, dripped nucleons, and pasta-like configurations exists which requires a separate treatment, the semi-analytical formulas of the FLT+NLO formalism enables a rapid evaluation of thermal effects in bulk homogeneous matter in addition to providing physical insights and checks of time-consuming exact numerical calculations.

Several areas for further investigation remain including an assessment of non-analytic contributions arising from long-wavelength fluctuations, single particle-hole excitations and, collective and pairing correlations close to the Fermi surface [BP91]. Establishing their roles in astrophysical phenomena needs further work.

2.7 Specific Contributions of the Author

The work documented in this chapter is largely derived from the published paper, "Thermal effects in dense matter beyond mean field theory" which has been the effort of a team including myself (Sudhanva Lalit), and Drs. Constantinos Constantinou and Madappa Prakash. The project of constructing "Thermal Effects in Dense Matter Beyond Mean Field Theory" using state-of-the-art Lagrangian densities was conceived by my advisor Madappa Prakash. The completion of this project involved significant new developments in both theoretical formalisms and numerical techniques. I am the second author in the peer-reviewed journal publication of the work presented in this chapter. All analytic equations used in this chapter were independently derived by me and crosschecked with those derived by other members of the team. The FORTRAN codes written to produce the results presented in this chapter were written by me jointly with my advisor Madappa Prakash. All figures presented in this chapter were conceptualized by the team but produced by me alone. The writing of this chapter was a team effort with the work being divided such that each member wrote the first draft of a given section, then passed it to another member to be augmented and improved. The process of passing the work between the team members was iterated until all members agreed on the final version. For the first drafts, my focus was on the sections containing results and their discussion, but I was actively involved in developing each section during the iteration process.

3 Dense Matter Equation of State for Neutron Star Mergers

3.1 Motivation

The observed decay of the mutual orbits with time in the binary pulsar system B1913+16 [TC99] and its excellent agreement with predictions of post-Newtonian gravity gave the first indirect evidence of the radiation of gravitational waves. Measurements of the various orbital parameters in this system also resulted in a precise determination of the companions masses, that of the neutron star being $1.4408 \pm 0.0003 M_\odot$. Since then, several precise measurements of neutron stars have been made in binary systems containing a radio pulsar [Lat12]. Recent examples of the most massive neutron stars are from the radio pulsars PSR J1614+2230 [$M = (1.97 \pm 0.04) M_\odot$] [DPR$^+$10], PSR J0348+0432 [$M = (2.01 \pm 0.04) M_\odot$][AFW$^+$13], and MSP J0740+6620 $\left[M = (2.17^{+0.11}_{-0.10}) M_\odot\right]$[C$^+$19].

Einstein's theory of General Relativity predicts the emission of gravity waves from asymmetric spinning compact objects, from mergers involving neutron stars and black holes, and from gravitational-collapse supernovae [Tho97]. For mergers of compact objects in binary systems, the gravitational-wave signature is primarily determined by the so-called chirp mass $\mathcal{M} = (M_1 M_2)^{3/5} (M_1 + M_2)^{-1/5}$. The radiation of gravitational waves causes loss of orbital angular momentum and removes energy which results in the mutual orbits to decay. For the binary pulsar systems B1913+16 and PSR J0737-3039, the merger timescales are about 250 and 85 million years. As many compact binaries exist in our and nearby Galaxies, copious amounts of gravitational radiation is expected.

The first direct evidence for the existence of gravitational waves was obtained through its detections by LIGO (Laser Interferometer Gravitational-Wave Observatory) in the binary black hole system GW150914 about 1.3 billion light years away on Sep 14, 2015 [A$^+$16]. Analysis of the data yielded a chirp mass of $\mathcal{M} = 30\, M_\odot$ with individual

black hole masses in the range $M_1 = 36^{+5}_{-4}\, M_\odot$ and $M_2 = 29^{+4}_{-4} M_\odot$. The first observation of gravitational waves from the merger of binary neutron stars, now known as GW170817 took place on Aug 18, 2017, by the advanced LIGO and VIRGO collaborations [A$^+$17c]. In this case, $\mathcal{M} = 1.188^{+0.004}_{-0.002}$, and $M_1 = (1.36 - 1.60) M_\odot$ and $M_2 = (1.17 - 1.36)\, M_\odot$. In addition to the masses, binary neutron star mergers allow for tidal deformations of the stars to be inferred in the stage prior to coalescence. Observation of GW170817 has placed bounds on the tidal deformability of stars in the mass range $1.2 - 1.6\ M_\odot$ to be $\tilde{\Lambda} = 222^{+420}_{-138}$. Although the reported error bars in $\bar{\Lambda}$ are large, the individual radii are estimated to be < 13.5 km [DFL$^+$18]. Combining the electromagnetic [C$^+$17, LMCP19] and gravitational wave information, it has also become possible to place constraint on the maximum gravitational mass of a neutron star: $M^g_{max} \lesssim 2.17 M_\odot$ [MM17, RMW18]. It is interesting that the accurately measured masses of the very massive neutron stars are very close to this limit. Pinning down the maximum mass of a neutron star has implications for the number of stellar mass black holes in our Universe.

Quite recently, observations of additional mergers have been reported; see reports in [X$^+$19] on April 2, 2019 and [LIG] on April 25, 2019. It is thought that one of these merger events (undetected in LIGO but observed through its X-ray signal in the Chandra deep field survey (CDF-S)) produced a magnetar (CDF-S X-ray transient XT2) at a distance of 6.6 billion light years[X$^+$19]. As of today when this thesis is being written, the second event is still under analysis.

In addition to gravitational waves, the detection of electromagnetic radiation (in the gamma ray, X-ray, optical and infra-red bands) in neutron star as well as neutron star - black hole merger events have the potential to shed led light not only on neutron star structure, but also on *r*-process nucleosynthesis of elements [LS76] and the origin of the shorter-duration gamma ray bursters [ELPS89].

The content of this chapter is largely drawn from the peer-reviewed, published paper "Dense matter equation of state for neutron star mergers" [LMCP19], which will be reproduced verbatim here. My specific contributions to this work are detailed at the end of this chapter.

Dense matter equation of state for neutron star mergers[2]

S. Lalit, M. A. A. Mamun, C. Constantinou, and M. Prakash[3]

Department of Physics and Astronomy,

Ohio University, Athens, Ohio 45701, United States

Abstract: In simulations of binary neutron star mergers, the dense matter equation of state (EOS) is required over wide ranges of density and temperature as well as under conditions in which neutrinos are trapped, and the effects of magnetic fields and rotation prevail. Here we assess the status of dense matter theory and point out the successes and limitations of approaches currently in use. A comparative study of the excluded volume (EV) and virial approaches for the $npα$ system using the equation of state of Akmal, Pandharipande and Ravenhall for interacting nucleons is presented in the sub-nuclear density regime. Owing to the excluded volume of the α-particles, their mass fraction vanishes in the EV approach below the baryon density 0.1 fm^{-3}, whereas it continues to rise due to the predominantly attractive interactions in the virial approach. The EV approach of Lattimer et al. is

[2] Contribution to the Topical Issue "First joint gravitational wave and electromagnetic observations: Implications for nu- clear and particle physics" edited by David Blaschke, Monica Colpi, Charles J. Horowitz, David Radice.

[3] email: prakash@ohio.edu

extended here to include clusters of light nuclei such as d, ^{3}H and ^{3}He in addition to α-particles. Results of the relevant state variables from this development are presented and enable comparisons with related but slightly different approaches in the literature. We also comment on some of the sweet and sour aspects of the supra-nuclear EOS. The extent to which the neutron star gravitational and baryon masses vary due to thermal effects, neutrino trapping, magnetic fields and rotation are summarized from earlier studies in which the effects from each of these sources were considered separately. Increases of about 20%($\gtrsim$ 50%) occur for rigid (differential) rotation with comparable increases occurring in the presence of magnetic fields only for fields in excess of 10^{18} Gauss. Comparatively smaller changes occur due to thermal effects and neutrino trapping. Some future studies to gain further insight into the outcome of dynamical simulations are suggested.

3.2 Introduction

The first observation of gravitational waves from the merger of binary neutron stars, now known as GW170817 [A$^+$17c], has given much impetus to ongoing theoretical investigations of the equation of state (EOS) of dense matter. Analysis of the data during inspiral (the phase prior to coalescence) by the LIGO and Virgo collaborations has yielded the chirp mass $\mathcal{M} = (M_1 M_2)^{3/5}/M^{1/5} = 1.188^{+0.004}_{-0.002}\ M_\odot$, where M_1 and M_2 are the companion masses and the total mass $M = M_1 + M_2 = 2.74^{+0.04}_{-0.01}\ M_\odot$. Accounting for the component spins in the range inferred from known spinning neutron stars, the individual masses were determined to be in the range $M_1 = (1.36 - 1.60)\ M_\odot$ and $M_2 = (1.17 - 1.36)\ M_\odot$ when the analysis was restricted to low-spin priors with the dimensionless spin $|\chi| = |J_i c/GM_i^2| \lesssim 0.05$. Of particular relevance to the zero-temperature EOS is the limit set by the data on the dimensionless tidal deformability

[FH08, Fav14]

$$\tilde{\Lambda} = \frac{16}{3}\frac{(M_1 + 12M_2)M_1^4\Lambda_1 + (M_2 + 12M_1)M_2^4\Lambda_2}{(M_1 + M_2)^5}\,. \tag{3.1}$$

For each star, the tidal deformability (or induced quadrupole polarizability) is given by [Lov09]

$$\Lambda_{1,2} = \frac{2}{3}k_2^{1,2}\left(\frac{R_{1,2}c^2}{GM_{1,2}}\right)^5\,, \tag{3.2}$$

where the dimensionless Love number $k_2^{1,2}$ depends on the structure of star, and therefore on the mass and the EOS. Here, G is the gravitational constant, and $R_{1,2}$ are the radii. The computation of $k_2^{1,2}$ with input EOSs is described in refs. [TC67, Hin08, DN09]. For a wide class of neutron star EOSs, $k_2^{1,2} \simeq 0.05$-0.15 [Hin08, HLLR10a, PPL10]. With unconstrained assumptions about the EOS of each of the stars, Ref. [A$^+$17c] sets the limits $\tilde{\Lambda} \lesssim 800$ (for low-spin priors with $|\chi| \lesssim 0.05$) and $\tilde{\Lambda} \lesssim 700$ (for high-spin priors with $|\chi| \lesssim 0.89$).

Recently, ref. [DFL$^+$18] has reported results from a reanalysis of the GW170817 data by imposing the common EOS constraint for the structure of both stars. At the 90% credible interval, the bounds $\tilde{\Lambda} = 222^{+420}_{-138}$ for a uniform component mass prior, $\tilde{\Lambda} = 245^{+453}_{-151}$ for a component consistent with Galactic double neutron stars, and $\tilde{\Lambda} = 233^{+448}_{-144}$ for a component mass tallied with the systematics of radio pulsars have been placed. Across all prior masses, a measurement of the common radius in the range $8.9 < \tilde{R} < 13.2$ km with a mean value $\langle\tilde{R}\rangle = 10.8$ km appears to be consistent with the data. This analysis was performed with polytropic EOSs consistent with constraints from laboratory data up to the nuclear equilibrium or saturation density $n_s \simeq 0.16$ fm^{-3}, microscopic calculations of the zero-temperature EOS up to $\sim 2n_s$, and a large number of extrapolations consistent with causality beyond $2n_s$.

Combining the electromagnetic (EM) [A$^+$17a] and gravitational wave (GW) information from the merger GW170817, ref. [MM17] provides constraints on the radius

$R_{\rm ns}$ and maximum gravitational mass $M^g_{\rm max}$ of a neutron star:

$$\begin{aligned} M^g_{\rm max} &\lesssim 2.17 M_\odot\,, \\ R_{1.3} &\gtrsim 3.1 G M^g_{\rm max} \simeq 9.92\ {\rm km}\,, \end{aligned} \tag{3.3}$$

where $R_{1.3}$ is the radius of a 1.3 $M_\odot$ neutron star and its numerical value above corresponds to $M^g_{\rm max} = 2.17\ M_\odot$.

No evidence of a post-merger signal from GW170817 was found at frequencies up to 4kHZ [A$^+$17c], the interferometer response at higher frequencies precluding the detection of GW waves exhibiting expected quasi-periodic oscillations of the remnant (see refs.[BJ12, BSJ16] and references therein). Promising prospects for future detections of post-merger signals in upgraded LIGO detectors offer the opportunity to explore the EOS beyond the supra-nuclear densities afforded by the current data. Simulations of the post-merger phase require the EOS of neutron-star matter for wide ranges of physical quantities (See refs. [BSJ16, BS10, FR12, Shi15, BR17, PS17], and references therein). The baryon number density ratio n/n_s ranges from 10^{-8}-10, the latter value depending on the constituents of matter in the core of a neutron star. Temperatures up to 100 MeV can be reached during the late stages of the merger. Net electron fractions, $Y_e = n_e/n$, ranging from 0.01-0.6, and entropies per baryon S (in units of k_B) in the range 0-100 have been reported in simulations.

Examples of the entropy and temperature profiles vs baryon mass density in the merger of two equal mass neutron stars after about 7.8 ms subsequent to merger are shown in figs. 3.1 and 3.2, respectively. Thanks are due to David Radice for providing these results obtained using the EOS of Lattimer and Swesty (LS220) [LS91]. The results shown in these figures are drawn from the calculations reported in refs. [BRO$^+$16, ZBR$^+$18, RPZB18]. The neutron star gravitational masses were 1.35 $M_\odot$ each. The rest-mass of the remnant is approximately 2.7-2.8 $M_\odot$. Higher values of S and T are

attained during the later stages of evolution. A black hole forms ~ 20 ms after merger in these calculations.

Gravitational signals from the post-merger remnant with a mass close to the maximum gravitational mass, $M^g_{\rm max}$, or even larger for short times, can provide insight into the possible phases of dense matter complementing that offered by electromagnetic signals. Unlike pulsar signals from neutron stars of mass $\gtrsim 2M_\odot$, gravitational signals after coalescence also enable determination of the thermal properties of dense matter.

One of the main objectives in this paper is to highlight and critically assess the sweet and sour spots of the EOS approaches currently in use. The bulk of sect. 3.3 is devoted toward this end with new contributions that include a comparison of the excluded volume approach [LS91] using the EOS of APR [APR98] for the npα system with the virial approach [HS06] and an extension of the excluded volume approach to include additional light nuclei such as d, ^{3}H and ^{3}He in addition to α-particles. Results of the latter allows for comparisons to be made with earlier works in both of these approaches. Limitations of both of these approaches are also pointed out in this section. Another objective is to address the question of how the masses and radii of neutron stars are affected by thermal effects, composition, trapped neutrinos, magnetic field, and rotation (rigid and differential). Sections 3.4 through 3.7 provide brief reviews of earlier works in which these effects were studied individually along with suggestions for future work that may aid in qualitative and semi-quantitative understanding of the outcome of dynamical simulations of the mergers of binary neutron stars. Our conclusions are in sect. 3.8.

3.3 Sweet and Sour points of the EOS Approaches

Several approaches to the EOS for simulations of core-collapse supernovae, young and old neutron stars, and binary mergers of neutron stars have been developed in the past decades (see ref. [OHKT17] for an extensive review). Owing to the different phases of

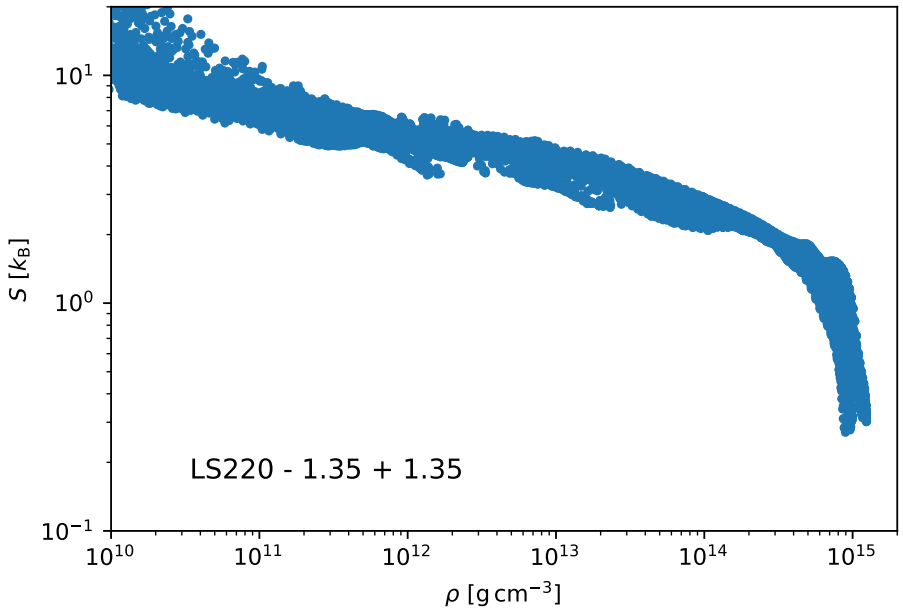

Figure 3.1: Entropy profile of a hyper-massive neuron star during merger. The data represents the meridional plane (i.e., the x-z plane, z being the rotational axis). Results are for the nominal EOS of Lattimer and Swesty (LS220) [LS91] and coalescing neutron stars each of mass $1.35 M_{\odot}$. Figure courtesy of David Radice.

matter encountered at different densities and temperatures, a combination of techniques has been used to calculate the required thermodynamical variables. Broadly speaking, three distinct regions (with different phases and degrees of freedom) in baryon density can be identified: (i) the sub-nuclear density homogeneous and inhomogeneous phases for $n \lesssim 0.1$ fm^{-3}, (ii) near-nuclear density homogeneous phase for $0.1 < n \lesssim 0.3$ fm^{-3}, and (iii) supra-nuclear density with or without phase transitions for $n \gtrsim 0.3$ fm^{-3}. We use the term "homogeneous phase" to refer to a system consisting of hadrons, and leptons of any or all flavors, all regarded as point particles. The same term is also used for supra-nuclear density matter with or without non-nucleonic degrees of freedom. The term "inhomogeneous phase" refers to matter which includes, in addition to nucleons and leptons, composite objects such as light nuclear clusters, heavy nuclei, and pasta-like

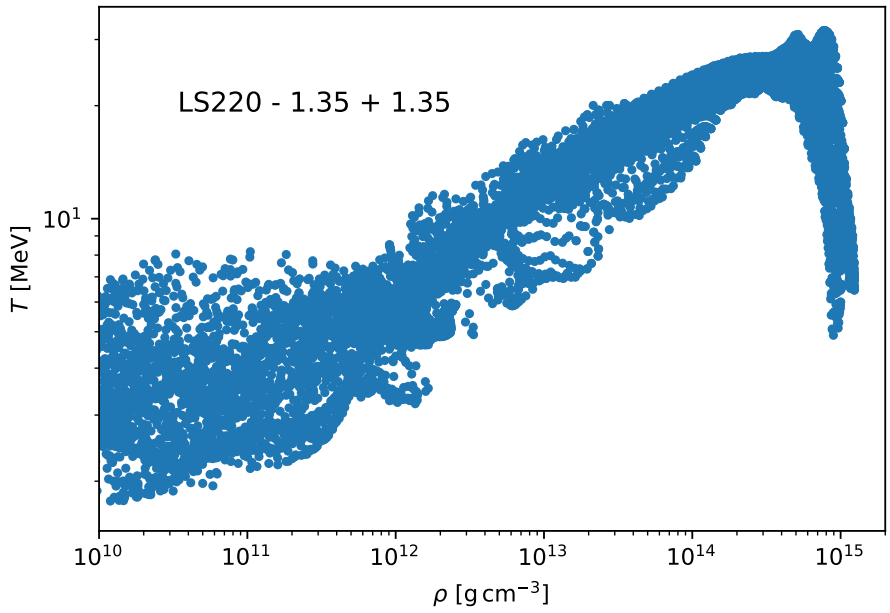

Figure 3.2: Temperature profile of a hyper-massive neuron star during merger. Details as in fig. 3.1. Figure courtesy of David Radice.

configurations in which various geometrical shapes [cylindrical (spaghetti), flat (lasagna), cylindrical holes (anti-spaghetti), spherical holes (swiss cheese)] are permitted [RPW83, PR95].

As the thermal variables depend on n, Y_e, and T, and on neutrino fractions Y_{ν_i} when neutrinos of species $i = e, \mu, \tau$ are trapped in matter, the preferred phase will be determined by the minimization of the total free energy with respect to the appropriate variables. As a result, the concentrations of the various species in both phases depend on (n, Y_e, T). For example, in the range n/n_s = 0.3-0.4 and Y_e = 0.3-0.4 in neutrino-free matter, nuclei with charge and mass numbers well exceeding 70 and 200 exist respectively at T = 2 MeV whereas the corresponding numbers are 30 and 80 at T = 12 MeV. It must be noted, however, that the precise values depend on the underlying nuclear energy density functionals used in the description of bulk homogeneous matter, nuclei and pasta

configurations. For example, typical values of T below which the pasta phase is present are ~ 4 MeV for $Y_e = 0.05$ and ~ 14 MeV for $Y_e = 0.5$ for the EOS of APR [SCMP19]. For charge neutral stellar matter in beta-equilibrium, the dissolution temperature of the pasta phase is around 4-5 MeV (see ref. [RMRR18] which contains an extensive set of references including classical and quantum molecular dynamical calculations).

At very low densities, $n \lesssim 10^{-6}$ fm^{-3}, the abundance of nuclei is generally calculated using the nuclear statistical equilibrium (NSE) approach using mass formulas to calculate the needed chemical potentials μ_i of nuclei (see [OHKT17] for a review and extensive references). The sour point here is that nuclei not encountered in the laboratory will be present and the use of different mass formulas yields different μ_i as extrapolations are required. In this region, interactions between the nucleons and nuclei are small.

With the density approaching 0.1 fm^{-3} and increasing temperature, however, effects of interactions become progressively important. Methods devised to account for interactions include the excluded volume approach, the single-nucleus approximation, the full ensemble method, virial expansion etc. [OHKT17]. Matching the NSE results to those of others is also beset with difficulties. Furthermore, the excluded volume approximation lacks attractive interactions, whereas the virial method requires information about phase shifts not always available from experiments in addition to fugacities exceeding unity in certain regions of n, Y_e, T (see below).

Properties of nucleonic matter in the near-nuclear density region $0.1 < n \lesssim 0.3$ fm^{-3} have received much attention recently from effective field theoretical (EFT) techniques. Among the advantages of EFT is that systematic error estimates can be made, but the drawback is that it cannot be carried through for densities $n \gtrsim 0.3$ fm^{-3} due to the perturbative expansion scales reaching invalid regions as the density increases toward the central densities of neutron stars of increasing masses. For the same reason, the

exploration of non-nucleonic degrees of freedom such as Bose condensates or quarks is beyond EFT at the current time.

The discussion above highlights some of the sweet and sour aspects of the current status of dense matter theory. Clearly, advances in each of the three density regions mentioned above are needed for a fuller microscopic understanding of nuclear matter to better explain astrophysical phenomena.

3.3.1 Instabilities in the Sub-Nuclear Phase of Nucleonic Matter

Our considerations in this subsection are more relevant for the matter produced in intermediate energy heavy ion collisions than for stellar matter discussed in the next subsection. However, the discussion here sets the stage for the case when electrons are present in stellar matter. A uniform phase of nucleonic matter becomes mechanically unstable (also referred to as spinodally unstable) at sub-nuclear densities, $n < n_s$, for which the compressibility $K(n) = 9\ dP/dn \leq 0$, where $P = n^2(dE/dn)$ is the pressure. The energy E and pressure of isospin asymmetric matter with $u = n/n_s$ and neutron excess $\alpha = (n_n - n_p)/n(= n_n + n_p)$ can be written as

$$E(u,\alpha) = E(u,0) + \alpha^2 S_2(u) + \ldots \tag{3.4}$$

$$\frac{P(u,\alpha)}{n_s} = u^2\left[E'(u,0) + \alpha^2 S_2'(u)\right] + \ldots\,, \tag{3.5}$$

where the nuclear symmetry energy $S_2(u) = \frac{1}{2}\frac{\partial^2 E(u,\alpha)}{\partial\alpha^2}\Big|_{\alpha=0}$ and the prime denotes derivative with respect to u. Higher order terms in α are generally small as

$S_2(u) >> S_4(u),\ S_6(u), \ldots$ (only even powers of α contribute as the two species are treated symmetrically in the Hamiltonian because of the near-complete isospin invariance of the nucleon-nucleon interaction). As a result,

$$\frac{\partial(P(u,\alpha)/n_s)}{\partial u} \simeq 2uE'(u,0) + u^2E''(u,0) + \alpha^2\left[2uS_2'(u,0) + u^2S_2''(u,0)\right]. \tag{3.6}$$

An estimate of the density at which the spinodal instability sets in for $T = 0$ symmetric nuclear matter (SNM) with $\alpha = 0$, or proton fraction $x = (1 - \alpha)/2 = 1/2$, can be made using the quadratic approximation to the energy vs density close to $u = 1$:

$$E(u, 0) = -B.E + \frac{K_s}{18}(u - 1)^2 , \tag{3.7}$$

where $B.E. = 16 \pm 1$ MeV is the binding energy of SNM and $K_s = (230 \pm 30)$ MeV is its compression modulus. The pressure P and its density derivative thus become

$$\frac{P}{n_s} = \frac{K_s}{9}u^2(u - 1) , \quad \frac{d(P/n_s)}{du} = \frac{1}{3}K_s u\left(u - \frac{2}{3}\right) . \tag{3.8}$$

Spinodal instability sets in at the density $n_{\rm sp} = (2/3)n_s \simeq 0.11$ fm^{-3} for SNM, independent of K_S. This estimate for $n_{\rm sp}$ is not greatly affected by the skewness of the EOS around u, which would add a term $\propto (u - 1)^3$ to eq. (3.7). For the EOS of Akmal, Pandharipande and Ravenhall (APR) [APR98], $n_{sp} \simeq 0.10$ fm^{-3}; other EOSs in current use have similar values of n_{sp}. With increasing neutron excess ($\alpha \to 1$), or decreasing proton fraction ($x \to 0$), the quadratic approximation in $E(u, 0)$ or $S_2(u)$ around $u = 1$ becomes inadequate [CMPL14]. In this case, $n_{\rm sp}(u, x)$ can be found from the density ratio u at which eq. (3.6) vanishes for each x. For $x \neq 0.5$, the first and second density derivatives of both $E(u, 0)$ and $S_2(u)$ determine $n_{\rm sp}(n, x)$, which decreases from its value for SNM; e.g., $n_{\rm sp}(n, 0.1) \simeq 0.05$ fm^{-3} for the EOS of APR. Other EOSs yield similar qualitative results, quantitative differences being small.

Thermal effects, which provide positive contributions to the total energy and pressure, also influence the stability of uniform nucleonic matter at sub-nuclear densities. The onset of the liquid-gas phase transition, determined by the requirements

$$\left.\frac{dP}{dn}\right|_{n_c,T_c} = \left.\frac{d^2P}{dn^2}\right|_{n_c,T_c} = 0 , \tag{3.9}$$

occurs at the critical density $n_c \simeq 0.06$ fm^{-3} and critical temperature $T_c \simeq 17.9$ MeV, respectively, for SNM using the EOS of APR [CMPL14]. Although $T_c/T_c(x = 0.5)$ drops

significantly with decreasing x, the ratio $P_c/(n_c T_c)$ remains very close to 0.347 for x in the range 0.1-0.5 (see fig. 9 of ref. [CMPL14]). Qualitative features of the above results are generic to other EOSs in common use. For example, for the Skyrme EOS parametrization Ska for which $T_c = 15.12$ MeV, $P_c/(n_c T_c) = 0.303$, again with little variation in the range of $x = 0.1 - 0.5$ [CMPL14].

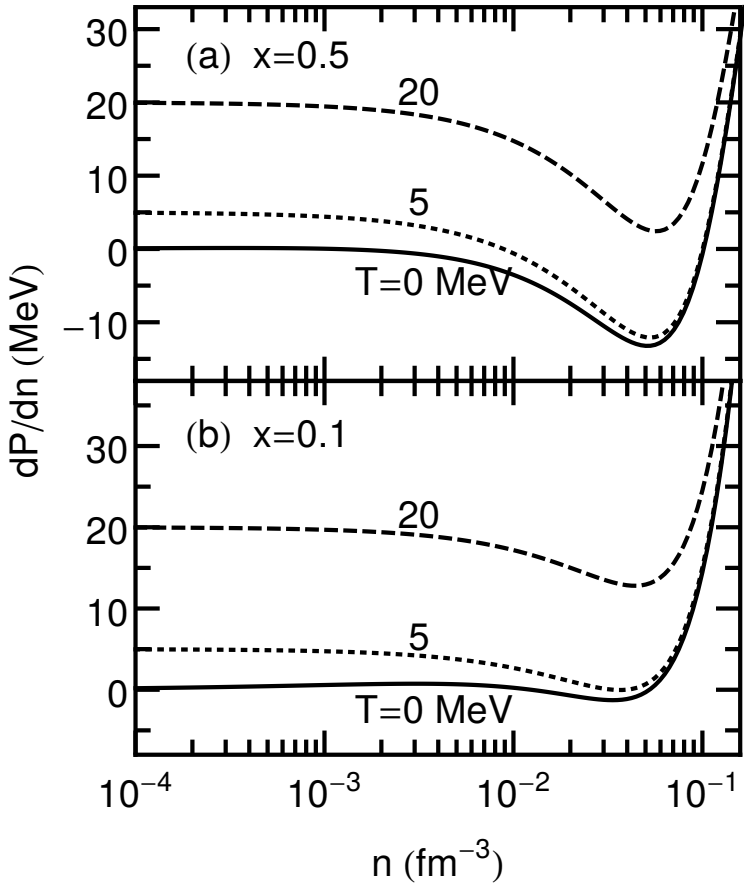

Figure 3.3: Derivative of the pressure of nucleons with respect to density vs density at the indicated temperatures T and proton fractions x.

Figure 3.3 shows the pressure derivative (with respect to density) of the bulk phase of nucleons for different temperatures and proton fractions. In SNM ($x = 0.5$), the spinodal

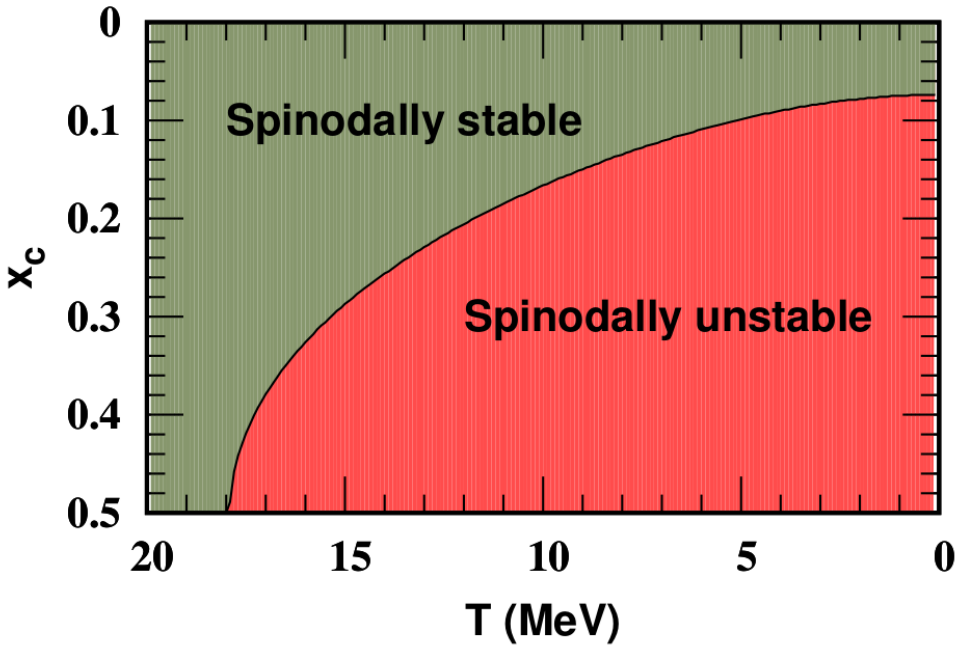

Figure 3.4: Spinodally stable and unstable regions in nucleonic matter for the APR model with x_c denoting the proton fraction above which $dP/dn \geq 0$ for all n.

region can be clearly identified for the lowest two temperatures shown. For the same x but at $T = 20$ MeV, the spinodal instability is absent as this temperature exceeds the liquid-gas phase transition temperature $T_c = 17.91$ MeV for this model. As the proton fraction decreases toward that of pure neutron matter (PNM), the instability region shrinks in size as fig. 3.3(b), in which $x = 0.1$, shows. Results for intermediate values of x show similar trends [CMPL14]. The value of x_c below which the spinodal density disappears, i.e., for which $dP/dn \geq 0$, is shown as a function of T in fig. 3.4 with the spinodally stable and unstable regions indicated. For all $T > T_c$, there is no density interval for which spinodal instability occurs as eq. (3.9) guarantees $dP/dn > 0$ for all n. The qualitative behavior of this curve is also exhibited in other models of the EOS [CMPL14].

At the densities and temperatures for which the homogeneous uniform phase of nucleonic matter is unstable, an inhomogeneous phase of matter consisting of light

nuclear clusters such as d, ^{3}H,^{3} He, α, etc. and heavier nuclei in addition to nucleons becomes energetically favorable.

3.3.2 Stability of the Sub-Nuclear Phase in Stellar Matter

Through beta decays and electron capture processes involving nucleons and nuclei, a uniform background of electrons would also be present in charge neutral stellar matter. The concentration of each species is determined by the conservation equations for baryon number and charge neutrality together with the minimization of the total free energy with respect to the appropriate internal variables (see below). Earlier work [LS91, BBP71, LLPR85] has identified three phases of matter depicted in fig. 3.5. The generic features shown in this figure are for the EOS of APR adopting the excluded volume treatment of ref. [LS91] for nuclei and for a typical net electron fraction Y_e. Similar features are obtained by using other EOSs and for other Y_e's albeit with quantitative differences.

In phase I of fig. 3.5, only nucleons, light nuclei (d, ^{3}H,^{3} He, α, etc.), and a uniform background of leptons (mostly electrons and positrons, and smaller amounts of muons at high enough T's) to maintain charge neutrality, and photons would be present. Phase II is characterized by the presence of light and heavy nuclei, many rather neutron rich. In a very small region close to $n \simeq 0.1$ fm^{-3}, exotic shapes of nuclei commonly called pasta configurations are also energetically favored. With density increasing beyond $n = 0.1$ fm^{-3}, the dissolution of all nuclei in the inhomogeneous phase gives way to the uniform phase III of nucleons with charge balancing leptons, and photons.

At supra-nuclear densities beyond 2-3 n_s, matter may also consist of Δ-isobars, Bose (pion, kaon, charged ρ-mesons, etc.) condensates, hyperons and/or quarks [Pra96]. At these densities, the effects of baryon superconductivity and superfluidity on the EOS are negligible as the associated gap parameters are small, $\sim$ 1-2 MeV, compared to the other

energy scales in dense matter. However, their effects on the long-term cooling of cold-catalyzed neutron stars through neutrino emission are important in interpreting the observed surface temperatures (see the compendium of contributions in ref. [PLPS15]). This latter subject is not covered here as it falls outside the scope of this article.

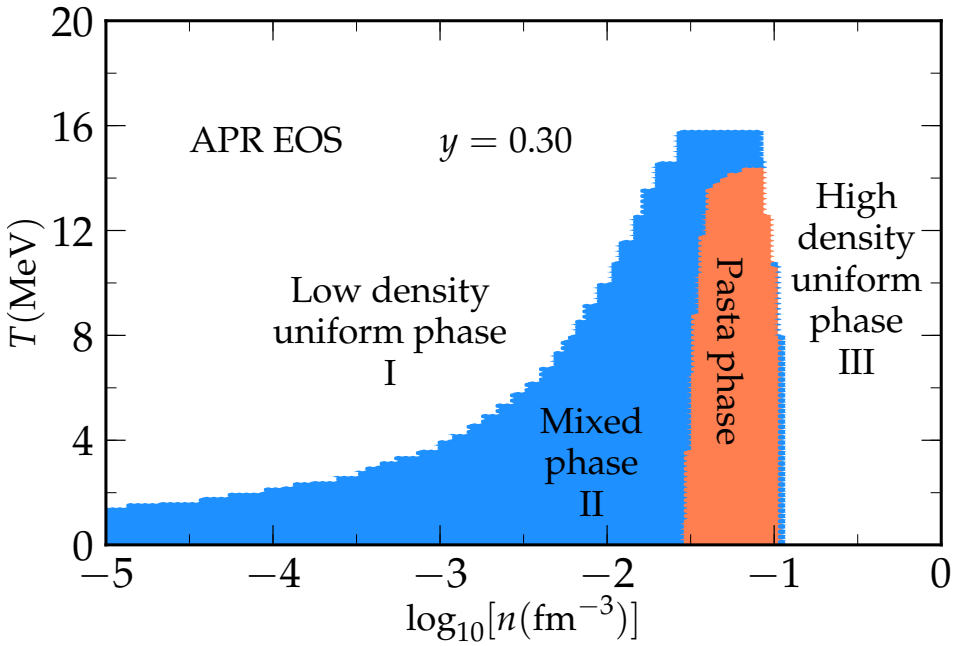

Figure 3.5: Phases in dense stellar matter. Figure courtesy of Andre Schneider.

Electrons restore stability

To highlight the role of electrons in the sub-nuclear phase, we first consider the case in which only nucleons and electrons are present. In this case, the conservation of baryon number and charge neutrality yield $n_n = n(1-x)$ and $n_p = nx = n_e$. Minimizing the total free energy density $F(n, x, T)$ with respect to x gives the energy balance relation between the chemical potentials:

$$\begin{aligned} \hat{\mu} &= \mu_n - \mu_p = \mu_e \,, \\ &\simeq 4(1-2x)\left[S_2(n) + 2S_4(n)(1-2x)^2 + \cdots\right] , \end{aligned} \tag{3.10}$$

which highlights the role of the nuclear symmetry energy. The pressure is then found from $P = n^2\ \partial(F/n)/\partial n|_{x,T}$ from which the derivative $(\partial P/\partial n)|_{x,T}$ can be calculated. Figure 3.6 shows results of this derivative for representative values of x and T as functions of n. The results here were calculated without approximation using the Hamiltonian density of APR for the nucleons with electrons being treated as a free Fermi gas.

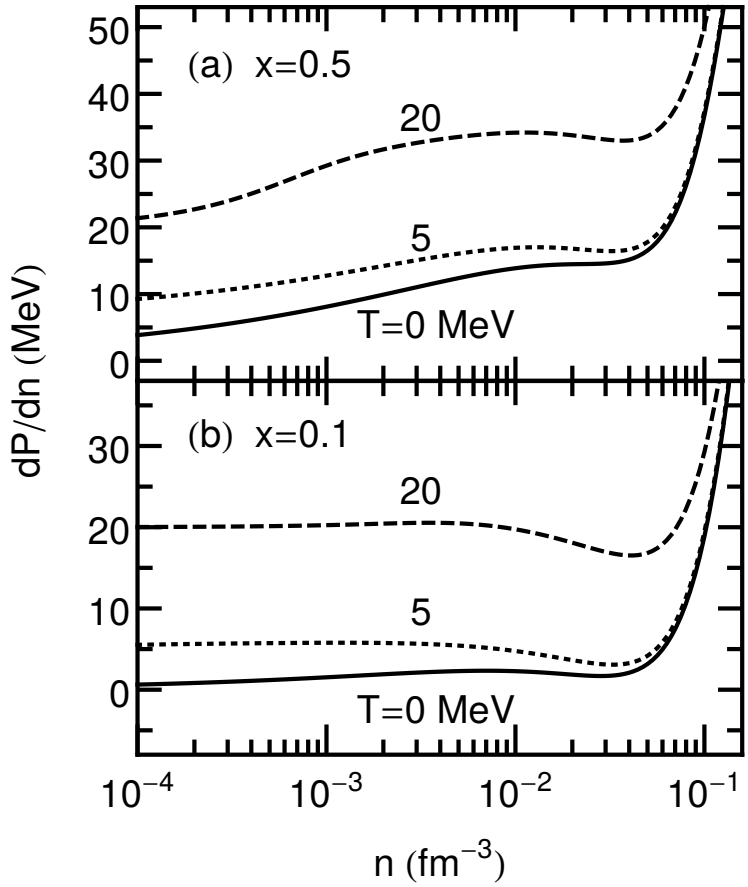

Figure 3.6: Derivative of the pressure of nucleons and electrons with respect to density vs density for the indicated temperatures and proton fractions.

It is clear from fig. 3.6 that contributions from electrons to the total pressure *entirely remove the mechanical (spinodal) instability* present in baryons-only matter for all x and

T. A similar conclusion was reached by ref. [CMPL15b] in which the adiabatic index $\Gamma_S = (n/P)(\partial P/\partial n)|_S$, where S is the entropy per baryon, was calculated (in Sec. VI there) for other nonrelativistic models (MDYI and SkO′) and a mean field theoretical model of nucleons. This conclusion also applies for charge neutral and beta-stable neutron star matter at both zero and finite temperatures for which the equilibrium proton fraction $\tilde{x}$ varies with n. In this case, the requirement that pressure be a continuously increasing function of n in a stable star assures stability against spinodal collapse. Note also that baryons-only matter is mechanically stable at all T for roughly $x < 0.1$. For these proton fractions, electrons are required only for the purposes of charge neutrality.

3.3.3 Inclusion of light Nuclear Clusters

Although electrons restore mechanical stability in stellar matter, the presence of light nuclear clusters such as d,^{3}H,^{3}He, α, etc. lowers the free energy and thus becomes the favored state of matter in phase I of fig. 3.5. In what follows, we discuss the excluded volume and virial approaches commonly used for treating the presence of these light nuclear clusters. An extension of the excluded volume approach of refs. [LS91, LLPR85] to include other clusters beyond α-particles will be presented. A comparison of the excluded volume and virial approaches for the npα system with leptons and photons will be made together with a brief discussion of the advantages and drawbacks of each of these approaches.

The excluded volume approach with α- particles

With a binding energy $B_\alpha \simeq 28.3$ MeV, α-particles are the most bound among the light nuclear clusters. The discussion here to include α- particles in addition to nucleons, electrons, and photons follows closely that of ref. [LS91] which, in turn, is a simplified version of an earlier treatment in ref. [LLPR85]. We first outline the procedure of ref.

[LS91] here as it paves the way for the subsequent inclusion of additional light nuclear clusters in this approach.

Interactions between α-particles and nucleons (assumed to be point particles) are taken into account by treating the α-particles as rigid spheres of volume

$v_\alpha = \frac{4\pi}{3}(\frac{4}{5}a_{\mathrm{p}\alpha})^3 \simeq 24$ fm^3, where $a_{\mathrm{p}\alpha}$ is the proton-α scattering length. This treatment accounts for repulsive interactions only, attractive interactions being deemed as small. The conservation equations for baryon number and charge neutrality are

$$n = 4n_\alpha + (n_{n\mathrm{o}} + n_{p\mathrm{o}})(1 - n_\alpha v_\alpha) \tag{3.11}$$

$$nY_e = 2n_\alpha + n_{p\mathrm{o}}(1 - n_\alpha v_\alpha)\,, \tag{3.12}$$

where $n_{n\mathrm{o}}$ and $n_{p\mathrm{o}}$ are the neutron and proton densities outside the α-particles of density n_α, and $Y_e = n_e/n$ is the net electron fraction (i.e., $n_e = n_{e^-} - n_{e^+}$). Equation (3.11) enables the mass fractions to be defined as

$$\begin{aligned} X_\alpha &= 4\frac{n_\alpha}{n}\,, \\ X_{n\mathrm{o}} &= \frac{n_{n\mathrm{o}}(1 - n_\alpha v_\alpha)}{n}\,, \quad X_{p\mathrm{o}} = \frac{n_{p\mathrm{o}}(1 - n_\alpha v_\alpha)}{n}\,. \end{aligned} \tag{3.13}$$

The total free energy density can be decomposed as

$$F = F_b + F_e + F_\gamma\,, \tag{3.14}$$

where $F_b = F_{\mathrm{o}} + F_\alpha$ is the free energy density of baryons, F_e and F_γ are those of the leptons and photons. The component F_{o} refers to the outside (of α-particles) nucleons and can be written as

$$F_{\mathrm{o}} = (1 - n_\alpha v_\alpha)\, n_{\mathrm{o}} f_{\mathrm{o}}(n_{\mathrm{o}}, x_{\mathrm{o}}, T)\,, \tag{3.15}$$

where f_{o} is the free energy per nucleon, $n_{\mathrm{o}} = n_{n\mathrm{o}} + n_{p\mathrm{o}}$ and $x_{\mathrm{o}} = n_{p\mathrm{o}}/n_{\mathrm{o}}$. The quantity f_{o} can be calculated using a suitable model for the EOS of interacting nucleons. Here we use that of APR at finite T following ref. [CMPL14] where details for calculating F_e and F_γ

are also provided. The α-particles are treated as non-interacting Boltzmann particles, whence

$$F_\alpha = n_\alpha(\mu_\alpha - B_\alpha - T)\,. \tag{3.16}$$

The α-particle chemical potential, easily obtained from the classical gas expression $n_\alpha = 8n_Q \exp(\mu_\alpha/T)$, is

$$\mu_\alpha = T\ln\left(\frac{n_\alpha}{8n_Q}\right) \quad \text{with} \quad n_Q = \left(\frac{mT}{2\pi\hbar^2}\right)^{3/2}\,, \tag{3.17}$$

where n_Q is the quantum concentration of nucleons with m denoting the nucleon mass. Being non-interacting particles, the α-particle pressure, energy density and entropy density are

$$\begin{aligned} P_\alpha &= n_\alpha T\,, \quad \epsilon_\alpha = n_\alpha\left(\frac{3}{2}T - B_\alpha\right)\,, \quad \text{and} \\ s_\alpha &= n_\alpha\left(\frac{5}{2} - \frac{\mu_\alpha}{T}\right)\,. \end{aligned} \tag{3.18}$$

Minimization of F with respect to n_α yields the relationship between the chemical potentials of the baryons:

$$0 = \frac{\partial F}{\partial n_\alpha} \Rightarrow \mu_\alpha = 2(\mu_{n\mathrm{o}} + \mu_{p\mathrm{o}}) + B_\alpha - p_\mathrm{o} v_\alpha\,, \tag{3.19}$$

where p_o is the pressure of nucleons outside the α-particles obtained using the (purely nucleonic) EOS at the given (subnuclear) density, lepton fraction, and temperature. Because the EOS of APR uses a common value for the rest masses for the neutron and proton, the term involving $2(m_p - m_n)$ is not included in the above equation.

In simulations of core-collapse supernovae, proto-neutron stars and binary mergers of neutron stars, the EOS is generally tabulated in terms of the variables (n, Y_e, T). From a numerical standpoint, it is advantageous to extend the variables to (n, Y_e, X_p, T), where $X_p = n_{p\mathrm{o}}/n$. Eliminating n_α from eqs. (3.11) and (3.12), one obtains

$$\begin{aligned} n_o &= \frac{2n(1-2Y_e) + nX_p(4 - nv_\alpha)}{2 - nY_e v_\alpha} \\ n_{po} &= nX_p\,, \quad n_{no} = n_o - n_{po}\,, \quad \text{and} \quad x_o = \frac{n_{po}}{n_o}\,. \end{aligned} \tag{3.20}$$

Thus n_{po} and n_{no} are completely determined by specifying (n, Y_e, T) and providing a guess value for X_p. With these n_{po} and n_{no} at hand, μ_{po} and μ_{no} [needed for the calculation of n_α using eq. (3.17)] can be obtained by solving

$$2\int \frac{d^3p}{(2\pi\hbar)^3}\frac{1}{1+\exp\left(\frac{e_i-\mu_i}{T}\right)} - n_i = 0 \tag{3.21}$$

where the spectra e_i correspond to the model of choice for the nucleonic EOS. The value of X_p can then be updated iteratively to satisfy the baryon number conservation eq. (3.11). The total pressure, entropy density and energy density are then

$$\begin{aligned} P &= P_{\rm o} + P_\alpha + P_e + P_\gamma\,, \\ s &= (1-n_\alpha v_\alpha)s_{\rm o} + s_\alpha + s_e + s_\gamma \quad S = s/n \\ \epsilon &= \sum_i \mu_i n_i + Ts - P\,, \quad E = \epsilon/n\,, \end{aligned} \tag{3.22}$$

where S denotes the total entropy per baryon, E the total energy per baryon and $P_o = (1-n_\alpha v_\alpha)\, p_o$. In utilizing the thermodynamic relation above to obtain the energy density, it is necessary to account for the α-particle binding energy B_α in the total chemical potential of the α, i.e., $\mu_\alpha^{\rm tot} = \mu_\alpha - B_\alpha$. We defer presentation of the numerical results of these state variables to a later section.

The excluded volume approach with multiple clusters

The presence of additional light nuclear clusters such as d, ^{3}H, and ^{3}He give a lower free energy relative to the case when only α-particles are considered besides nucleons. The binding energies of these light nuclei are listed in table 3.1. In the excluded volume approach, interactions between the various nuclear species and nucleons can also be included by treating these nuclei as rigid spheres with excluded volumes $v_i = \frac{4}{3}\pi R_i^3$, where the sharp sphere radii R_i can be inferred from the measured charge or mass rms radii, the latter not being experimentally available yet. Values of $v_i,\ i =$ d, ^{3}H, ^{3}He and ^{4}He are also listed in Table 3.1. Note that v_α differs slightly from that used in refs. [LS91, LLPR85].

Table 3.1: Properties of light nuclei. The symbol for each nucleus used in text is as indicated. The symbol v stands for the rigid sphere effective excluded volume.

Nucleus	Symbol	B.E. (MeV)	v (fm^3)
d	d	2.22	40.5
^{3}H	τ	8.48	23.2
^{3}He	3	7.72	32.0
^{4}He	α	28.3	19.9

The baryon number conservation equation takes the form

$$\begin{aligned} n &= 4n_\alpha + (1 - n_\alpha v_\alpha) \\ &\times \{3n_3 + (1 - n_3 v_3) \\ &\times [3n_\tau + (1 - n_\tau v_\tau) \\ &\times (2n_d + n_o(1 - n_d v_d))]\} \,. \end{aligned} \tag{3.23}$$

Note that the order by which the excluded volumes are nested does not affect the final results for the thermodynamic state variables as functions of (n, Y_e, T) insofar as a particular order is used consistently over the course of the calculation.

The mass fractions are defined as

$$\begin{aligned} X_\alpha &= \frac{4n_\alpha}{n} \,, X_3 = \frac{3n_3}{n}(1 - n_\alpha v_\alpha) \,, \\ X_\tau &= \frac{3n_\tau}{n}(1 - n_\alpha v_\alpha)(1 - n_3 v_3) \,, \\ X_d &= \frac{2n_d}{n}(1 - n_\alpha v_\alpha)(1 - n_3 v_3)(1 - n_\tau v_\tau) \,, \\ X_{n\mathrm{o}} &= \frac{n_{n\mathrm{o}}}{n} \prod_i (1 - n_i v_i) \,, X_{p\mathrm{o}} = \frac{n_{p\mathrm{o}}}{n} \prod_i (1 - n_i v_i) \,. \end{aligned} \tag{3.24}$$

with $i = d, 3, \tau, \alpha$. The corresponding charge neutrality condition requires

$$\begin{aligned} nY_e &= 2n_\alpha + (1 - n_\alpha v_\alpha) \\ &\times \{2n_3 + (1 - n_3 v_3) \\ &\times [n_\tau + (1 - n_\tau v_\tau) \\ &\times \left(n_d + n_{po}(1 - n_d v_d)\right)]\} \,. \end{aligned} \tag{3.25}$$

When all of the nuclear species are treated as non-interacting Boltzmann particles, their densities, chemical potentials and "bare" (i.e., without excluded volume factors included) free energy densities are given by

$$\begin{aligned} n_i &= A_i^{3/2} n_Q \exp(\mu_i / T) \\ \mu_i &= T \ln\left(\frac{n_i}{A_i^{3/2} n_Q}\right) \\ f_i &= n_i(\mu_i - B_i - T) \quad i = d, \tau, 3, \alpha \,, \end{aligned} \tag{3.26}$$

where A_i are the mass numbers of the light nuclei and n_Q is the quantum concentration of nucleons in eq. (3.17). The pressure, energy density and entropy density of each species is that of a non-interacting gas as in eq. (3.18). As in the previous section, the free energy densities of interacting nucleons outside the nuclei are calculated using the EOS of APR at finite T [CMPL14].

The relationships between the various chemical potentials are obtained by minimizing the total free energy density

$$\begin{aligned} F &= F_b + F_e + F_\gamma \\ F_b &= F_{\rm o} + F_d + F_\tau + F_3 + F_\alpha \\ F_{\rm o} &= \prod_{i=d,\tau,3,\alpha} (1 - n_i v_i)\, n_{\rm o} f_{\rm o}(n_{\rm o}, x_{\rm o}, T) \\ F_{\rm d} &= \prod_{i=\tau,3,\alpha} (1 - n_i v_i)\, f_{\rm d}(n_{\rm d}, T) \\ F_\tau &= \prod_{i=3,\alpha} (1 - n_i v_i)\, f_\tau(n_\tau, T) \\ F_3 &= (1 - n_\alpha v_\alpha)\, f_3(n_3, T) \\ F_\alpha &= f_\alpha(n_\alpha, T) \end{aligned} \tag{3.27}$$

with respect to n_i:

$$\begin{aligned} \frac{\partial F}{\partial n_i} &= 0 \Rightarrow \\ \mu_d &= \mu_{no} + \mu_{po} + B_d - v_d p_o \\ \mu_\tau &= 2\mu_{no} + \mu_{po} + B_\tau - v_\tau(p_o + n_d T) \\ \mu_3 &= \mu_{no} + 2\mu_{po} + B_3 - v_3(p_o + n_d T + n_\tau T) \\ \mu_\alpha &= 2(\mu_{no} + \mu_{po}) + B_\alpha - v_\alpha(p_o + n_d T + n_\tau T + n_3 T)\,, \end{aligned} \tag{3.28}$$

where $p_{\rm o}$ stands for the pressure of interacting nucleons in the absence of the light nuclei. The inclusion of additional clusters increases the number of quantities to be determined compared to the case when only α-particles are considered. As in the previous section, the set of variables (n, Y_e, X_p, T) facilitates numerical evaluations considerably. The nucleon densities outside the nuclei can be found by eliminating n_α from eqs. (3.23) and (3.25) and

a guess value of X_p:

$$\begin{aligned}
n_o &= \left\{\left[Q\frac{1}{1-n_3v_3} - 3n_\tau\right]\frac{1}{1-n_\tau v_\tau} - 2n_d\right\}\frac{1}{1-n_d v_d} \\
Q &= \left(\frac{2n(1-2Y_e) + R(4-nv_\alpha)}{2-nY_e v_\alpha} - 3n_3\right) \\
R &= 2n_3 + (1-n_3v_3) \\
&\times \left\{n_\tau + (1-n_\tau v_\tau)\left[n_d + nX_p(1-n_d v_d)\right]\right\} \\
n_{no} &= n_o - n_{po}\,, \quad x_o = \frac{n_{po}}{n_o} \quad \text{and} \quad n_{po} = nX_p
\end{aligned} \tag{3.29}$$

using which the outside nucleon chemical potentials can be determined by utilizing their relations to the nucleon densities. Equation (3.28) then provides the various chemical potentials and eq. (3.26) their corresponding densities. The correct value of X_p can be determined iteratively by satisfying the baryon number conservation eq. (3.23). The total pressure is then given by

$$\begin{aligned}
P &= P_b + P_e + P_\gamma \\
P_b &= P_{\rm o} + P_d + P_\tau + P_3 + P_\alpha \\
P_{\rm o} &= \prod_{i=d,\tau,3,\alpha} (1-n_i v_i)\; p_{\rm o}(n_{\rm o}, x_{\rm o}, T) \\
P_{\rm d} &= \prod_{i=\tau,3,\alpha} (1-n_i v_i)\; p_{\rm d}(n_{\rm d}, T) \\
P_\tau &= \prod_{i=3,\alpha} (1-n_i v_i)\; p_\tau(n_\tau, T) \\
P_3 &= (1-n_\alpha v_\alpha)\; p_3(n_3, T) \\
P_\alpha &= p_\alpha(n_\alpha, T) \\
p_i &= n_i T
\end{aligned} \tag{3.30}$$

Expressions for the entropy and energy densities are similar with $s_{\rm o}$ and $\epsilon_{\rm o}$ taking the place of $p_{\rm o}$, and the various other p_i's above replaced by $s_i = n_i(5/2 - \mu_i/T)$ and $\epsilon_i = n_i(3/2T - B_i)$ for $i = d, \tau, 3, \alpha$, respectively.

The Virial Approach

The treatment of clusters is also afforded by the virial expansion approach that includes bound and continuum states, and provides corrections to the ideal gas results for thermal variables [BU37]. When applicable, this approach is model independent as experimental data (i. e., phase shifts), where available, are input to theory. In terms of the partition function Q, the pressure $P = (T/V) \log Q$, and is expressed in terms of the fugacities $z_i = \exp(\mu_i/T)$, (i = d, ^{3}H, ^{3}He, ^{4}He etc.) and the 2nd virial coefficients b_2 which are simple integrals involving thermal weights and elastic scattering phase shifts. Unlike in classical statistical mechanics, a satisfactory treatment of the 3rd and higher order quantum virial coefficients is yet to be accomplished.

In the context of heavy-ion collisions, this approach was used to calculate the state variables of a resonance gas in ref. [VP97]. For low-density supernova and neutron-star matter, the EOS for the npα system was calculated in ref. [HS06], with the inclusion of other light nuclear clusters in refs. [OGH$^+$07, A$^+$08] and those with heavy-nuclei also in ref. [SHT10]. The review in ref. [OHKT17] provides an extensive list of other references in which the virial approach and its extensions have been used to calculate the EOS of low-density matter.

Here we restrict ourselves to the npα system with electrons and photons to make comparisons with the results of the excluded volume approach, and to point out similarities and differences. The results reported here were obtained precisely in the manner expounded in refs. [HS06] and [LS91] respectively, with APR serving as the underlying model for the nucleon-nucleon force in the latter case. In both cases, we have verified that our results shown here reproduce those of these earlier works.

Comparison between the Excluded Volume and Virial Approaches

We begin by showing results for the npα system with leptons and photons. Figure 3.7 shows a comparison of the α-particle mass fractions $X_\alpha = 4n_\alpha/n$ between the excluded volume approach using the EOS of APR for nucleons and the virial approach. Unlike in the standard LS model, X_α's here lie above the virial results until they vanish at some density (see fig. 5 and associated discussion in ref. [HS06]). Clearly, results of the excluded volume approach depend on the treatment of the nucleon-nucleon interactions. As noted in refs. [LS91, LLPR85], the $p_o v_\alpha$ term in eq. (3.19) decreases the μ_α and n_α as the density increases causing the disappearance of α's. Such is not the case in the virial approach in which for each Y_e, X_α's continue to increase up to and even beyond n_s where the approach becomes invalid. However, the appearance of heavy-nuclei at sub-nuclear densities results in diminishing X_α's in the virial approach as well [SHT10]. The physical difference between the two approaches is that only repulsive interactions are incorporated in the excluded volume approach whereas in the virial approach the α-nucleon interactions are predominantly attractive. In what follows, we will first present results from each of these approaches to provide a comparison and to appreciate their characteristics before addressing a method in which the limitations of each method can be avoided.

Figures 3.8(a) and (b) show the pressure vs baryon density in the two approaches at $T = 4$ MeV, and for $Y_e = 0.1$ and 0.4, respectively. The individual contributions from the baryons presented in this figure provide a contrast between results of the excluded volume approach (solid curves) using the EOS of APR for nucleons and the virial (dashed curves) approach. Unlike in the virial approach, the excluded volume pressure due to the outside nucleons, P_o, shows a non-monotonic behavior for both Y_e's. This difference is due to the disappearance of the α-particles with growing density in the excluded volume approach. Particularly noteworthy are the negative values of P_o for $Y_e = 0.4$ characteristic of nearly symmetric nucleonic matter at the densities shown [CMPL14]. This feature is absent in

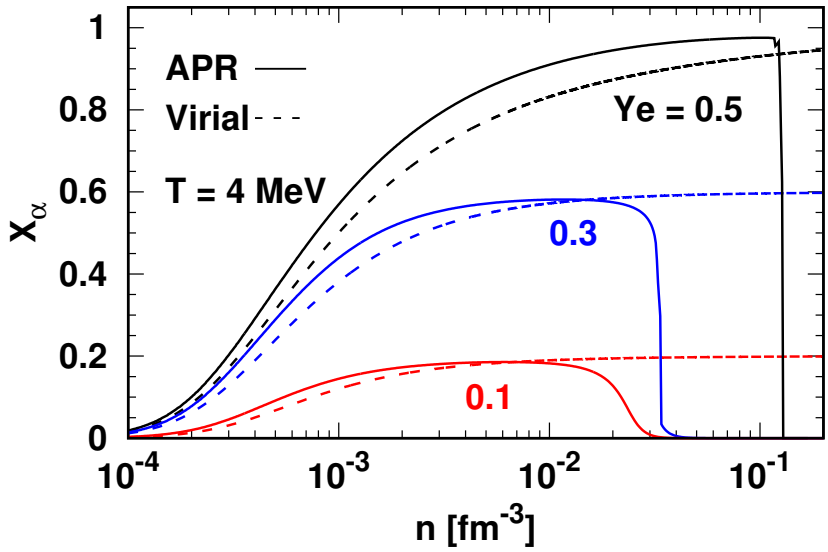

Figure 3.7: Mass fractions $X_\alpha = 4n_\alpha/n$ vs baryon density at the indicated temperature T and net electron fractions Y_e.

the virial approach. The sub-dominant contributions P_α from the α-particles are nearly the same in the two approaches. For both Y_e's, the contribution from the leptons, P_e, is dominant over that of the baryons. This dominance persists for all values of Y_e's except those approaching that of PNM for which $Y_e = 0$. The contribution from photons is negligible at the temperature and densities shown. We note, however, that these results, along with those of other state variables to be shown below, will be quantitatively altered when other light nuclear clusters as well as heavy nuclei are included at sub-nuclear densities.

The entropy per baryon, $S = s/n$, vs n is shown in figs. 3.9(a) and (b) for the same T and Y_e's as in fig. 3.8. The upward trend in the results for S_o and S_e is caused by the low values of n in their respective definitions. As with the pressures, the non-monotonic behavior of S_o at the higher end of densities in this figure is caused by the disappearance

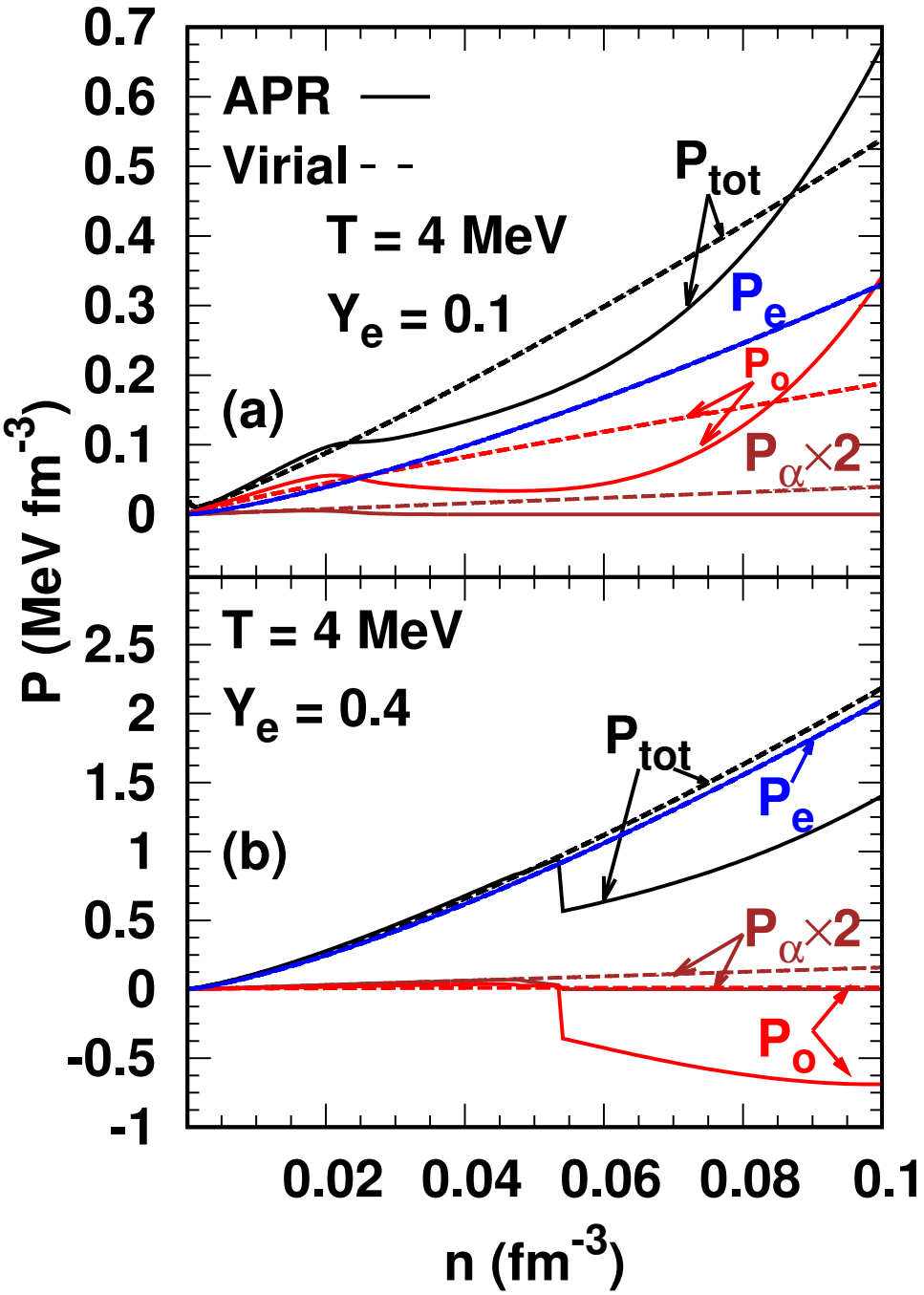

Figure 3.8: Pressure vs baryon density in the excluded volume and virial approaches for the indicated temperature and net electron fractions. Low individual contributions have been multiplied by a factor of 2 for clarity.

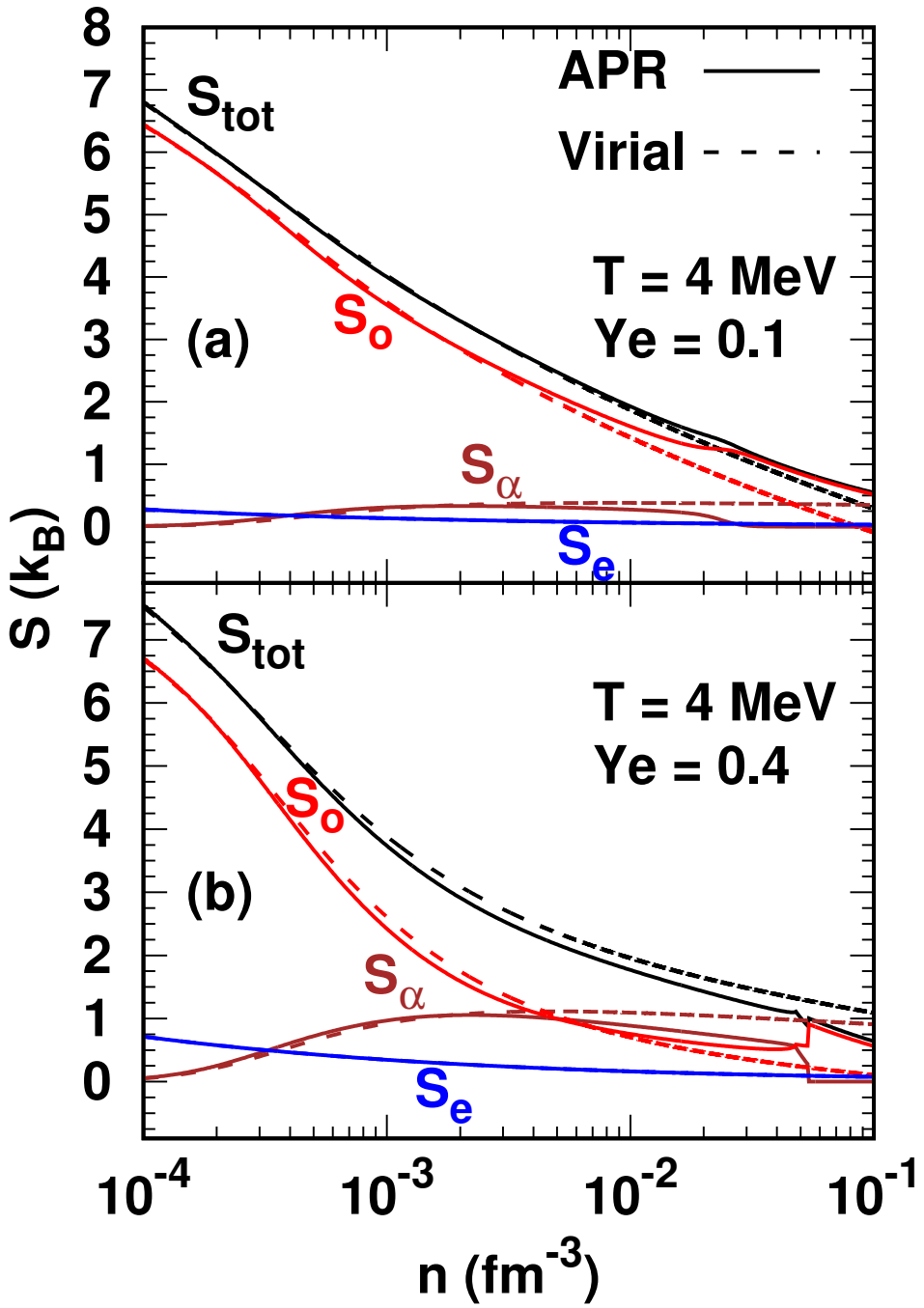

Figure 3.9: Same as fig. 3.8, but for the entropy per baryon vs baryon number density.

of α-particles in the excluded volume approach. As n_α vanishes faster than n for very low

n, $S_\alpha \to 0$ as $n \to 0$. In contrast to the pressures, the dominant contribution for $S_{\rm tot}$ arises from the nucleons outside of α-particles.

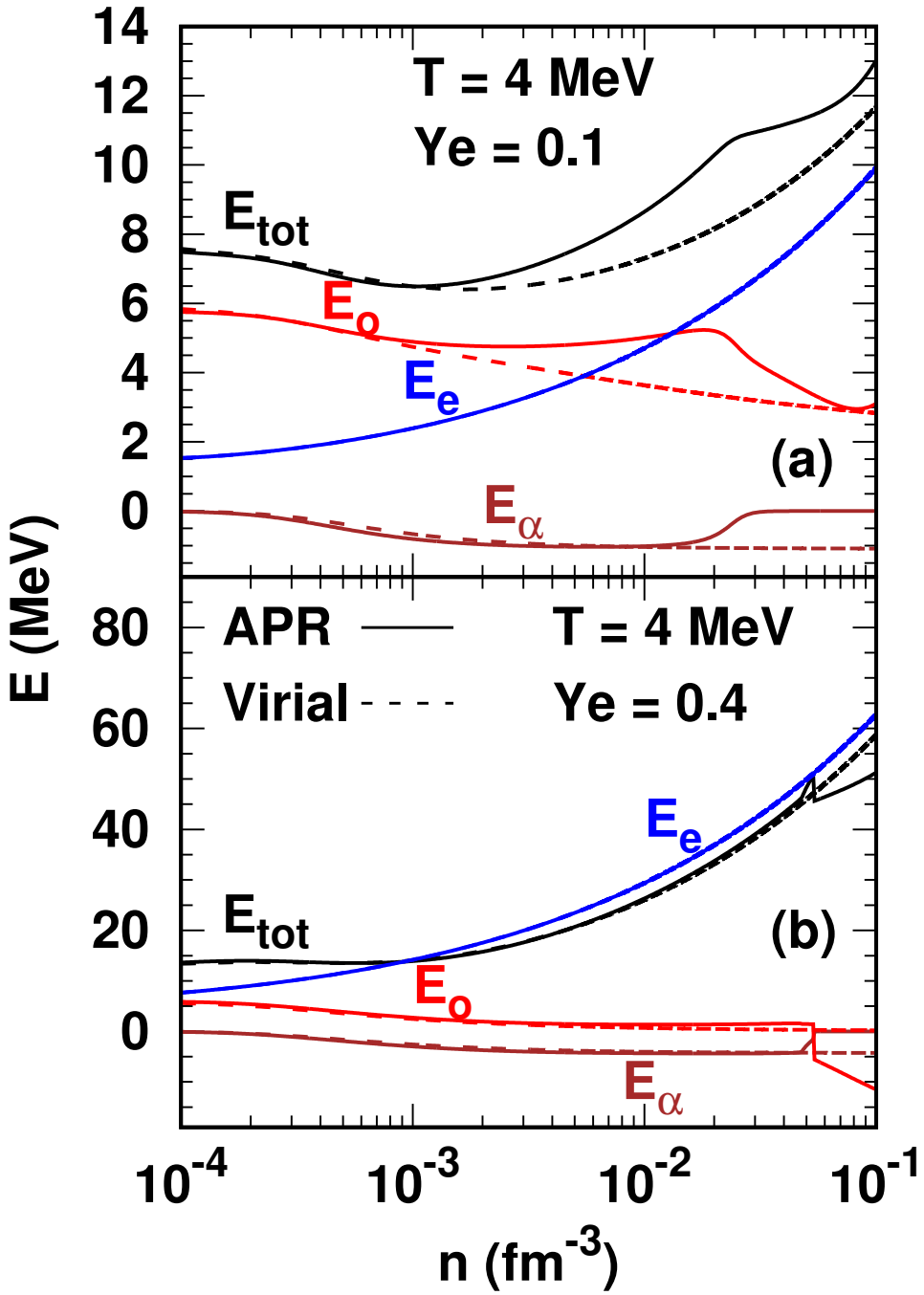

Figure 3.10: Same as fig. 3.8, but for the energy per baryon vs baryon number density.

For the same values of T and Y_e as in fig. 3.8, the energy per baryon, $E = \epsilon/n$, vs n is shown figs. 3.10(a) and (b). For both Y_e's, the α-particle energies per baryon, E_α, in the two approaches are nearly the same at low densities. They differ from each other at the densities for which the excluded volume effects become significant. As n_α continues to increase with n in the virial approach, the magnitude of E_α continues to decrease. Note also that E_α remains negative until $T \gtrsim 2B_\alpha/3$. For Y_e=0.1, the electron energies supersede those of the nucleons at some density whereas they are the dominant contributions at $Y_e = 0.4$ at all n shown. In contrast to the virial approach, the non-monotonic behavior of the nucleon energies, $E_{\rm o}$, at $Y_e = 0.1$, stemming from the excluded volume approach, is also noteworthy.

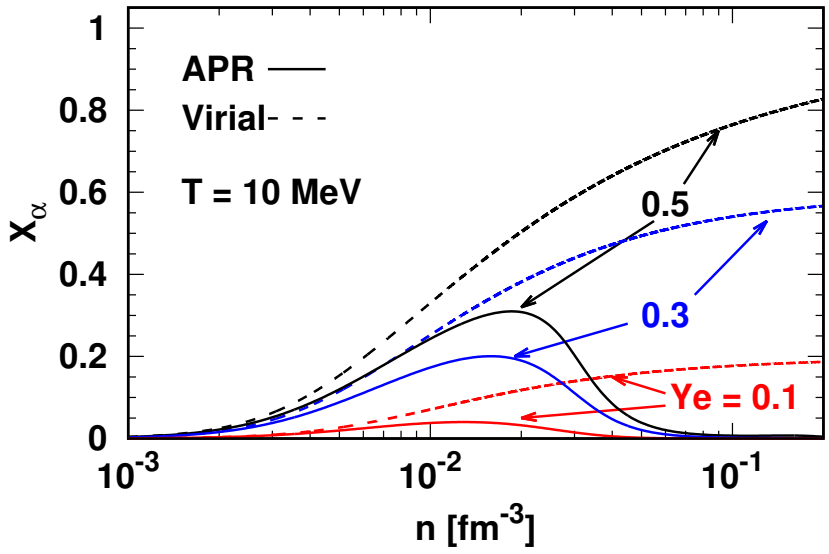

Figure 3.11: Same as fig. 3.7, but for $T = 10$ MeV.

In fig. 3.11, the α-particle fractions are shown at $T = 10$ MeV for representative Y_e's. In contrast to the results at $T = 4$ MeV, the dissolution of the α-particles is less abrupt in

the excluded volume approach. The difference with the results of the virial approach grows as the density increases for all Y_e's. With more positive charge and baryon number added with the inclusion of additional light nuclear clusters and heavy nuclei, these results will also change correspondingly in both the approaches (see discussion in subsequent sections).

Pressures at $T = 10$ MeV are shown in fig. 3.12. Relative to the results in fig. 3.8 at $T = 4$ MeV, the higher thermal content in the pressure of nucleons $P_{\rm o}$ is evident in this figure for both Y_e's. Contributions to $P_{\rm o}$ at $Y_e = 0.4$ for n approaching 0.1 fm^{-3} in the excluded volume approach are negative because the temperature is well below the liquid-gas phase transition temperature of $T_c \simeq 17$ MeV for the EOS of APR at this Y_e [CMPL14]. The virial $P_{\rm o}$'s remain positive, albeit very small at $Y_e = 0.4$. Contributions from leptons are substantial for both Y_e's.

Results for multiple clusters in the Excluded Volume Approach

In this section, we present and discuss results of the excluded volume approach when the low-density phase contains d, ^{3}H, ^{3}He and ^{4}He. For related, but slightly different treatment of the excluded volume approach, *cf.* refs. [Typ16, PT17]. Results in these references are qualitatively similar to those of ours although small quantitative differences exist. Put together, these results enable comparisons with results of the virial approach in refs. [OGH$^+$07, A$^+$08].

The mass fractions from eq. (3.24) are shown in fig. 3.13. In the results shown, the relative fractions of the various species are determined by a combination of the charge and baryon number conservation laws as well as values of the B_i's, T, Y_e, and $P_{\rm o}$. The density at which an individual species vanishes is primarily controlled by the excluded volume v_i assigned to it. Note that there is some leeway in assigning these values instead of the geometrical factors adopted here. In principle, one could also use ranges of effective

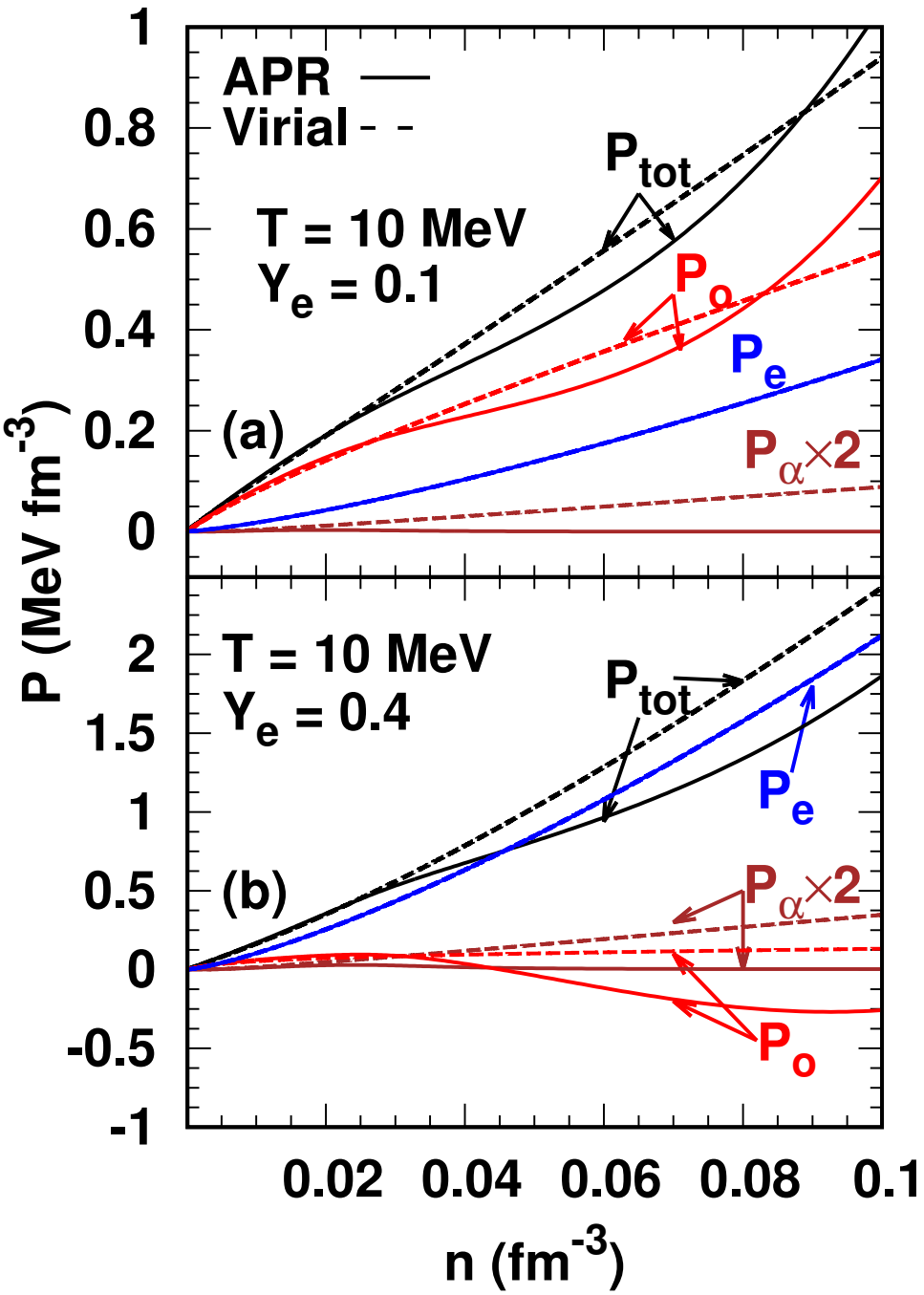

Figure 3.12: Same as fig. 3.8, but for $T = 10$ MeV.

interactions in determining the excluded volume. In addition, the presence of heavy nuclei (to be included later) will also alter the relative concentrations. Our results here are illustrative of the effects of excluded volumes, but the formalism allows for other values to be used. These remarks apply for results of the state variables shown below as well.

Figure 3.14 shows contributions from light nuclei to the total pressure. As the light nuclei are treated as non-interacting gases, their pressures are given by ideal gas expressions, $P_i = n_i T$, modulo the excluded volume factors in eq. (3.30) which act significantly only when each of the nuclear species is disappearing. The temperature being fixed at $T = 4$ MeV for this figure, the partial pressures reflect the variation of the individual densities of nuclei with n. Note that contributions from the electrons begin to dominate as Y_e increases.

The entropies per baryon of light nuclei and their total are displayed in fig. 3.15. Note that the predominance of one or the other light nuclear species varies with increasing density with nucleons giving a substantial contribution for both Y_e's shown. Contributions from ^{3}He, d and e are subdominant for both Y_e's.

For the same temperature and Y_e's as in the previous figures, contributions from light nuclei for the total energy per baryon vs density are shown in fig. 3.16. Because the B.E. of deuterons is small compared to the temperature, their energies are positive until they disappear. Such is not the case for ^{3}H, ^{3}He, and α-particles, hence they remain negative until they disappear. Note also that the nucleon energies turn negative as n approaches 0.1 fm^{-3} for $Y_e = 0.4$. As noted earlier, these results are subject to modifications in the presence of heavy nuclei to be described later.

Limitations of the Excluded Volume and Virial Approaches

The excluded volume approach accounts only for repulsive interactions which become significant as the density increases. As a consequence, light nuclear species

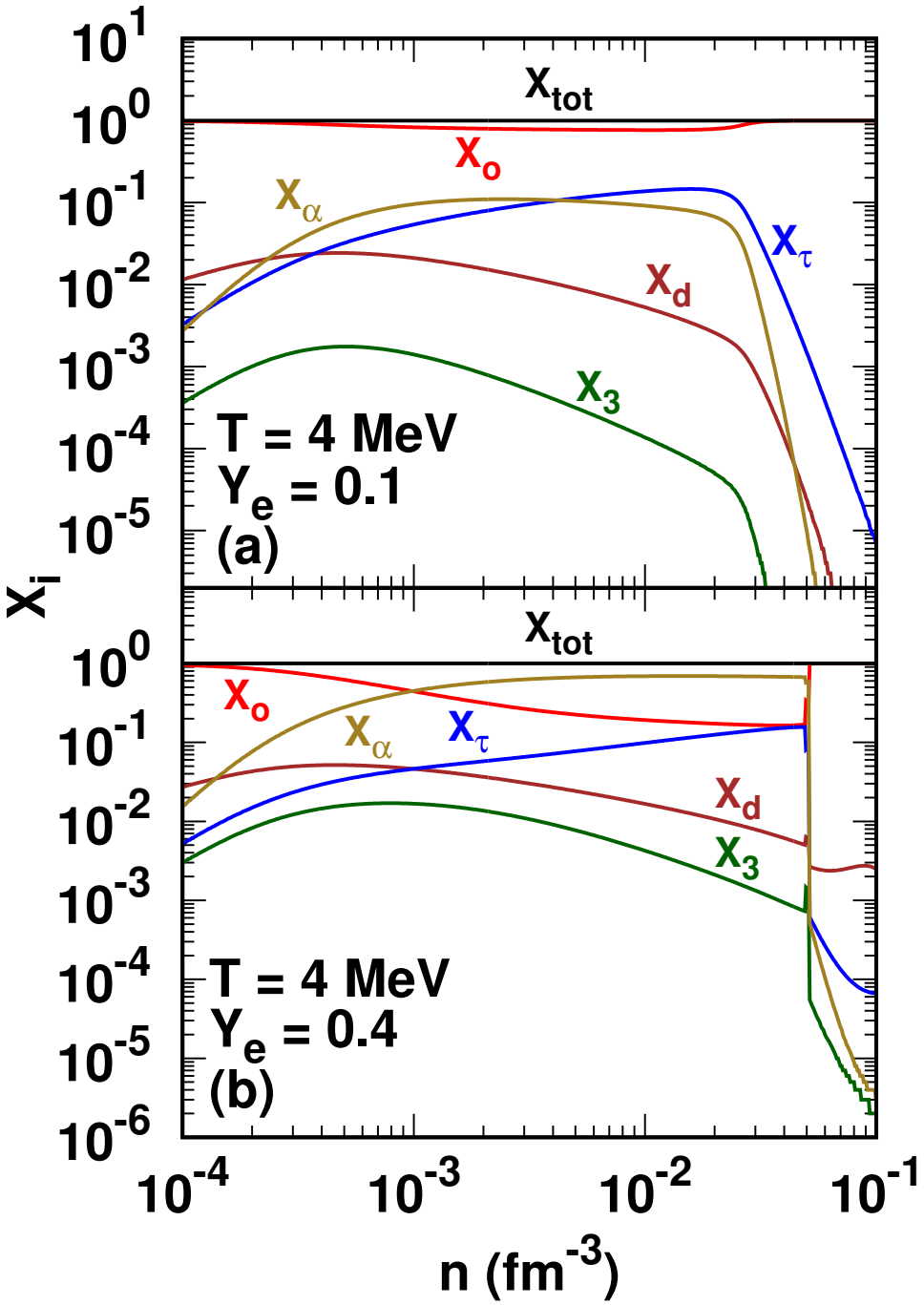

Figure 3.13: Mass fractions of light nuclei vs baryon density at the indicated temperature and electron fractions.

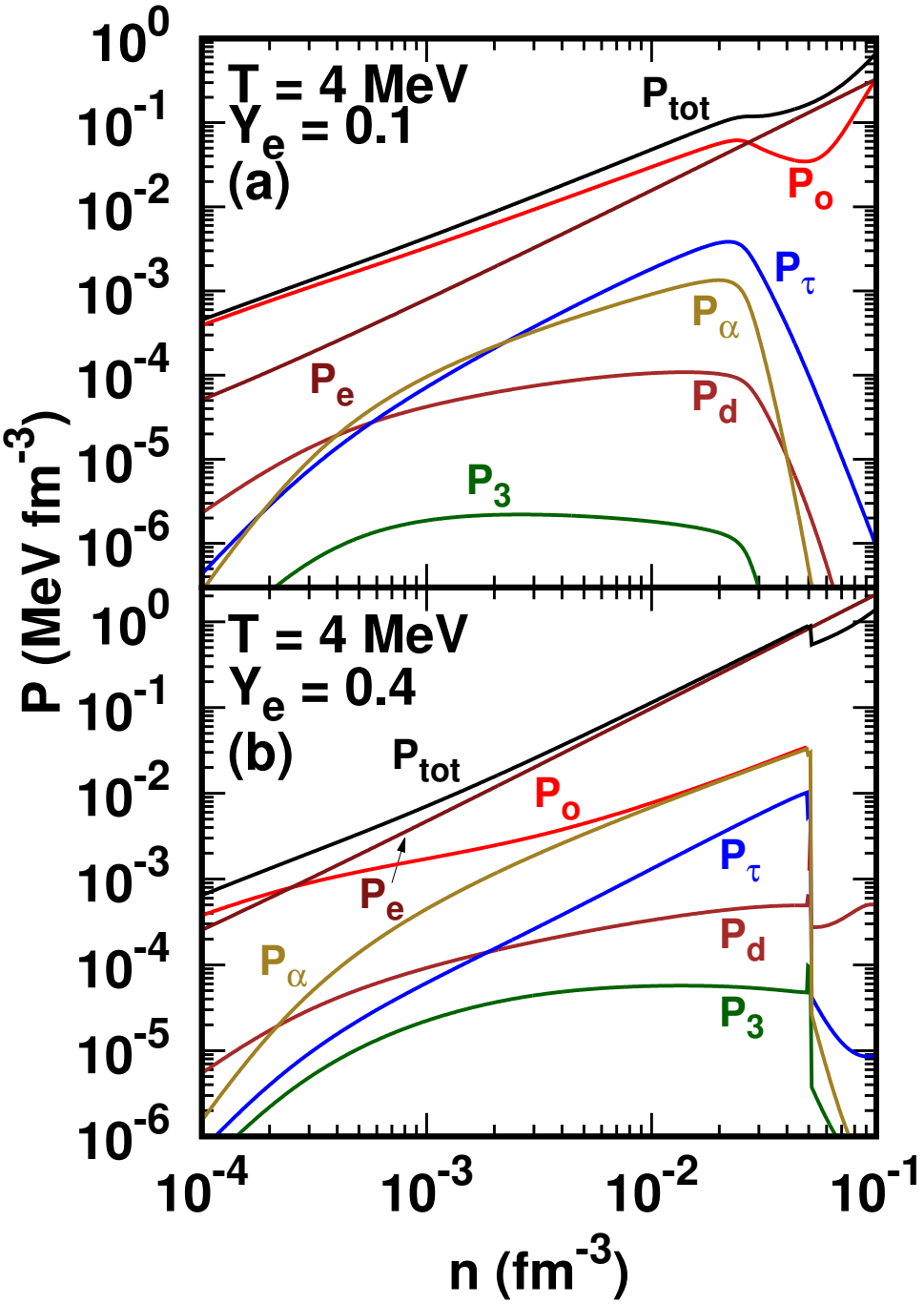

Figure 3.14: Contributions from light nuclei to the total pressure vs baryon density at the indicated temperature and electron fractions.

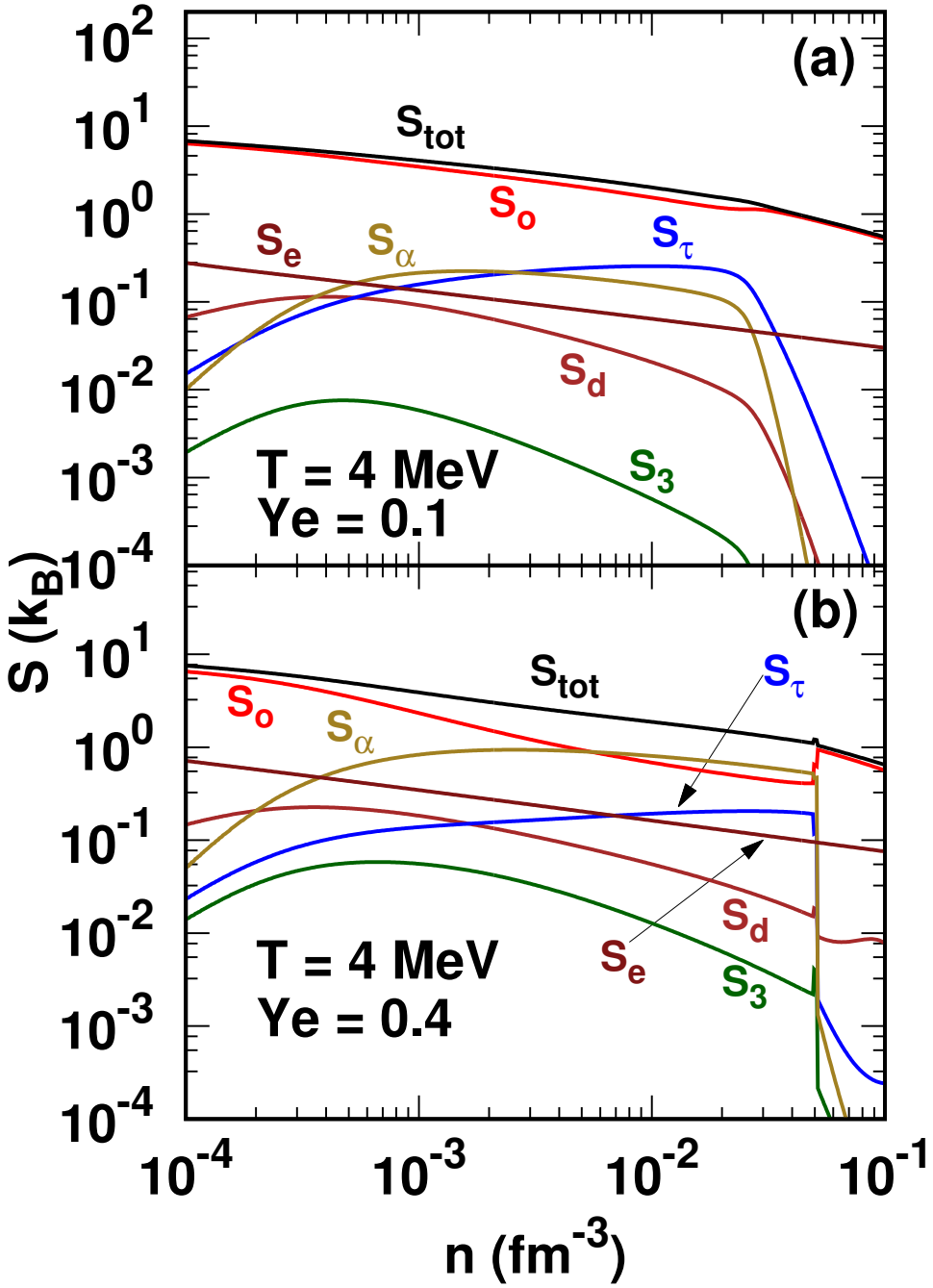

Figure 3.15: Contributions from light nuclei to the total entropy per baryon vs baryon density at the indicated temperature and electron fractions.

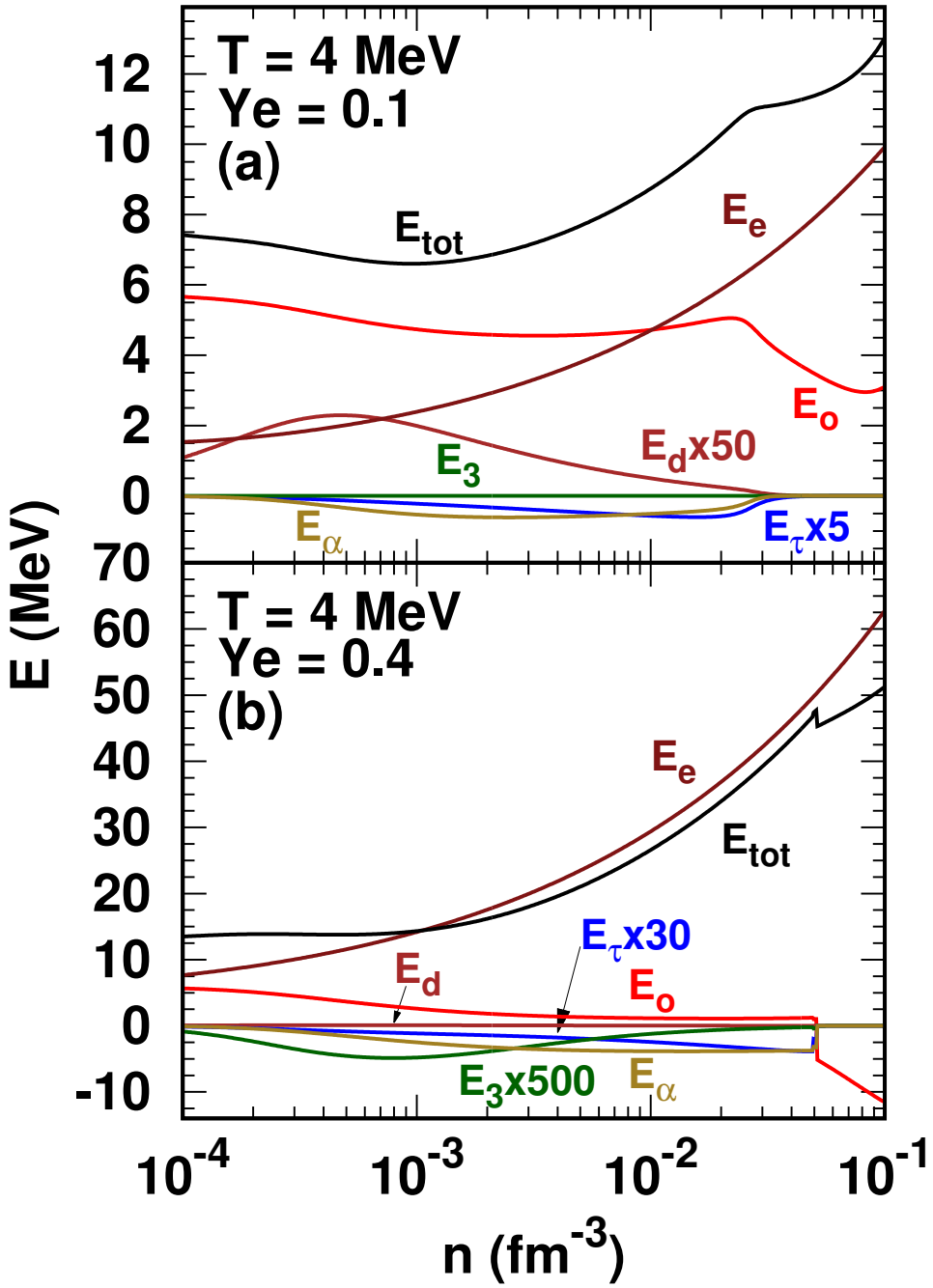

Figure 3.16: Contributions from light nuclei to the total energy per baryon vs baryon density. Note the large multiplicative factors used in some cases for the sake of clarity.

disappear at varying densities below ~ 0.1 fm^{-3}. In the (n, Y_e, T) region where heavy nuclei are favored, the relative abundances of the light nuclei are also greatly affected [LS91, SHT10]. The principal drawback of the excluded volume approach is the lack of attractive interactions known to be present from phase shift data, where available. Nevertheless, as inclusion of such effects provides small corrections to the ideal gas state variables, the results of the excluded volume approach will likely not be affected significantly.

Taking guidance from the available phase shift data, the virial approach, where applicable, includes both attractive and repulsive interactions. In the manner in which interactions are included in this approach, their effects become predominantly attractive. Consequently, the mass fractions of light nuclei continue to increase toward and beyond n_s in the regions of (n, Y_e, T) where heavy nuclei are absent. Although the fugacities of the clusters remain less than unity, such is not the case for nucleons in a wide range of T and Y_e. An illustration of this feature is presented for npe matter in fig. 3.17 where neutron fugacities z_n are shown. With decreasing proton fraction x, the densities at which z_n's exceed unity also decrease. As $z << 1$ is a requirement of the virial approach, caution must be exercised in its use.

From a theoretical standpoint, the region with light nuclear clusters presents the situation of fermion-boson mixtures extensively studied in the context of cold atoms [PS08]. We have developed an approach based on the mean fields experienced by nucleons and the different light nuclei accounting for both attractive and repulsive hard-core interactions. Results from this approach will be presented in a separate publication.

Inhomogeneous Phase with Heavy Nuclei

The inhomogeneous phase consisting of heavy nuclei surrounded by a gas of nucleons, light nuclei, leptons and photons occupies a substantial region (phase II in fig.

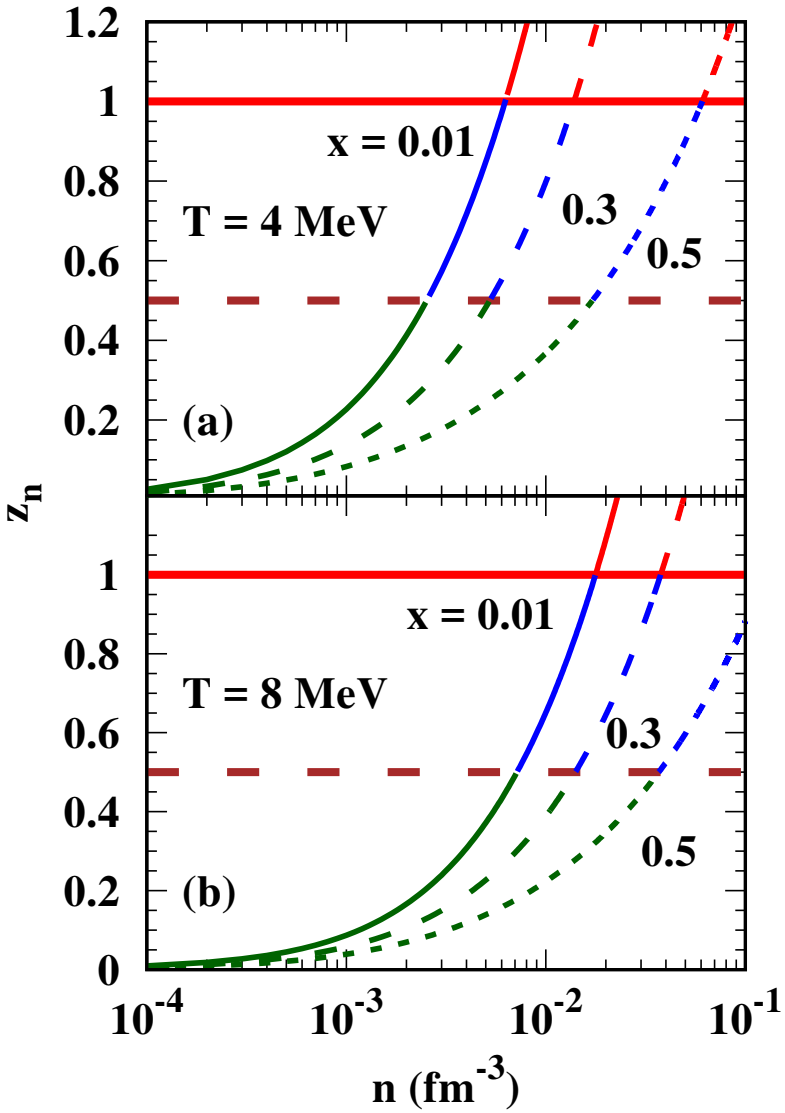

Figure 3.17: Neutron fugacity $z_n = \exp(\mu_n/T)$ vs baryon density in npe matter from the virial approach. Values of the temperature T and proton fraction $x = n_p/n_b$ are as indicated in the figure. The intersections of the various curves with the horizontal lines at $z_n = 1$ indicate the densities beyond which the virial approach loses its validity.

3.5) at sub-nuclear densities $n \lesssim 0.1$ fm^{-3}. For densities in excess of 0.1 fm^{-3}, matter is too dense for nuclei of any type to form and thus consists of uniformly distributed

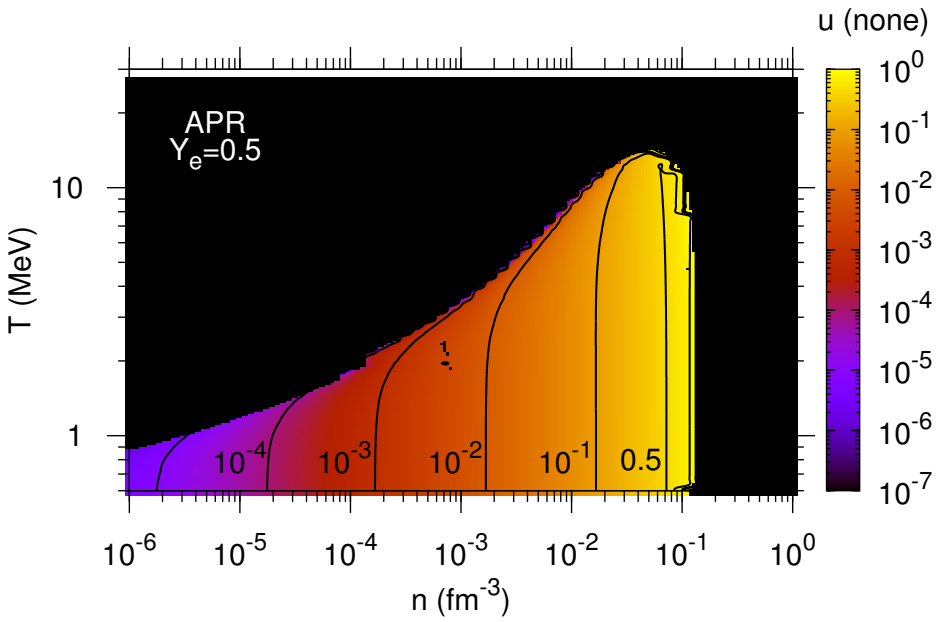

Figure 3.18: Contours of the volume fraction u occupied by nuclei at sub-nuclear densities in the T-n plane for the EOS of APR. The net electron fraction $Y_e = 0.5$. Figure courtesy of Brian Muccioli.

nucleons and leptons (phase III in fig. 3.5). For the treatment of heavy nuclei, two main approaches have been adopted in the literature: the single nucleus approximation [LS91, LLPR85] and the full ensemble method [SHT10]. The former approach gives an adequate representation of the thermodynamics of the system [BL84], while the latter approach is warranted for applications involving neutrino-nucleus and electron-nucleus scattering and absorption processes.

In fig. 3.18, we show results for the volume fraction u occupied by nuclei for $Y_e = 0.5$. The results shown here are for the EOS of APR in the single nucleus approximation of [LS91]. Decreasing the electron fraction from $Y_e = 0.5$ reduces the fraction of space occupied by nuclei for a given density n and temperature T. This

reduction occurs because at low Y_e's, nuclei are unable to maintain a moderate proton fraction ($x_i \simeq 0.3$) and thus fewer nuclei form.

Observe that while the presence of electrons in the whole system ensures charge neutrality and mechanical stability, electrons are entirely irrelevant in the calculation of T_c^A which is the temperature above which nuclei of mass A dissolve into their constituent nucleons. As such, T_c is a property of matter enclosed in nuclei and can only depend on the charge fraction x_i inside nuclei. In turn, x_i is a function of the ambient conditions (n, Y_e, T) in which the nuclei are embedded; here Y_e is the net electron fraction of the whole system. For large enough nuclei, matter in their interior can be reasonably well approximated by infinite matter. In this case, T_c is obtained by solving eq. (9); that is T_c is the liquid-gas phase transition temperature. Note that, in general, $x_i < Y_e$ and therefore $T_c^A < T_c^\infty$. Similar considerations apply to the pasta phase; the temperature T_c^p above which the pasta phase disappears is much less than T_c^A. Detailed results for the state variables corresponding to the EOS of APR will be reported separately [SCMP19]. This work adds to the suite of EOSs based on the Skyrme interaction provided in ref. [SRO17].

The Supra-Nuclear Equation of State

Structural properties, such as the mass, radius, moment of inertia, quadrupolar polarizability (or tidal deformability), etc., of a neutron star depend sensitively on the supra-nuclear EOS [LP16]. While the radius of a normal nucleonic neutron star is primarily determined by the EOS in the region up to $n \sim 2n_s$, the star's maximum mass depends on the EOS close to its central density [LP01]. When additional components such as hyperons, Bose Condensates or quarks are considered (and present in substantial amounts), the EOS beyond $2n_s$ can influence both the radius and the maximum mass. The internal composition controls the long-term cooling of neutron stars detected through optical and X-ray thermal emission [PLPS04a]. For the manner in which the

supra-nuclear EOS influences other observable properties including gravitational wave emission, neutrino emission from type-II supernovae, rotation, magnetic properties, etc., of a neutron star, *cf.* refs. [LP16, LP07] for an overview.

There are several *sweet and sour points* concerning theoretical attempts to calculate the supra-nuclear EOS. On the sweet side, developments in effective field theory have enabled first principle calculations of isospin symmetric and asymmetric matter with systematic corrections to be estimated. On the sour side, continuing beyond $2n_s$ to encompass the central densities of neutron stars is precluded in these methods because of the perturbative expansion parameter Λ/p, where Λ is a cut-off in momentum p, reaching uncomfortable values particularly for PNM for which the Fermi momentum $p_F(\text{PNM}) = 2^{2/3} p_F(\text{SNM})$. For example, $p_F(\text{PNM}) \simeq 336$ (533) MeV/c for $n_s(2n_s)$, whereas typically $\Lambda \simeq 600$ MeV/c. Additionally, the error estimates depend on the method employed to impose the cut-off Λ which also affects the unitarity of operators when a cut-off is used. To access the EOS beyond $2n_s$ for inferring structural properties of a neutron star, the approach taken thus far has been to use piece-wise and causal polytropic EOSs beyond $2n_s$ so that a maximum mass of $\gtrsim 2M_\odot$ can be obtained [HLPS13]. While this approach is adequate and useful for cold neutron stars in a parametric study, the internal composition, finite temperature properties and isospin dependence of the EOS cannot be accessed with polytropic EOSs.

Phenomenological EOSs based on non-relativistic potential model approaches with contact and finite-range interactions have long been used to explore possible consequences in astrophysical applications by varying the high-density behavior of the EOS. The advantage of these models is that calculations are relatively easier than the time-consuming first-principle calculations. However, higher-than-two-body interactions, found necessary to fit constraints offered by laboratory data on nuclei at near-nuclear densities, render these EOSs acausal at some high density due to the lack of Lorentz

invariance in a non-relativistic approach. Often, the density at which causality is violated lies within the central densities of neutron stars. Although a method to impose causality based on thermodynamical arguments has been known for a while for cold stars [NC73, LPMY90], it is only recently that a similar method has been devised at finite temperature [CP17]. A practical way to avoid this problem is to screen repulsive contributions from higher-than-two-body interactions (as they lead to an energy per particle that varies faster than linearly at high density) as in refs. [BD80, PAL88, P$^+$97]. For any such nonrelativistic potential model, causality is preserved for *all* temperatures/entropies if the inequalities $\frac{c_s(T=0)}{c} \leq 1$ and $\frac{4}{9}Q^2 + \frac{2n}{3}\frac{dQ}{dn} \leq 1$ are *both* satisfied. The quantity Q is related to the nucleon effective mass m^* and its density derivative according to $Q = 1 - \frac{3m^*}{2n}\frac{dm^*}{dn}$.That is, a full finite-T calculation of the speed of sound is not necessary in order to check whether or not causality is violated. These remarks are relevant also to all first-principle dense-matter calculations that use a non-relativistic approach.

Relativistic Dirac-Brueckner-Hartree-Fock [MPA87, EOHJ$^+$96] and mean field-theoretical [MS96] models and their extensions are inherently Lorentz invariant and thus preserve causality. While the former approach is based on nucleon-nucleon scattering data, in the latter, nucleon-boson coupling strengths are calibrated in medium at n_s to reproduce empirical properties of nuclear matter and nuclei. As with their non-relativistic counterparts, several adjustments of many-body forces in medium have been required to obtain $2M_\odot$ neutron stars with reasonable radii for $\sim 1.4M_\odot$ stars for which observational constraints are beginning to emerge. These approaches, however, do not suffer from the cut-off issues that non-relativistic effective field-theoretical approaches do.

Establishing or ruling out the presence of non-nucleonic degrees of freedom in neutron-star matter has proved difficult on both observational and theoretical fronts. Observationally, a compelling evidence for the presence of exotica in the form of

hyperons, Bose condensates or quarks is lacking. On the theoretical side, many studies including the presence of exotica in one form or the other have been conducted. Most of these studies have been revised with adhoc adjustments concerning strong interactions at high density in view of the discovery of $2M_\odot$ neutron stars. The consensus since then has been that a large amount of exotica in neutron star interiors is untenable [LP11]. In the case of quarks, the overarching concern is the lack of a non-perturbative treatment of quark matter interactions. This conundrum is likely to remain unless breakthroughs occur on both observational and theoretical fronts.

3.4 Thermal Effects on the Structure of Neutron Stars

As figs. 3.1 and 3.2 imply, the entropy and temperature of the post-merger remnant in the merger of binary neutron stars change with the spatial location as well as with time. Consequently, the enclosed mass and the radius of the remnant also change with time. In reality, such changes are brought about by several physical effects such as thermal effects, neutrino trapping, rotation and magnetic fields etc. all acting at the same time. To gain a qualitative or semi-quantitative understanding of how each of these effects affect the masses and radii at a given time, we can study the role of one physical effect at a time while freezing the others. A full dynamical simulation is, however, required for a complete understanding when all of the physical mechanisms act in concert.

We therefore begin with the role of thermal effects on the structure of a neutron star. As most of the enclosed mass is accumulated from regions above n_s in the star, an analysis based on nearly-degenerate matter offers some insight. Under such conditions, the maximum gravitational mass at finite constant entropy per baryon (throughout the star) can be expressed as [P$^+$97]

$$M_{\rm max}(S) = M_{\rm max}(0)\,[1 + \lambda S^2 + \cdots]\,, \tag{3.31}$$

where the coefficient λ is EOS dependent. Table 3.2 presents physical properties of the maximum mass (gravitational) nucleonic stars for the EOSs chosen in ref. [P$^+$97]. The EOSs labelled BPAL32 and SL32 are non-relativistic potential models, and MRHA and GM are from mean field theoretical models. The values of λ given in table 3.2 are quite small, $\sim 10^{-2}$. We note that the results in this table correspond to the case when only regions above $n \simeq 0.08$ fm^{-3} contained thermal effects, but not the surface regions below that density. We have verified that the increasing trend in the maximum mass at finite S is not affected by this omission, but the radius would be larger when the surface regions are also subject to thermal effects. Results for EOSs including that of APR in which the entire star is heated will be reported in a subsequent publication [SCMP19].

As in the case of nucleonic stars, thermal effects provide positive pressure at a given baryon density in stars containing hyperons, Bose condensates or quarks as well, and therefore the maximum gravitational mass increases slightly at finite entropy relative to that at zero temperature [P$^+$97]. As will be discussed in later sections, other physical effects increase the maximum mass substantially more than thermal effects.

3.5 Effects of trapped Neutrinos on the Structure of Neutron Stars

Elusive as they are, the weakly interacting neutrinos can be trapped in matter, albeit transiently, in several astrophysical circumstances. The physical sites of interest include the early universe, core-collapse supernovae, newly born neutron stars, and mergers of binary neutron stars [PLSV01]. For example, the supernova center mean free path for neutrino scattering is $\lambda \approx 2 \times 10^5$ (MeV/E$_\nu$)^2 cm, where E_ν is the neutrino energy in MeV. Thus, neutrinos with energy 1 MeV or more would be trapped during the evolution of a core-collapse supernova. Furthermore, at early times in a proto-neutron star's evolution, neutrinos would be trapped in matter as well, being unable to propagate on dynamical timescales. Electron capture reactions, which proceeded due to the increasing density and

Table 3.2: Effects of finite entropy on the structure of neutron stars. Results taken from Prakash et al. [P+97]. The various symbols are: S, entropy per baryon, $M_{\rm max}$, the maximum mass, R, the radius of the maximum mass configuration, n_c/n_0, the core density in units of the nuclear equilibrium density, P_c, the core pressure, T_c, the core temperature, λ, percentage change in $M_{\rm max}$, and I, the moment of inertia corresponding to $M_{\rm max}$. Model designations are as in ref. [P+97] (see also text).

Model	S	$\frac{M_{\rm max}}{M_\odot}$	R (km)	$\frac{n_c}{n_0}$	P_c $\left(\frac{\rm MeV}{\rm fm^{-3}}\right)$	T_c (MeV)	$10^2\lambda$
BPAL32	0	1.93	10.1	7.7	590.2	0	
	2	1.97	10.9	6.9	482.8	71.5	0.53
SL32	0	2.1	10.6	6.8	689.9	0	
	2	2.2	11.6	5.8	532.2	103.2	1.11
MRHA	0	1.86	10.6	7.3	484.9	0	
	2	1.9	11.2	6.6	419.6	58.8	0.56
GM	0	2.0	10.9	7.1	545.8	0	
	2	2.04	11.6	6.4	458.2	62.6	0.47

electron chemical potential, effectively halt as the trapped neutrinos settle into a degenerate Fermi sea and contribute their own Fermi pressure to the system. Because neutrinos interact weakly, all of their thermal characteristics are taken as their ideal Fermi gas contributions. The chemical potential of the electron neutrinos, μ_{ν_e} is related to the net electron-neutrino number per baryon Y_{ν_e} by $\mu_{\nu_e}^3 = 6\pi^2 n Y_{\nu_e}$ (the neutrino mass here being negligible compared to μ_{ν_e}). Similar considerations apply to the other flavors of neutrinos as well.

It is interesting to make some observations regarding the effect of trapped neutrinos on the mass of the star itself to which we turn now. Under conditions when neutrinos of lepton flavor $\ell = e, \mu$ and τ are trapped in the system, the beta equilibrium condition becomes

$$\mu_i = b_i \mu_n - q_i(\mu_l - \mu_{\nu_\ell}) \,, \tag{3.32}$$

where μ_i is the chemical potential of baryon i, b_i is its baryon number and q_i is the charge. The chemical potential of the neutron, lepton ℓ and neutrino ν_ℓ are denoted by μ_n, μ_ℓ and μ_{ν_ℓ}, respectively. For example, equilibrium under the electron capture reaction $p + e^- \leftrightarrow n + \nu_e$ establishes the relation

$$\hat{\mu} \equiv \mu_n - \mu_p = \mu_e - \mu_{\nu_e} \,, \tag{3.33}$$

allowing the proton chemical potential to be expressed in terms of three independent chemical potentials as

$$\mu_p = \mu_n - (\mu_e - \mu_{\nu_e}) \,. \tag{3.34}$$

Analogous relations involving other neutrino flavors, hyperons, kaons, quarks, etc. can be found ref. [Pra96].

Because of trapping, the numbers of leptons of each flavor of neutrino

$$Y_{L\ell} = Y_\ell + Y_{\nu_\ell} \tag{3.35}$$

are conserved on dynamical time scales. In the context of core-collapse supernovae, the constraint $Y_{L\mu} = Y_\mu + Y_{\nu_\mu} = 0$ can be imposed because no muons are thought to be present when neutrinos become trapped in the gravitational collapse of the white-dwarf core of massive stars. The electron lepton number $Y_{Le} = Y_e + Y_{\nu_e} \simeq 0.4$, the precise value depending on the efficiency of electron capture reactions during the initial collapse stage. Note, however, that in mergers of binary neutron stars, $Y_{L\mu} \neq 0$, as cold catalyzed neutron stars prior to merger would contain some muons above $\sim n_s$.

Since neutrinos do not carry any charge, the charge neutrality condition remains unaltered from the case in which neutrinos are not trapped.

Table 3.3: Effects of trapped neutrinos on the structure of nucleonic stars. Results taken from Prakash et al. [P+97]. The various symbols are as in table 3.2.

Model	S	$\frac{M_{\max}}{M_\odot}$	R (km)	$\frac{n_c}{n_0}$	P_c $\left(\frac{\text{MeV}}{\text{fm}^{-3}}\right)$	T_c (MeV)	$10^2\lambda$
BPAL32	0	1.86	10.1	7.6	609.6	0	
	2	1.91	10.8	6.7	503.7	63.7	0.63
MRHA	0	1.78	10.3	7.5	514.1	0	
	2	1.84	10.9	6.8	448.3	54.6	0.75
GM	0	1.94	10.5	7.4	595.8	0	
	2	1.98	11.2	6.7	496.6	59.0	0.58

The results presented in table 3.3 for nucleonic stars correspond to the case when $Y_{Le} = 0.4$ and $Y_{L\mu} = 0$, i.e., relevant more for core-collapse supernovae and the initial stages of proto-neutron stars than for the post-merger remnants (in which $Y_{L\mu} \neq 0$) of the coalescence of binary neutron stars. The EOS designations are as in table 3.2. Comparing

results in tables 3.3 and 3.2, one notices a reduction in the maximum mass of $\sim (0.06 - 0.08) M_\odot$ depending on the EOS for both $S = 0$ and 2 when neutrinos are trapped. This reduction is caused by the electron chemical potential μ_e being larger in this instance relative to the case of neutrino-free stars. This increase is required by the conservation of Y_{Le} in eq. (3.35) in the presence of neutrinos. Consequently, nucleonic matter becomes more proton rich to maintain charge neutrality, which in turn causes the EOS to become softer relative to the neutrino-free case.

For the manner in which the maximum mass varies in the case of neutrino-trapped stars containing strangeness-bearing components such as hyperons, kaon condensates or quarks, we refer the reader to ref. [P+97] in which pathways of subsidence of such stars to black holes after deleptonization is described. We note that such pathways would exist only for cases in which a substantial amount of exotica are present (fulfilling, of course, the current constraint of $2M_\odot$ cold catalyzed stars).

As neutrinos diffuse through matter, the lepton numbers will change. The precise manner in which neutrinos diffuse through the star in time is beyond the scope this work; see, however, refs. [BL86, KJ95, PRP+99, PMPL01, PSPL01, RSC+12] for detailed accounts.

3.6 Magnetic Effects on Neutron Star Structure

When magnetic fields have sufficient strength, they influence both the EOS and the structure (through changes in the relevant metric functions) of neutron stars in an intermingled manner. The magnetic field strength needed to dramatically affect neutron structure can be estimated by a dimensional analysis equating the magnetic filed energy $E_B \sim (4\pi R^3/3)(B^2/8\pi)$ with the gravitational binding energy $E_{B.E.} \sim 3GM^2/(5R)$, yielding the so-called virial limit

$$B \sim 1.4 \times 10^{18} \left(\frac{M}{1.4 M_\odot}\right)\left(\frac{R}{10\ \mathrm{km}}\right)^{-2}\ \mathrm{Gauss}\,, \tag{3.36}$$

where M and R are, respectively, the neutron star mass and radius. Magnetic fields quantize the orbital motion (Landau quantization) of charged particles such as electrons, muons and protons in charge neutral and beta-equilibrated matter of neutron stars. The importance of relativistic effects is gauged by the equality of the particle's cyclotron energy $e\hbar B/(mc)$ to its rest mass energy. Although there is nothing critical about this, the magnitudes of the so-called critical fields for the electron, muon and proton are:

$$\begin{aligned} B_c^e &= (\hbar c/e)\, \lambda\!\!\!^{-}_e{}^{-2} = 4.414 \times 10^{13} \text{ Gauss}\,, \\ B_c^\mu &= (m_\mu/m_e)^2 B_c^e = 1.755 \times 10^{18} \text{ Gauss}\,, \\ B_c^p &= (m_p/m_e)^2 B_c^e = 1.487 \times 10^{20} \text{ Gauss}\,, \end{aligned} \tag{3.37}$$

where $\lambda\!\!\!^{-}_e = \hbar/(m_e c) \simeq 386$ fm is the reduced Compton wavelength of the electron. When the Fermi energy of the proton becomes significantly affected by B, the composition and hence the EOS of matter in beta equilibrium becomes significantly affected, and in general leads to a softening of the EOS for $B^* \equiv B/B_c^e \sim 10^5$ [BPL00].

The energy density and pressure from the electromagnetic field are:

$$\epsilon_f = P_f = \frac{B^2}{8\pi} = 4.814 \times 10^{-8}\, B^{*2} \text{ MeV fm}^{-3}\,. \tag{3.38}$$

Thus, to obtain a nominal $\epsilon_f = P_f = 1$ MeV fm^{-3}, a magnetic field strength of $B^* = 4.56 \times 10^3$ or $B \simeq 2 \times 10^{14}$ Gauss is required. These values may be contrasted with the pressure of matter in non-magnetic neutron stars that range from 2-4 MeV fm^{-3} at nuclear density to 400-1000 MeV fm^{-3} at the central densities of maximum mass neutron stars depending on the EOS. Thus, the field contributions dominate the matter pressure only for $B^* > 10^4$ at nuclear densities and for $B^* > 10^5$ at the central densities of neutron stars.

In strong magnetic fields, anomalous magnetic moments κ of the baryons interact with the magnetic field opposing the softening of the EOS due to Landau quantization

[BPL00, BPL02]. For nucleons,

$$\begin{aligned} \kappa_p &= \mu_N \left(\frac{g_p}{2} - 1 \right) \quad \text{for } p\,, \text{ and}\,, \\ \kappa_n &= \mu_N \left(\frac{g_n}{2} - 1 \right) \quad \text{for } n\,, \end{aligned} \tag{3.39}$$

where μ_N is the nuclear magneton, and $g_p = 5.58$ and $g_n = -3.82$ are the Lande g-factors for the proton and neutron, respectively. The energy

$$|\kappa_n + \kappa_p|\, B \simeq 1.67 \times 10^{-5} \text{ MeV} \tag{3.40}$$

measures the changes in the field-free beta equilibrium condition and to the baryon Fermi energies with contributions from the anomalous magnetic moments becoming significant for $B^* > 10^5$. In fact, complete spin polarization of the neutrons occurs when

$$|\kappa_n|\, B \sim \frac{(6\pi^2 n_n)^{2/3}}{4m_n}\,, \tag{3.41}$$

which at nuclear density leads to $B^* \simeq 1.6 \times 10^5$ or $B \simeq 7.1 \times 10^{18}$ Gauss. Such spin polarization results in an overall stiffening of the EOS (due to the increased degeneracy pressure of neutrons) that counters the softening induced by Landau quantization [BPL00]. The net effect is to render the effective EOS very close to that of field-free matter. For a summary of additional effects, for fields close to or exceeding B_c^p, such as vacuum polarization effects [Sch88] and compositeness of baryons, see ref. [LP07].

Studies conducted with assumed frozen-in fields, see, e.g., refs. [BBGN95, BSS00, CPL01] and references therein, offer some insight into the effects of magnetic fields on the structure of neutron stars. Figure 3.19 shows results from ref. [CPL01] (for the EOS of APR) in which the limits of hydrostatic equilibrium for axially-symmetric magnetic fields in general relativistic configurations were analyzed assuming a constant current function. Axially-symmetric magnetic fields provide a centrifugal-like contribution to the total stress-energy tensor, which flattens an otherwise

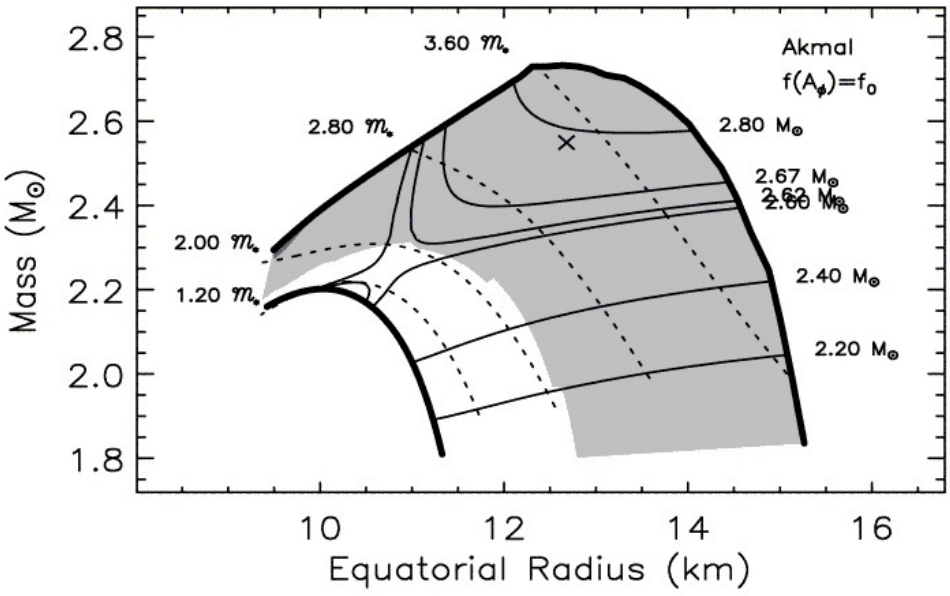

Figure 3.19: Mass-equatorial radius plot showing converged solutions attainable with a constant current function for the EOS of APR [APR98]. The lower heavy curve represents spherical, non magnetized configuration, and the upper heavy curve represents the boundary beyond which solutions appear not to exist. Lighter solid curves are sequences of constant baryon mass (in $M_\odot$), while dotted curves are sequences of constant magnetic moment $\mathcal{M}$ (in units of $\mathcal{M}_* = 10^{35}$ Gaussian). The cross denotes the maximum mass configuration attainable by uniform rotation. Figure from Cardall, Prakash and Lattimer [CPL01].

spherical star. Large enough fields decrease the central (energy) density as the mass is increased eventually compromising the star's stability. As with rotation, magnetic fields allow neutron stars with a particular EOS and baryon number to have larger masses and equatorial radii compared to the field-free case. The maximum mass attainable with a magnetic field governed by a constant current function is noticeably larger than that attained by rotation.

In fig. 3.19, hydrostatically stable configurations (some of which may not be stable to dynamical perturbations) are contained between the heavy solid curves. The lower heavy solid curve is the usual field-free, spherical result for the mass-radius relation. The upper heavy solid curve represents the largest possible stable mass for a given equatorial radius

as the internal magnetic field strength is increased. Large axially-symmetric fields tend to yield flattened configurations, and if large enough, shift the maximum densities off-center resulting in toroidal shapes.

The lighter solid curves in fig. 3.19 represent constant baryon mass sequences of interest as potential evolutionary paths. Note, however, that such paths represent reality only if the current function stays constant over the timescales of magnetic field decay due to Hall drift and ambipolar diffusion. As there is no such guarantee, perhaps the study of several different current functions could shed light on probable evolutionary sequences. The lighter dotted curves in this figure display sequences of constant magnetic moment $\mathcal{M}$. Unlike for baryon number or mass, there is no principle of "conservation of magnetic moment", but over the slow timescales of magnetic field decay, this procedure seems like a plausible opening exploration.

In the context of simulations of merging neutron stars, several additional caveats apply. The post-merger remnant would be differentially rotating till the time rigid rotation takes over due to effects of poorly understood (artificial) viscosity. The generation and evolution of magnetic fields in the rotating remnant itself is a subject beset with considerable uncertainty and is worthy of further studies.

3.7 Rotational Effects on Neutron Star Structure

Rigid rotation increases the maximum mass of a neutron star due to the positive pressure support provided by centrifugal forces. With increasing angular momentum J, mass-shedding at the equator occurs, limiting the maximum angular momentum, $J_{\rm max}$, a star can support. General relativistic instabilities occur slightly before the Keplerian limit, but the latter generally gives a good estimate of rotational instabilities. For uniform rotation, studies in e.g., ref. [CST94] have shown that the increase in the maximum gravitational mass can amount to $\sim 20\%$. In what follows, we summarize the results of

ref. [BSB18] (see also references to earlier works there, and also ref. [FS13]) in which the behavior of maximum baryon and gravitational masses with respect to the Kerr parameter $a = cJ/(GM^2)$ was studied using a wide class of EOSs and a few select laws for differential rotation. In summary, ref. [BSB18] finds

$$\frac{M_B}{M_B^*} = 1 + 0.51\left(\frac{cJ}{GM_B^{*2}}\right)^2 - 0.28\left(\frac{cJ}{GM_B^{*2}}\right)^4 \tag{3.42}$$

$$\frac{M_B}{M_B^*} = 0.93\,\frac{M_G}{M_G^*} + 0.07 \tag{3.43}$$

$$\frac{M_G}{M_G^*} = 1 + 0.29\left(\frac{cJ}{GM_G^{*2}}\right)^2 - 0.10\left(\frac{cJ}{M_G^{*2}}\right)^4 . \tag{3.44}$$

The notation above is $M_G^* := M_{G,max}^{TOV}$, $M_B^* := M_{B,max}^{TOV}$ are maximum gravitational and baryon masses for non-rotating models with $J = 0$, and M_G and M_B are for rotating models with $J \neq 0$.

Self-bound strange quark stars deviate from above trend yielding

$$\frac{M_B}{M_B^*} = 1 + 0.87\left(\frac{cJ}{GM_B^{*2}}\right)^2 - 0.60\left(\frac{cJ}{GM_B^{*2}}\right)^4 . \tag{3.45}$$

The conclusion that emerges from these static studies is that uniform (differential) rotation can increase the maximum allowed mass (before mass shedding) by up to $\sim 20\%$ ($\geq 50\%$). Similar conclusions have been reached in refs. [BR16, WMR18, RMW18], albeit with slightly differing numbers in the case of differentially rotating stars with different rotation laws. As noted in ref. [BSB18], further analysis by extracting realistic rotation laws from dynamical simulations (including magnetic effects) is warranted.

3.8 Conclusions

Simulations of the merger of binary neutron stars require the EOS of dense matter over wider ranges of density and temperature than do those of core-collapse supernovae and protoneutron stars. This requirement stems mainly from the compression and mass of the post-merger remnant achieved in a merger event which are larger than those in the

latter cases. Although advances have been made in dense matter theory, many sore points remain some of which have been pointed out in this work. The gravitational and baryon masses of the post-merger remnants are also influenced by effects of composition, temperature, neutrino trapping, magnetic fields and rotation, the latter differential for short times and rigid thereafter. To gain physical insights, we have provided brief reviews of earlier works studying these effects considering each of them to act separately. In dynamical simulations of mergers, however, all of these effects would be acting simultaneously and evolving with time.

New elements of our work here are (1) a comparison of excluded volume and virial approaches for the npα system using the EOS of APR for interacting nucleons, and, (2) extension of the excluded volume approach to include additional light nuclei such as d, ^{3}H, and ^{3}He at sub-nuclear densities along the lines of refs. [LS91, LLPR85].

The principal difference between the excluded volume and virial approaches for the npα system is that the mass fraction of the α-particle vanishes for $n \lesssim 0.1$ fm^{-3} in the former case (due to excluded volume effects) whereas it continues to rise for the latter up to and beyond nuclear densities. As a result, the excluded volume total pressure exhibits a non-monotonic behavior with density for all electron fractions unlike in the virial approach. For the same reason, similar features are also seen in the total energy per baryon. In both cases, the dominant contribution to the entropy per baryon comes from nucleons outside of α-particles for all electron fractions. The origin of the differences between the two approaches is that the excluded volume approach accounts only for repulsive interactions whereas interactions in the virial approach are predominantly attractive. In addition, the requirement that fugacities be less than unity is not met for nucleonic matter; the density at which the violation occurs decreasing with proton fraction. For densities, temperatures and electron fractions for which heavy nuclei would be present, results from both approaches are similar although quantitative differences exist.

Results from our extension of the excluded volume approach to include light nuclei in addition to the α-particle enable comparisons to be made with related, but slightly different approach of refs. [Typ16, PT17]. We defer such a comparison to a future work. We find that variation of an order in magnitude in the excluded volumes does not result in a big variation of results when multiple clusters are present. What, in fact, determines the relative mass fractions of light nuclei are the respective binding energies and, to a lesser extent, the charge fraction at which the calculation is performed; for example, in neutron rich matter, the concentrations of ^{3}H and ^{3}He will be somewhat enhanced in comparison to the symmetric nuclear matter case. The EOS in this density region would also be relevant to intermediate energy heavy-ion collisions in which abundances of these nuclei are measured. One must note, however, the contributions from electrons, present in astrophysical situations, would be absent in this case. A worthwhile future task would be analyses of fermion-boson mixtures at sub-nuclear densities using effective field theoretical (EFT) techniques.

EFT approaches have enabled first-principle calculations of isospin symmetric and asymmetric nucleonic matter put to $\sim 2n_s$ with systematic error estimates associated with perturbation theory, the treatment of three-body interactions and dependencies on cut-off procedures. For densities beyond $\sim 2n_s$, extrapolations using causal polytropic EOSs have been used to examine the ranges of masses and radii consistent with the requirement of obtaining $2M_\odot$ neutron stars. This latter procedure precludes extension of the EOS to finite temperatures; furthermore, knowledge of the compositional dependence of the EOS required in dynamical simulations is lost. Other approaches, including phenomenological EOSs based on non-relativistic potential models, relativistic Dirac-Brueckner-Hartree-Fock and mean field theoretical models (and its extensions) do not suffer from cut-off issues. However, several adjustments to many-body forces in such treatments have been required since the discovery of $2M_\odot$ neutron stars. Concerning the

possible presence of exotica (hyperons, Bose condensates and quarks) in neutron star interiors, the $2M_{\odot}$ constraint places restrictions in that a significant amount of such matter is disfavored.

Studies of static configurations in which thermal effects, neutrino trapping, assumed magnetic fields and rotation are present on an individual basis have revealed that the maximum gravitational and baryon masses are affected to varying degrees. The maximum increase in these masses occurs for rotation nearing the mass-shedding (Keplerian) limit. For rigid (differential) rotation, the increase in the maximum can amount to 20%($\gtrsim$ 50%). Magnetic fields have a comparable effect only for fields close to or in excess of 10^{18} Gauss. In both of these cases, the star would be deformed. Changes in maximum masses due to thermal effects are comparatively smaller, of order a per cent, which is also the case when neutrinos are trapped. To better understand results of dynamical simulations in which all of these effects would be acting concurrently, study of static configurations in which these effects are combined one after the other with a wider choice of magnetic fields and differential rotation laws than employed so far would be greatly helpful.

3.9 Acknowledgements

Research support from the U.S. DOE grant. No. DE-FG02-93ER-40756 is gratefully acknowledged. We thank David Radice, Jim Lattimer, Andreas Bauswein and Luciano Rezzola for helpful communications. This work benefited from discussions at the 2018 INT-JINA Symposium on “First multi-messenger observation of a neutron star merger and its implications for nuclear physics” supported by the National Science Foundation under Grant No. PHY-1430152 (JINA Center for the Evolution of the Elements) as also from discussions at the 2018 N3AS collaboration meeting of the “Research Hub for Fundamental Symmetries, Neutrinos, and Applications to Nuclear Astrophysics”

supported by the National Science Foundation, Grant PHY-1630782, and the Heising-Simons Foundation, Grant 2017-228.

3.10 Specific Contributions of the Author

The work documented in this chapter is largely derived from the paper "Dense matter equation of state for neutron star mergers" which has been the effort of a team including myself (Sudhanva Lalit), Md. Abdullah Al Mamun and Drs. Constantinos Constantinou and Madappa Prakash. The project of constructing "Dense matter equation of state for neutron star mergers" using using multiple species was conceived by my advisor Dr. Madappa Prakash. The completion of this project involved significant new developments in both theoretical formalisms and numerical techniques. I am the leading author in the peer-reviewed journal publication of the work presented in this chapter. All analytic equations used in this chapter were independently derived by me and crosschecked with those derived by other members of the team. The FORTRAN codes written to produce the results presented in this chapter were written solely by me. Figures (3.13-3.16) presented in this chapter were conceptualized by the team but produced by me alone. The writing of this paper was a team effort with the work being divided such that each member wrote the first draft of a given section, then passed it to another member to be augmented and improved. The process of passing the work between the team members was iterated until all members agreed on the final version. For the first drafts, my focus was on the sections containing results and conclusions, but I was actively involved in developing each section during the iteration process.

4 Treating Quarks within Neutron Stars

The content of this chapter is largely drawn from the preprint "Treating quarks within neutron stars" [HML+19], which will be reproduced verbatim here. My specific contributions to this work are detailed at the end of this chapter.

Treating quarks within neutron stars

Sophia Han,[1,2] M. A. A. Mamun,[1] S. Lalit,[1] C. Constantinou,[3] and M. Prakash[1]

[1] *Department of Physics and Astronomy, Ohio University, Athens, Ohio 45701, USA*

[2] *Department of Physics, University of California Berkeley, Berkeley, CA 94720, USA*

[3] *Department of Physics, Kent State University, Kent, OH 44242, USA*

Abstract

Neutron star interiors provide the opportunity to probe properties of cold dense matter in the QCD phase diagram. Utilizing models of dense matter in accord with nuclear systematics at nuclear densities, we investigate the compatibility of deconfined quark cores with current observational constraints on the maximum-mass and tidal deformability of neutron stars. We explore various methods of implementing the hadron-to-quark phase transition, specifically, first-order transitions with sharp (Maxwell construction) and soft (Gibbs construction) interfaces, and smooth crossover transitions. We find that within the models we apply, hadronic matter has to be stiff for a first-order phase transition and soft for a crossover transition. In both scenarios, quarks most likely appear at the center of canonical neutron stars in the mass range $\approx 1.0 - 1.6\,\mathrm{M}_\odot$ with a sound velocity $c^2_{\mathrm{QM}} \gtrsim 0.4$ characteristic of strong repulsive interactions required to support recently discovered neutron stars with masses $\geq 2\,\mathrm{M}_\odot$. We also identify equations of state and

phase transition scenarios that are consistent with the bounds placed on tidal deformations of neutron stars in the recent binary merger event GW170817. We emphasize that distinguishing hybrid stars with quark cores from normal hadronic stars is very difficult from the knowledge of masses and radii alone, unless drastic sharp transitions induce distinctive disconnected hybrid branches in the mass-radius relation.

4.1 Introduction

The observation that the dense matter inside neutron stars might consist of weakly interacting quark matter owing to the asymptotic freedom of Quantum Chromodynamics (QCD) was first made by Collins and Perry [CP75]. Since then, numerous explorative studies have been conducted to isolate neutron star observables that can establish the presence of quarks deconfined from hadrons. Starting from the QCD Lagrangian, lattice gauge simulations at finite temperature T and net baryon number $n_{\rm B} = 0$ naturally realize hadronic and quark degrees of freedom in a smooth crossover transition. However, lattice simulations for finite $n_{\rm B}$ at $T = 0$, of relevance to neutron stars, have been thwarted due to the unsolved fermion sign problem and untenable imaginary probabilities. As a result, the possible phases of dense matter at $T = 0$ have been generally explored by constructing equation of state (EOS) models of hadrons and quarks that are independent of each other although few exceptions do exist.

Extensive studies of nucleonic matter in neutron stars for $n_{\rm B} \lesssim 0.5\, n_0$, where $n_0 \simeq 0.16$ fm^{-3} is the isospin symmetric nuclear matter equilibrium density, have predicted the presence of a solid crust. Observations of the surface temperatures of accreting neutron stars in their quiescent periods have indeed confirmed the presence of a crust (see ref. [MDK$^+$18], and references therein). This region is characterized by a Coulomb lattice of neutron-rich nuclei surrounded by dripped neutrons with admixtures of light nuclei and

a uniform background of electrons in chemical potential and pressure equilibrium in a charge neutral state. Differences among different equations of state [BPS71, NV73, DH01] are small and are of minor importance to the structure of stars more massive than 1 $M_\odot$. In this work, we use the EOSs of ref. [NV73] (for $0.001 < n_B < 0.08$ fm^{-3}) and ref. [BPS71] (for $n_B < 0.001$ fm^{-3}) to determine the structural properties of the star.

Models of the hadronic EOS for $n_B > 0.08$ fm^{-3} can be grouped into three broad categories: non-relativistic potential models, Dirac-Brueckner-Hartree-Fock models, and relativistic field-theoretical models. Microscopic many-body calculations in the first two of these categories employ free-space two-nucleon interactions supplemented by three-nucleon interactions required to describe the properties of light nuclei as input. In contrast, coupling strengths of the two- and higher-body nucleon interactions mediated by meson exchanges are calibrated at n_0 in the relativistic field-theoretical models. Several schematic potential models based on zero- and finite-range forces also exist that take recourse in the Hohenberg-Kohn-Sham theorem [HK64, KS65] which assures that the ground state energy of a many-body system can be expressed in terms of the local densities alone. Refinements in all of these approaches are guided by the laboratory data on the bulk properties of isospin symmetric and asymmetric matter such as the binding energy BE $= -16 \pm 1$ MeV at $n_0 = 0.16 \pm 0.01$ fm^{-3}, compression modulus $K_{nm} = 240 \pm 20$ MeV, nucleon's Landau effective mass $m^*/m = 0.7 \pm 0.1$, symmetry energy $S_2 = 28 - 35$ MeV, and the symmetry energy slope parameter $L = 60 \pm 20$ MeV, etc.

The lack of Lorentz invariance in non-relativistic models leads to an acausal behavior at some high density particularly if contributions from three- and higher-body interactions to the energy are not screened in medium [BD80, PAL88]. The general practice has been to enforce causality from thermodynamic considerations [NC73, LPMY90]. In some cases, the reliability of the non-relativistic models is severely restricted, some times only

up to $2\,n_0$ as in the case of the chiral effective field-theoretical (EFT) models owing to the perturbative scheme and the momentum cut-off procedure employed there [HLPS10, TKHS13].

To explore consequences of the many predictions of these models at supra-nuclear densities, piecewise polytropic EOSs that are causal have also been extensively used to map out the range of pressure vs. density relations (EOSs) that are consistent with neutron star phenomenology [LP16, SLB16, TKHS13, ZL18]. The viability of these EOSs at supra-nuclear densities necessarily depends on the growing neutron star data to be detailed below.

The possibility of non-nucleonic degrees of freedom such as strangeness-bearing hyperons, pion and kaon condensates, and deconfined quarks above n_0 has also been examined in many of these models [LP16]. At some $n_{\rm B} \gtrsim (2-4)\,n_0$, the presence of quark degrees of freedom has been invoked on the physical basis that the constituents of the hadrons could be liberated as the compression in density progressively increases. First-principle calculations [BC76a, BC76b, FM78, FJ84, KRV10, KV16, GKR$^+$18, ASRS08] of the EOS of quark matter have thus far been limited to the perturbative region of QCD valid at asymptotically high baryon densities. The Nambu–Jona-Lasinio (NJL) model [NJL61], which shares many symmetries with QCD - but not confinement - has been used to mimic chiral restoration in quark matter [Kun89, BO99, Bub05]. Also in common use are variations [KF15, GCS19] of the MIT bag model [BC76a].

Lacking knowledge about the nature of the phase transition, it has been common to posit a first-order phase transition. Even in this case, the magnitude of the hadron-quark interface tension is uncertain [ARRW01, MFPSB10, LGAA13, FHS19]. If the interface tension is regarded as being infinite, a Maxwell construction can be employed to determine the range of density for which chemical potential and pressure equality between

the hadronic and quark phases exists [Gle92]. The other extreme case corresponds to a vanishing interface tension when a Gibbs construction is considered more appropriate. The Gibbs construction also corresponds to global charge neutrality instead of local charge neutrality, appropriate for matter with two conserved charges (baryon number and charge) [Gle01].

Depending on the models used to calculate the EOSs of the hadron and quark phases, chemical potential and pressure equilibrium between the two phases may not be realized [BHK$^+$18]. In such cases, several interpolatory procedures have been used to connect the two phases on the premise that at $n_{\mathrm{B}} >> n_0$, a purely hadronic phase is physically unjustifiable [MHT13, FK16, KPSB15, BHK$^+$18]. As a result, the hadron-quark transition becomes one of a smooth crossover the proportion of each phase depending on the specific interpolation procedure used. This is in contrast to the Gibbs construction (which also renders the transition into a mixed phase to be smooth) in which the fraction of each phase is determined self-consistently.

Although differing in details, other examples of a smooth crossover transition are the chiral model of ref. [DNS15] and the quarkyonic model of ref. [MR19]. A quark phase with additional hadronic admixtures such as hyperons and Bose condensates has also been explored [P$^+$97]. The precise manner in which the hadron-quark transition is treated influences the magnitudes of the mass and radius of the star. In addition, the behavior of the speed of sound with density affects the magnitude of tidal deformations. It is worth mentioning, however, that stars with purely hadronic matter (HM) can sometimes masquerade as stars with quark matter (QM) [ABPR05].

The objectives of this work are to seek answers to probing questions such as (a) What is the minimum neutron star (NS) mass consistent with the observational lower limit of the maximum mass (M_{max}) that is likely to contain quarks? (b) What is the minimum physically reasonable density at which a hadron-quark transition of any sort can occur?

(c) Which astronomical observations have the best potential to attest to the presence of quarks?

Toward providing answers to the above questions, we have undertaken a detailed study of the hadron-to-quark matter transition in neutron stars. Our focus is to study the sensitivity of outcomes on neutron star structure, principally mass-radius relations, in the different treatments of the phase transition. Results so obtained are then subjected to the constraints provided by precise measurements of heavy neutron stars [C$^+$19, AFW$^+$13, DPR$^+$10], bounds on the tidal deformability of neutron stars in the binary merger event GW170817 [A$^+$17c, A$^+$18, DFL$^+$18, A$^+$19] and radius estimates of $1.4\,M_\odot$ available from x-ray observations of neutron stars [SLB16, LP16, ÖPA$^+$16].

Earlier studies in this regard have generally chosen one favored EOS in the hadronic sector and one approach to the quark matter EOS [SPL00, HSM$^+$01, BMG10, KF15, GCS19, WITJ18]. Contrasts between the Maxwell and Gibbs constructions have also been made in some of these works, but with the result that the $R_{1.4}$ are typically larger than 14 km or more (characteristic of the use of mean-field theoretical (MFT) models) which is at odds with most of the available estimates. This work differs in that variations in the EOSs of both the hadronic and quark sectors are considered as well as a global view of the outcomes of different treatments of the transition is taken. By including terms involving scalar-vector and scalar-isovector interactions in MFT models, we show that values of $R_{1.4}$ more in consonance with data can be achieved. Additionally, we present an extension of the quarkyonic matter model of ref. [MR19] to isospin asymmetric matter with the inclusion of interactions between quarks (not considered there) to enable calculations of beta-stable neutron stars. This extension will be useful in applications involving compositional and thermal gradients in quarkyonic stars (such as their long-term cooling as well as quiescent cooling following accretion on them from a companion star and in investigating f-, p- and g- mode

oscillations). Our in-depth study of the thermodynamics of quarkyonic matter sheds additional physical insight into the role the nucleon shell plays in stiffening the EOS.

Our findings in this work reveal that several aspects of neutron star properties deduced from observations may have to be brought to bear in finding answers to the questions posed above. These properties include the masses M, radii R, periods P and their time derivatives $\dot{P}$ and $\ddot{P}$, surface temperatures T_s of isolated neutron stars and of those that undergo periodic accretion from companions, tidal deformations Λ from the detection of gravitational waves from the inspiraling phase of neutron star mergers, etc. Currently, the accurately measured neutron star masses around and above $2\,\mathrm{M}_\odot$ [C$^+$19, AFW$^+$13, DPR$^+$10] pose stringent restrictions on the EOS. Even so, the EOS would be better restricted with knowledge of radii of stars for which the masses are also known, although this would not reveal the constituents of dense matter as the structure equations depend only on the pressure vs. density relation and not on how it was obtained. In contrast, the surface temperatures of both isolated neutron stars and of quiescent cooling of accreting neutron stars are sensitive to the composition, but simultaneous knowledge of their masses and radii are yet unknown. The anomalous behavior of the braking indices $n = \Omega\ddot{\Omega}/\dot{\Omega}^2$, where $\Omega = 2\pi/P$ is the spin rate, of several known pulsars [MMF12, HSUU15, JK17] can also be put to good use in this connection.

The organization of this paper is as follows. In Sec. 4.2, we present the models in the hadronic and quark sectors chosen for our study. The rationale for our choice and basic features of these models are highlighted here for orientation. We stress that our choices are representative, but not exhaustive. Results of neutron star properties for different treatments of the hadron-quark transition introduced in Sec. 4.3 are shown and discussed in Sec. 4.4. Our conclusions and outlook are contained in Sec. 4.5. Appendix 4.5 contains details about the thermodynamics of nucleons in the shell of quarkyonic matter.

We use units in which $\hbar = c = 1$.

4.2 Equation of State Models

Nucleonic EOSs

To explore sensitivity to the hadronic part of the EOS, we use representative examples from both potential and relativistic mean field-theoretical (RMFT) models. In the former category, the EOS of Akmal, Pandharipande and Ravehall [APR98], which is a parametrization of the more microscopic variational calculations of Akmal and Pandharipande [AP97], is chosen as its energy vs. baryon density up to $2\,n_0$ closely matches those of modern EFT calculations of pure neutron matter and symmetric nuclear matter [HLPS10, TKHS13]. Explicit expressions for the energy density ε, pressure P, compression modulus K_0, Landau effective mass m^*/m, symmetry energy S_2, and the symmetry energy slope parameter L along with the coupling strengths of the various terms therein can be found in ref. [CMPL14].

To provide contrast, we have constructed three EOSs, MS-A, MS-B and MS-C using the RMFT model of Müller and Serot [MS96] employing terms that contain scalar-isovector and vector-isovector mixings as in refs. [HP01b, HP01a]. Explicitly, the Lagrangian density for this model is

$$\begin{aligned}
\mathcal{L} &= \overline{\Psi}[i\partial\!\!\!/ - g_\omega \omega\!\!\!/ - \frac{1}{2} g_\rho \rho\!\!\!/ .\tau - M + g_\sigma \sigma - \frac{1}{2} e(1+\tau_3) A\!\!\!/]\Psi \\
&+ \frac{1}{2}(\partial_\mu \sigma)^2 - V(\sigma) - \frac{1}{4} f_{\mu\nu} f^{\mu\nu} + \frac{1}{2} m_\omega^2 \omega^\mu \omega_\mu \\
&- \frac{1}{4} B_{\mu\nu} B^{\mu\nu} + \frac{1}{2} m_\rho^2 \rho^\mu \rho_\mu - \frac{1}{4} F_{\mu\nu} F^{\mu\nu} \\
&+ \frac{\zeta}{24} g_\omega^4 (\omega^\mu \omega_\mu)^2 + \frac{\xi}{24} g_\rho^4 (\rho^\mu \rho_\mu)^2 + g_\rho^2 f(\sigma, \omega_\mu \omega^\mu) \rho^\mu . \rho_\mu
\end{aligned} \tag{4.1}$$

with

$$\begin{aligned}
V(\sigma) &= \frac{1}{2} m_\sigma^2 \sigma^2 + \frac{\kappa}{6} (g_\sigma \sigma)^3 + \frac{\lambda}{24} (g_\sigma \sigma)^4 \\
f(\sigma, \omega) &= \Lambda_\sigma g_\sigma^2 \sigma^2 + \Lambda_\omega g_\omega^2 \omega^2 \,.
\end{aligned} \tag{4.2}$$

Expressions for the energy particle $\varepsilon/n, P, K_0$, the the Dirac effective mass M^* and hence the sigma field $\sigma_0 = (M - M^*)/g_\sigma$ in the mean field approximation can be found in ref. [SPLE05]. With input values of these quantities at n_0, the coupling strengths g_σ, g_ω, κ and λ are straightforwardly determined by numerically solving the system of nonlinear equations containing these quantities. The strengths ζ and ξ, Λ_σ and Λ_ω of the quartic ω and ρ fields, remain as adjustable input parameters to control the high density behavior. The density dependent symmetry energy in this model is [HP01a]

$$\begin{aligned} S_2 &= S_{2k} + S_{2d} \\ &= \frac{k_F^2}{6E_F^*} + \frac{1}{8}\frac{g_\rho^2\, n}{m_\rho^{*2}}\,, \quad E_F^* = \sqrt{k_F^2 + M^{*2}} \\ m_\rho^{*2} &= 2g_\rho^2\left(\Lambda_\sigma g_\sigma^2 \sigma_0^2 + \Lambda_\omega g_\omega^2 \omega_0^2\right). \end{aligned} \tag{4.3}$$

The first term on the right hand side above contains effects of interaction through σ-meson exchange, whereas the second term includes those from the ρ-meson exchange along with ρ-σ and ρ-ω mixing. The corresponding slope parameter at n_0 becomes

$$\begin{aligned} L &= 3\,n_0 \left.\frac{dS_2}{dn}\right|_{n_0} = L_k|_{n_0} + L_d|_{n_0} \\ L_k &= 2S_{2k}\left[1 - 18\left(\frac{S_{2k}}{k_F}\right)^2\left\{1 + 3\left(\frac{M^*}{k_F}\right)^2 \frac{d\ln M^*}{d\ln n}\right\}\right] \\ L_d &= 3S_{2d}\left[1 - 32S_{2d}\left\{\Lambda_\sigma g_\sigma^2 \sigma_0 \frac{d\sigma_0}{dn} + \Lambda_\omega g_\omega^2 \omega_0 \frac{d\omega_0}{dn}\right\}\right]. \end{aligned} \tag{4.4}$$

Analogous expressions, but without the term involving Λ_σ, can be found in ref. [CP14]. The strength g_ρ may be fixed with a prescribed value of S_2 at n_0, which leaves one or a combination of Λ_σ and Λ_ω to obtain a desired value of L. The values of the various couplings used in this work are listed in Table 4.1.

As noted in refs. [HP01a, SPLE05], the quartic and scalar-isovector and vector-isovector terms in eq. (4.1) enable acceptable values [LL13] of the symmetry

Table 4.1: RMFT coupling strengths. Values of the meson masses used are $m_\sigma = 660$ MeV, $m_\omega = 783$ MeV and $m_\rho = 770$ MeV.

Model	g_σ	g_ω	g_ρ	κ	λ
MS-A	12.819	12.258	12.079	0.02544	-0.02179
MS-B	11.369	10.143	9.446	0.05098	-0.03396
MS-C	10.026	7.961	8.492	0.10841	-0.00365
Model	ζ	ξ	Λ_σ	Λ_ω	
MS-A	0.0001	1.0	0.001	0.05	
MS-B	0.0001	1.0	0.001	0.05	
MS-C	0.0001	1.0	0.001	0.05	

energy slope parameter, L, at n_0, to be obtained. The reduction in L from its generally large value found in the literature for RMFT models is made possible by the second term in L_d of eq. (4.4), the term in braces being positive definite. These density dependent terms also influence the high density behavior of these EOSs leaving the near nuclear density behavior intact. Salient properties at the nuclear equilibrium density n_0 for these nucleonic models are presented in Table 4.2. The values of L in Table 4.2 are to be compared with those of the APR and so-called FSU models [CP14, FPH18] in the literature; see e.g. fig. 2 and Table IV in ref. [CP14]: $L = 60.5$ MeV for FSU (but it does not achieve $2\,\mathrm{M}_\odot$) and $L = 112.8 \pm 16.1$ MeV for FSU2 with $M_{\max} = 2.07 \pm 0.02\,\mathrm{M}_\odot$, $R_{\max} = 12.2$ km and $R_{1.4} = 14.42 \pm 0.26$ km. In comparison to FSU2, the values of L for the MS models of this work are significantly smaller, which results in smaller radii for the maximum mass and $1.4\,\mathrm{M}_\odot$ neutron stars (see Table 4.3 below).

Table 4.2: Properties at the nuclear equilibrium density n_0 for EOSs used in this work compared to that of the APR EOS [CMPL14]. Entries in this table are the Landau effective mass m^*/M, isospin symmetric matter compression modulus K_0, kinetic and interaction parts S_{2k} and S_{2d} of the total symmetry energy S_2, and the corresponding parts of the symmetry energy slope parameter L. In MS models, $m^* = E_F^* = \sqrt{k_F^2 + M^{*2}}$.

Property	APR	MS-A	MS-B	MS-C	Units
n_0	0.16	0.16	0.16	0.16	fm^{-3}
m^*/M	0.698	0.662	0.763	0.847	
K_0	266	230	230	230	MeV
S_{2k}	9.79	18.55	16.09	14.49	MeV
S_{2d}	22.80	11.45	13.91	15.51	MeV
S_2	32.58	30.0	30.0	30.0	MeV
L_k	12.69	61.74	44.35	34.52	MeV
L_d	45.78	-13.40	8.65	30.88	MeV
L	58.47	48.34	53.00	65.40	MeV

Properties of nucleonic neutron stars

Structural properties of charge neutral and beta-equilibrated neutron stars resulting from the chosen EOSs are listed in Table 4.3. Two of the three MS EOSs satisfy the requirement of supporting a star with $M_{\mathrm{max}} \geq 2\,\mathrm{M}_\odot$. The EOS of MS-C does not obey the $2\,\mathrm{M}_\odot$ constraint, but we have retained it in our analysis because, in conjunction with crossover transitions involving quark matter, masses well in excess of this observational limit can be obtained (see Secs. 4.3 and 4.4). Although the RMFT models employ terms that contain scalar-isovector and vector-isovector mixings as in refs. [HP01b, HP01a] to yield acceptable values of the symmetry energy slope parameter L at n_0, the radii of neutron stars stemming from these models are somewhat larger than that of the APR

model, but lie within the range of those extracted from data [LL13]. The largest differences between the APR and RMFT models are in the central pressures of the maximum mass stars. The proton fractions, $y_{c,1.4}$ and $y_{c,\max}$, are such that only stars close to the maximum mass stars allow the direct Urca processes with electrons and muons to occur [LPPH91a].

Table 4.3: Structural properties of nucleonic neutron stars with $M = 1.4\,\mathrm{M}_\odot$ and $M_{\max}$ for the indicated EOSs. For each mass, the compactness parameter $\beta = (GM/c^2R) \simeq (1.475\,R)(M/\mathrm{M}_\odot)$, n_c, P_c and y_c are the central values of the density, pressure and proton fraction, respectively.

Property	APR	MS-A	MS-B	MS-C	Units
$R_{1.4}$	11.74	13.21	12.41	11.85	km
$\beta_{1.4}$	0.176	0.157	0.167	0.174	
$n_{c,1.4}/n_0$	3.35	2.05	2.80	3.72	
$P_{c,1.4}$	89.33	41.78	64.43	94.24	MeV fm^{-3}
$y_{c,1.4}$	0.11	0.104	0.106	0.106	
$R_{\max}$	10.26	12.44	10.91	9.94	km
$M_{\max}$	2.185	2.63	2.21	1.83	$\mathrm{M}_\odot$
$\beta_{\max}$	0.314	0.312	0.299	0.273	
$n_{\mathrm{c,max}}/n_0$	6.97	4.71	6.38	8.30	
$P_{\mathrm{c,max}}$	884.69	498.32	632.66	664.60	MeV fm^{-3}
$y_{\mathrm{c,max}}$	0.16	0.14	0.14	0.128	

An examination of L in Table 4.2, and, $R_{1.4}$ and $R_{\max}$ in Table 4.3 reveals an anti-correlation between these quantities for the MS models. That is, smaller values of L lead to larger values of $R_{1.4}$ and $R_{\max}$. In particular, this trend for the L-$R_{1.4}$ relation is opposite to that observed for many EOS models. The reason for this reversal in the

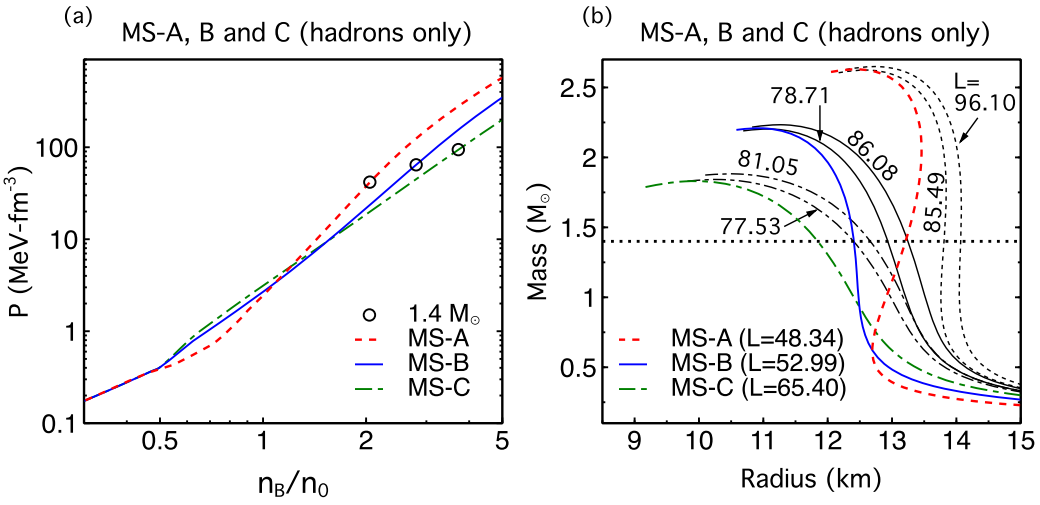

Figure 4.1: Pressure versus baryon density and M-R curves for the MS models in Table 4.4. The circles on the pressure curves in panel (a) shown indicate the densities of 1.4 $M_\odot$ stars for EOSs that yield the smallest radius $R_{1.4}$ in each class of MS models.

generally believed opposite trend becomes clear when one examines closely the P vs n_B and M-R relations for the MS models shown in fig. 4.1. The central densities of 1.4 $M_\odot$ stars for the EOSs chosen are all $\gtrsim 2\,n_0$ with that of the star corresponding to MS-C being the farthest. The slope of the symmetry energy parameter, L, however, refers to that at n_0. The behaviors of the pressures, see panel (a) in this figure, for $n_B \gtrsim 2\,n_0$ for all of these EOSs are distinctly different from their corresponding behaviors at $n_B \simeq n_0$. The corresponding M-R curves in fig. 4.1 (b) and Table 4.4 also clearly show how the value of $n_{c,1.4}$ differs in each of these cases.

Interestingly enough, the standard L-$R_{1.4}$ is held within a class of MS models with the same effective mass; see fig. 4.1 (b) and Table 4.4. Evidently, the manner in which the size of a 1.4 $M_\odot$ is built depends sensitively on the behavior of the EOS well above n_0. These features deliver the alert that the standard L-$R_{1.4}$ correlation is not as universal as generally thought.

Table 4.4: Effective mass dependence of the L-$R_{1.4}$ relation. Entries are as in Tables 4.2 and 4.3, but organized differently.

Model	m^*/M	Λ_σ	Λ_ω	L (MeV)	$R_{1.4}$ (km)	$n_{c,1.4}/n_0$
MS-A	0.662	0.001	0.05	48.34	13.21	2.05
	0.662	0.001	0.01	85.49	13.81	2.00
	0.662	0.0	0.0	96.1	14.07	1.93
MS-B	0.763	0.001	0.05	52.99	12.41	2.80
	0.763	0.001	0.01	78.71	12.93	2.68
	0.763	0.0	0.0	86.08	13.25	2.53
MS-C	0.847	0.001	0.05	65.40	11.85	3.72
	0.847	0.001	0.01	77.53	12.41	3.35
	0.847	0.0	0.0	81.05	12.67	3.12

Quark EOSs

For completeness, we briefly describe the EOSs considered to describe the quark phase in this work. Details can be found in the references cited. Since the discovery of $2\,M_\odot$ neutron stars [C$^+$19, AFW$^+$13, DPR$^+$10], the traditional MIT bag [BC76a] and NJL [Kun89] models have been supplemented with vector interactions [KF15] to achieve consistency with data. These models have been termed vMIT, vBag, vNJL, etc., and are outlined below.

The bag model and its variations

The Lagrangian density of the MIT bag model is [BC76a]

$$\mathcal{L} = \sum_i [\, \overline{\psi}_i(i\partial\!\!\!/ - m_i - B)\psi_i + \mathcal{L}_{\rm int} \,]\Theta \tag{4.5}$$

which describes quarks of mass m_i confined within a bag as denoted by the Θ function. For three flavors, $i = u, d, s$ and three colors, $N_c = 3$ of quarks, the number and baryon densities, energy density, pressure and chemical potentials in the bag model are [BC76a]

$$\begin{aligned} n_i &= 2N_c \int^{k_{Fi}} \frac{d^3k}{(2\pi)^3}\,, \quad n_{\rm B} = \frac{1}{3}\sum_i n_i \\ \varepsilon_Q &= 2N_c \sum_i \int^{k_{Fi}} \frac{d^3k}{(2\pi)^3}\,\sqrt{k^2+m_i^2} + \varepsilon_{\rm pert} + B \\ P_Q &= \frac{2N_c}{3}\sum_i \int^{k_{Fi}} \frac{d^3k}{(2\pi)^3}\,\frac{k^2}{\sqrt{k^2+m_i^2}} + P_{\rm pert} - B \\ \mu_i &= \sqrt{k_{Fi}^2+m_i^2} + \mu_{{\rm pert},i}\,. \end{aligned} \tag{4.6}$$

The superscript k_{Fi} in the integral signs is the Fermi wave number for each species i at which the integration over k is terminated at zero temperature. The first terms in ε_Q and P_Q are free Fermi gas contributions, $\varepsilon_{\rm FG}$ and $P_{\rm FG}$, respectively, the second terms are QCD perturbative corrections due to gluon exchange corresponding to $\mathcal{L}_{\rm int}$ and B is the so-called bag constant which accounts for the cost in confining the quarks into a bag. The quark masses m_i are generally taken to be current quark masses. Often, the u and d quark masses are set to zero (as at high density, k_{Fi} in these cases far exceed m_i), whereas that of the s quark is taken at its Particle Data Group value. References [BC76a, BC76b, FM78, FJ84, KRV10, KV16, GKR$^+$18] detail the QCD perturbative calculations of $\varepsilon_{\rm pert}$ and $P_{\rm pert}$, and the ensuing results for the structure of normal neutron stars containing quarks within the cores as well as self-bound strange quark stars. At leading order of QCD corrections, the results are qualitatively similar to what is obtained by just using the Fermi gas results with an appropriately chosen value of B [PBP90].

In recent years, variations of the bag model have been adopted [KF15, GCS19] to calculate the structure of neutron stars with quarks in their cores to account for $2\,{\rm M}_\odot$ maximum-mass stars. Termed as vMIT or vBag models, the QCD perturbative results are dropped and replaced by repulsive vector interactions between quarks in such works. We

will provide some numerical examples of the vMIT model for contrast with other models as those of the vBag model turn out to be qualitatively similar.

The vMIT model

The form $\mathcal{L}_{\rm int} = -G_v \sum_i \bar{\psi}\gamma_\mu V^\mu \psi + (m_V^2/2) V_\mu V^\mu$, where interactions between the quarks occur via the exchange of an vector-isoscalar meson V^μ of mass m_V, is chosen in ref. [GCS19]. Here, the quark masses are chosen close to their current quark masses. Explicitly,

$$\begin{aligned} \varepsilon_Q &= \sum_i \varepsilon_{\rm FG,i} + \frac{1}{2}\left(\frac{G_v}{m_V}\right)^2 n_Q^2 + B \\ P_Q &= \sum_i P_{\rm FG,i} + \frac{1}{2}\left(\frac{G_v}{m_V}\right)^2 n_Q^2 - B \\ \mu_i &= \sqrt{k_{Fi}^2 + m_i^2} + \left(\frac{G_v}{m_V}\right)^2 n_Q \,, \end{aligned} \tag{4.7}$$

where $n_Q = \sum_i n_i$ and the bag constant B is chosen appropriately to enable a transition to matter containing quarks. Note that terms associated with the vector interaction above are similar to those in hadronic models. In the results reported below, we vary the model parameters in the range $B^{1/4} = (155 - 180)$ MeV and $a = (G_v/m_V)^2 = (0.1 - 0.3)$ fm^2.

The vNJL model

In its commonly used form, the Lagrangian density for the vNJL model in the mean field approximation is

$$\begin{aligned} \mathcal{L} &= \bar{q}(i\partial\!\!\!/ - \hat{m}_0)q + G_s \sum_{k=0}^{8} \left[(\bar{q}\lambda_k q)^2 + (\bar{q} i\gamma_5 \lambda_k q)^2 \right] \\ &- K\Big[\det{}_f(\bar{q}(1+\gamma_5)q) + \det{}_f(\bar{q}(1-\gamma_5)q) \Big] \\ &+ G_v \sum_i (\bar{q}\gamma^\mu q)^2 \,. \end{aligned} \tag{4.8}$$

Here, q denotes a quark field with three flavors u, d, s and three colors, $\hat{m}_0$ is the 3×3 diagonal current quark mass matrix, λ_k represents the 8 generators of SU(3), and λ_0 is

proportional to the identity matrix. The four-fermion interactions are from the original formulation of this model [NJL61], whereas the flavor mixing, determinental interaction is added to break the $U_A(1)$ symmetry [tH86]. The last term accounts for vector interactions [Bub05]. As the constants G_s, K and G_v are dimensionful, the quantum theory is non-renormalizeable. Therefore, an ultraviolet cutoff Λ is imposed, and results are meaningful only for quark Fermi momenta well below this cutoff.

The Lagrangian density in Eq. (4.8) leads to the energy density

$$\begin{aligned} \varepsilon &= \varepsilon_{\rm FG} + \varepsilon_{\rm int} \\ \varepsilon_{\rm int} &= -2\,N_c \sum_i \int^{\Lambda} \frac{d^3k}{(2\pi)^3} \left(\sqrt{k^2+m_i^2} - \sqrt{k^2+m_{o,i}^2} \right) \\ &+ 2G_s \sum_i \langle \overline{q}_i q_i \rangle - 4K \prod_i \langle \overline{q}_i q_i \rangle + 2G_v \sum_i n_i^2 \,, \end{aligned} \tag{4.9}$$

where the sums above run over u, d, s. The subscript "0" denotes current quark masses and the superscript Λ in the integral sign indicates that an ultraviolet cutoff Λ is imposed on the integration over k. In both $\varepsilon_{\rm FG}$ [see Eq. (4.6)] and $\varepsilon_{\rm int}$, the quark masses m_i are dynamically generated by requiring that ε be stationary with respect to variations in the quark condensate $\langle \overline{q}_i q_i \rangle$:

$$m_i = m_{0,i} - 4G_s \langle \overline{q}_i q_i \rangle + 2K \langle \overline{q}_j q_j \rangle \langle \overline{q}_k q_k \rangle \,, \tag{4.10}$$

(q_i, q_j, q_k) representing any permutation of (u, d, s). The quark condensate $\langle \overline{q}_i q_i \rangle$ is given by

$$\langle \overline{q}_i q_i \rangle = -2N_c \int_{k_{Fi}}^{\Lambda} \frac{d^3k}{(2\pi)^3} \frac{m_i}{\sqrt{k^2+m_i^2}} \,, \tag{4.11}$$

and the quark number density $n_i = \langle q_i^\dagger q_i \rangle$ is as in Eq. (4.6). Note that the integrals appearing in eqs. (4.9)-(4.11) can all be evaluated analytically. eqs. (4.10) and (4.11) render the dynamically-generated masses m_i density-dependent and which tend to $m_{0,i}$ at high density mimicking the restoration of chiral symmetry in QCD.

To facilitate a comparison between the vBag and vNJL models, ref. [BO99] recommends a constant energy density $B_0 = \varepsilon_{\rm int}|_{m_u=m_d=m_s=0}$ to be added to $\varepsilon_{\rm int}$ which makes the vacuum energy density zero. With this addition, the energy density takes the form $\varepsilon = \varepsilon_{\rm FG} + B_{\rm eff}$, with $B_{\rm eff} = B_0 + \varepsilon_{\rm int}$.

The quark chemical potentials are

$$\mu_i = \left.\frac{d\varepsilon}{dn_i}\right|_{n_j,n_k} = \sqrt{m_i^2 + k_{Fi}^2} + 4G_v n_i \tag{4.12}$$

using which the pressure is obtained from the thermodynamic identity

$$P = \sum_i n_i\mu_i - \varepsilon = P_{\rm FG} - B_{\rm eff}\,. \tag{4.13}$$

To mimic confinement absent in the vNJL model, often a constant term $B_{\rm dc}$ is used with the replacement $B_{\rm eff} \to B_{\rm eff} - B_{\rm dc}$.

For numerical calculations, we use the HK parameter set [HK94]: $\Lambda = 631.4$ MeV, $G_s\Lambda^2 = 1.835$, $K\Lambda^5 = 0.29$, $m_{u,d} = 5.5$ MeV, $m_s = 135.7$ MeV and $B_{\rm dc} = 0$.

The vBag model

In ref. [KF15], vector interactions are used in the form of flavor-independent four-fermion interactions as in the NJL models (described below): $\mathcal{L}_{\rm int} = G_v \sum_i (\bar{\psi}\gamma^\mu\psi)^2$. In this case [KF15],

$$\begin{aligned}
\varepsilon_Q &= \sum_i \varepsilon_{\rm FG,i} + \frac{G_v}{2}\sum_i n_i^2 + B_{\rm eff} \\
P_Q &= \sum_i P_{\rm FG,i} + \frac{G_v}{2}\sum_i n_i^2 - B_{\rm eff} \\
\mu_i &= \sqrt{k_{Fi}^2 + m_i^2} + G_v n_i\,,
\end{aligned} \tag{4.14}$$

where the explicit forms of $\varepsilon_{\rm FG,i}$ and $P_{\rm FG,i}$ can be read off from Eq. (4.6). The effective bag constant $B_{\rm eff}$ in this model is composed of two parts: $B_{\rm eff} = \sum_i B_\chi^i - B_{\rm dc}$, where the flavor

dependent chiral bag constant

$$\begin{aligned} B_\chi^i &= P(m_{0,i}, k_{Fi}=0) - P(m_i, k_{Fi}=0) \\ &= 2N_c \sum_i \int^\Lambda \frac{d^3k}{(2\pi)^3} \left(\sqrt{k^2+m_{o,i}^2} - \sqrt{k^2+m_i^2} \right), \end{aligned} \tag{4.15}$$

where m_i is a dynamically generated quark mass as in the NJL model, $m_{0,i}$ is the current quark mass, and Λ is an ultraviolet cut-off on the integration over k. The quantity $B_{\rm dc}$ is tuned to control the onset of quark deconfinement.

Note that B_χ^i and $B_{\rm dc}$, and thus $B_{\rm eff}$, are independent of density. Unlike in the vNJL model in which all terms in the energy density and pressure are calculated with density-dependent dynamical masses m_i, the Fermi gas contributions in the vBag model are calculated with $m_i(k_{Fi}=0)$. Consequences of the vBag model on neutron star structure have been studied extensively in refs. [KF15, WITJ18] (and in this work), and will not be repeated here as the vNJL model provides a more general scheme.

Charge neutrality and beta-equilibrium conditions

Equilibrium with respect to weak-interaction processes $d \to u e^- \bar{\nu}_e$ and $s \to u e^- \bar{\nu}_e$ leads to the chemical potential equalities $\mu_d = \mu_u + \mu_e = \mu_s$ in neutrino-free matter. Charge neutrality requires that $2n_u - n_d - n_s - n_e = 0$. Together with the baryon number relation $n_u + n_d + n_s = 3\,n_{\rm B}$, the simultaneous solution of the equations

$$\begin{aligned} (1+x_e) + \left[x_s^{2/3} + \frac{C_s - C_d}{r^{2/3}} \right]^{3/2} + x_s &= 3 \\ \left[(1+x_e)^{2/3} + \frac{C_u}{r^{2/3}} \right]^{1/2} - \left[x_s^{2/3} + \frac{C_s}{r^{2/3}} \right]^{1/2} + (3x_e)^{1/3} &= 0 \end{aligned} \tag{4.16}$$

assures that quark matter with the three flavors u, d, s is charge neutral and in beta-equilibrium. In Eq. (4.16), $x_i = n_i/n_{\rm B}$ denote the particle concentrations, $r = n_{\rm B}/n_0$

and the factor $C_i = m_i^2/(\pi^{4/3} n_0^{2/3}), i = u, d, s$. Note that C_i can depend on the density compression ratio r through $m_i \equiv m_i(r)$ as in the vNJL model. The concentrations of the u and d quarks are given by

$$x_u = 1 + x_e \quad \text{and} \quad x_d = \left[x_s^{2/3} + \frac{C_s - C_d}{r^{2/3}} \right]^{3/2} , \tag{4.17}$$

respectively. Owing to the charges carried by the quarks, the electron concentration in quark matter is generally very small with increasing r.

4.3 Treatment of Phase Transitions

First-order transitions

The manner in which the hadron-quark transition occurs is unknown. Even if the phase transition is assumed to be of first order, description of the transition depends on the knowledge of the surface tension σ_s between the two phases [ARRW01, MFPSB10, LGAA13, FHS19]. In view of uncertainties in the magnitude of σ_s, two extreme cases have been studied in the literature.

Maxwell Construction

For very large values of σ_s, a Maxwell construction in which pressure and chemical potential equalities, $P(H) = P(Q)$ and $\mu_n(H) = \mu_n(Q)$, are established between the two phases has been deemed appropriate. In charge neutral and beta-equilibrated matter, only one baryon chemical potential, often chosen to be μ_n, is needed to conserve baryon number as local charge neutrality is implicit. The range of densities over which these equalities hold can be found using the methods detailed in refs. [CMPL14, LLPR83].

Gibbs Construction

For very low values of σ_s, a Gibbs construction in which a mixed phase of hadrons and quarks is present is more appropriate [Gle92, Gle01]. The description of the mixed

phase is achieved by satisfying Gibbs' phase rules: $P(H) = P(Q)$ and $\mu_n = \mu_u + 2\mu_d$. Further, the conditions of global charge neutrality and baryon number conservation are imposed through the relations

$$\begin{aligned} Q &= f\,Q(H) + (1-f)\,Q(Q) = 0 \\ n_{\rm B} &= f\,n_{\rm B}(H) + (1-f)\,n_{\rm B}(Q)\,, \end{aligned} \tag{4.18}$$

where f represents the fractional volume occupied by hadrons, and is solved for at each $n_{\rm B}$. Unlike in the pure phases of the Maxwell construction, $Q(H)$ and $Q(Q)$ do not separately vanish in the Gibbs mixed phase. The total energy density is $\varepsilon = f\varepsilon(H) + (1-f)\varepsilon(Q)$. Relative to the Maxwell construction, the behavior of the pressure vs density is smooth in the case of Gibbs construction. Discontinuities in its derivatives with respect to density, reflected in the squared speed of sound $c_s^2 = dP/d\varepsilon$, will however be present at the densities where the mixed phase begins and ends.

The Maxwell and Gibbs constructions represent extreme cases to treat first-order phase transitions. Reality may lie in between these two cases. However, there are situations in which neither method can be applied as the required pressure and chemical potential equalities cannot be met for many hadronic and quark EOSs [BHK$^+$18]. In such cases, an interpolatory method which makes the transition a smooth crossover has been used [MHT13, FK16, KPSB15, BHK$^+$18].

Crossover transitions

As it is not clear that a first-order phase hadron-to-quark transition at finite baryon density is demanded by fundamental considerations, crossover or second-order transitions have also been explored recently; see, e.g., refs. [BHK$^+$18, DNS15, MR19]. As details of results ensuing from the model of ref. [DNS15] have been recorded earlier in refs. [DS10, NDS10], we will only examine the cases of interpolated and quarkyonic models in what follows.

Interpolated EOS

We follow the simple recipe in ref. [MHT13] where the interpolated EOS in the hadron-quark crossover region is characterized by its central value $\bar{n}$ and width Γ. Pure hadronic matter exists for $n \lesssim \bar{n} - \Gamma$, whereas a phase of pure quark matter is found for $n \gtrsim \bar{n} + \Gamma$. In the crossover region, $\bar{n} - \Gamma \lesssim n \lesssim \bar{n} + \Gamma$, strongly interacting hadrons and quarks coexist in prescribed proportions. The interpolation is performed for pressure vs baryon number density according to

$$P(n) = P_H(n) f_-(n) + P_Q(n) f_+(n) \tag{4.19}$$

$$f_\pm(n) = \frac{1}{2}\left[1 \pm \tanh\left(\frac{n - \bar{n}}{\Gamma}\right)\right], \tag{4.20}$$

where P_H and P_Q are the pressure in pure hadronic and pure quark matter, respectively. The interpolated EOS for the crossover, Eq. (4.19), is different from that of the Gibbs construction within the conventional picture of a first-order phase transition in that the pressure equality between the two phases has been abandoned. Also, f_- and f_+ are not solved for, but chosen externally. (Alternative forms of interpolation have also been suggested in refs. [FK16, KPSB15], but do not qualitatively change the outcome.) The energy density ε vs n is obtained by integrating $P = n^2 \partial(\varepsilon/n)/\partial n$:

$$\begin{aligned} \varepsilon(n) &= \varepsilon_H(n) f_-(n) + P_Q(n) f_+(n) + \Delta\varepsilon \\ \Delta\varepsilon &= n \int_{\bar{n}}^{n} \mathrm{d}n' \left[\varepsilon_H(n') - \varepsilon_Q(n')\right] \frac{g(n')}{n'}, \\ g(n') &= \frac{\mathrm{sech}^2 X}{2\Gamma}, \quad X = \frac{n' - \bar{n}}{\Gamma}. \end{aligned} \tag{4.21}$$

Quarkyonic matter

The transition to matter containing quarks in the model termed quarkyonic matter [MP07, MR19] is second order as the squared speed of sound $c_s^2 = dP/d\varepsilon$ is smoothly continuous, but its derivative is not. This model is a departure from the first-order phase

transition models insofar as once quarks appear, both nucleons and quarks are present until asymptotically large densities when the nucleon concentrations vanish. Keeping the structure of the quarkyonic matter model as in refs. [MP07, MR19] in which isospin symmetric nuclear matter (SNM) and pure neutron matter (PNM) were considered, we present below its generalization to charge neutral and beta-equilibrated neutron star matter. In quarkyonic matter, the appearance of quarks is subject to the threshold condition [MR19]

$$k_{Fq} = \frac{(k_{FB} - \Delta)}{N_c}\,\Theta(k_{FB} - \Delta)\,, \tag{4.22}$$

where k_{FB} is the baryon momentum, $N_c = 3$ is the number of colors, and the momentum threshold Δ is chosen to be

$$\Delta = \frac{\Lambda_Q^3}{k_{FB}^2} + \kappa\frac{\Lambda_Q}{N_c^2}\,. \tag{4.23}$$

For hadronic matter containing both neutrons and protons, independent Δ's (Δ_n and Δ_p) with their own k_{FB}'s (k_{Fn} and k_{Fp}) must be used. Above, $\Lambda_Q \sim \Lambda_{\rm QCD} \simeq 300 - 500$ MeV, and $\kappa \simeq 0.1 - 0.3$ is suitably chosen to preserve causality. In PNM, the transition density, $n_{\rm trans}$, for the appearance of quarks is $0.77\,(3.55)\,n_0$ for $\Delta = 300\,(500)$ MeV and $\kappa = 0.3$, where n_0 is the SNM equilibrium density. The corresponding values for $\kappa = 0.1$ are $0.75\,n_0$ and $3.47\,n_0$, respectively, and shows the weak dependence of $n_{\rm trans}$ on κ. Unlike in the other approaches, the transition density at which quarks begin to appear in this model is independent of the EOSs used in the hadronic and quark sectors, being dependent entirely on $\Lambda_{\rm QCD}$ and large N_c physics.

The total baryon density of quarkyonic matter is

$$n_{\rm B} = \sum_{i=n,p} 2\int_{N_c k_{Fq}}^{k_{Fi}} \frac{d^3k}{(2\pi)^3} + \sum_{q=u,d,s}\frac{2N_c}{3}\int_0^{k_{Fq}}\frac{d^3k}{(2\pi)^3}\,. \tag{4.24}$$

Notice that once quarks appear, the shell width Δ in which nucleons reside decreases with density as $n_{\rm B}^{-2/3}$ yielding the preponderance of quarks with increasing $n_{\rm B}$. Including leptonic (electron and muon) contributions ε_ℓ, the total energy density is

$$\begin{aligned}\varepsilon &= \sum_{i=n,p} 2\int_{N_c k_{Fq}}^{k_{Fi}} \frac{d^3k}{(2\pi)^3}\, e_k + \varepsilon_{\rm int}(n_n, n_p) \\ &+ \sum_{q=u,d,s} 2N_c \int_0^{k_{Fq}} \frac{d^3k}{(2\pi)^3}\ \sqrt{k^2 + M_q^2} + \varepsilon_{\rm int}(q_k, q_\ell) \\ &+ \sum_{\ell=e^-,\mu^-} \varepsilon_\ell\,, \end{aligned} \tag{4.25}$$

where e_k is the single particle kinetic energy inclusive of the rest mass energy. The nucleonic part of the energy density for $n \gtrsim 0.5\, n_0$ can be taken from a suitable potential or field-theoretical model that is constrained by nuclear systematics near nuclear densities and preserves causality at high densities. Below $0.5\, n_0$, the energy density is that of crustal matter as in, e.g., refs. [NV73, BPS71]. It is important to realize that the term $\varepsilon_{\rm int}(n_n, n_p)$ contributes in regions where $k_{FB} < \Delta$ as well as where $k_{FB} > \Delta$.

The chemical potentials and pressure are obtained from

$$\begin{aligned}\mu_k = \left.\frac{\partial\varepsilon}{\partial n_k}\right|_{n_j},\ P &= n_{\rm B}^2 \frac{\partial(\varepsilon/n_{\rm B})}{\partial n_{\rm B}} + \sum_{\ell=e^-,\mu^-} P_\ell \\ &= \sum_k n_k\mu_k - \varepsilon\,, \end{aligned} \tag{4.26}$$

where the sum above runs over all fermions.

As with nucleons, an appropriate choice of the quark EOS is also indicated. Reference [MP07] set $\varepsilon_{\rm int}(q_k, q_\ell) = 0$, and the quark masses M_q were taken as $M_n/3$. The use of the nucleon constituent quark masses takes account of quark-gluon interactions to a certain degree as has been noted in the case of finite temperature QCD as well. This procedure, however, omits density dependent contributions from interactions between quarks. In our work, we will employ quark models (such as vMIT, vNJL) in which contributions from interacting quarks are included. Subtleties involved in the calculation

of the kinetic part of the nucleon chemical potentials and in satisfying the thermodynamic identity are detailed in Appendix 4.5.

This model has a distinct behavior for $c_s^2 = dP/d\varepsilon$ vs n_B in that c_s^2 exhibits a maximum (its location controlled by Λ_Q, and the magnitude depending on both Λ_Q and κ) before approaching the value of 1/3 characteristic of quarks at asymptotically large densities [MP07].

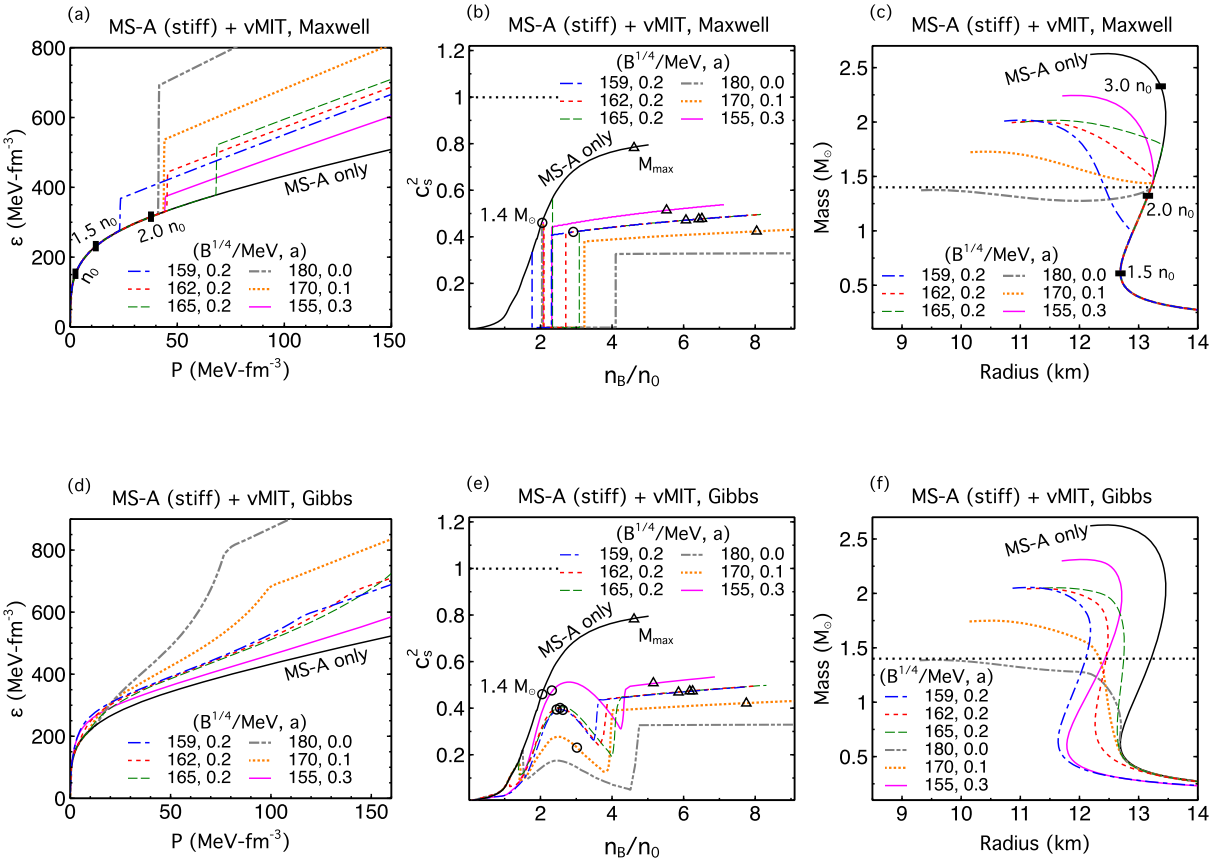

Figure 4.2: Energy density vs pressure, squared speed of sound vs ratio of baryon density to the nuclear equilibrium density, and mass vs radius curves for the models indicated. Panels (a)-(c) are for Maxwell construction, whereas (d)-(f) are for Gibbs construction; the quark model parameters used are in the inset and results are for beta-equilibrated matter. The 1.4 $M_\odot$ and maximum-mass stars are marked with open circles and triangles in $c_s^2(n_B)$ plots.

4.4 Results with Phase Transitions

The nucleonic EOSs chosen in this study satisfy the available nuclear systematics near the nuclear equilibrium density (see Tables I-III). Their supra-nuclear density behavior can, however, be varied to yield a soft or stiff EOS by varying the parameters in the chosen model. Depending on the quark EOS examined, such as vMIT, vNJL or of quarkyonic matter, the examination of a broad range of transitions to quark matter - soft-to-soft, soft-to-stiff, stiff-to soft and stiff-to-stiff - become possible. For both first-order and crossover transitions, we calculate the mass-radius curves and tidal deformabilities and discuss the results in view of the existing observational constraints. Of particular relevance to the zero-temperature EOS is the limit set by the data on the dimensionless tidal deformability [FH08, Fav14]

$$\tilde{\Lambda} = \frac{16}{13}\frac{(m_1 + 12m_2)m_1^4\,\Lambda_1 + (m_2 + 12m_1)m_2^4\,\Lambda_2}{(m_1 + m_2)^5}. \tag{4.27}$$

For each star, the tidal deformability (or induced quadrupole polarizability) is given by [Lov09]

$$\Lambda_{1,2} = \frac{2}{3}k_2^{1,2}\left(\frac{R_{1,2}\,c^2}{G\,m_{1,2}}\right)^5 , \tag{4.28}$$

where the dimensionless Love number $k_2^{1,2}$ depends on the structure of the star, and therefore on the mass and the EOS. Here, G is the gravitational constant, and $R_{1,2}$ are the radii. The computation of $k_2^{1,2}$ with input EOSs is described in refs. [TC67, Hin08, DN09]. For a wide class of neutron star EOSs, $k_2^{1,2} \simeq 0.05 - 0.15$ [Hin08, HLLR10b, PPL10].

Combining the electromagnetic (EM) [A$^+$17b] and gravitational wave (GW) information from the merger GW170817, ref. [MM17] provides constraints on the radius $R_{\rm ns}$ and maximum gravitational mass $M^g_{\rm max}$ of a neutron star:

$$\begin{aligned} M^g_{\rm max} &\lesssim 2.17\,{\rm M}_\odot\,, \\ R_{1.3} &\gtrsim 3.1\,GM^g_{\rm max} \simeq 9.92\ {\rm km}\,, \end{aligned} \tag{4.29}$$

where $R_{1.3}$ is the radius of a $1.3\,\mathrm{M}_\odot$ neutron star and its numerical value above corresponds to $M^g_{\max} = 2.17\,\mathrm{M}_\odot$. These estimates have been revisited in a recent analysis in ref. [SZKF19] in which a weaker constraint on the lower limit on the maximum mass $M^g_{\max} \lesssim 2.3\,\mathrm{M}_\odot$ has been reported.

First-order transitions: Maxwell vs. Gibbs

We first survey the allowed parameter space for valid first-order phase transitions, namely, a critical pressure exists above which quark matter is energetically favored. We then proceed with both Maxwell and Gibbs constructions, calculating quantities to be compared with observational constraints. Our results are summarized in figs. 4.2-4.4. Where possible, we also characterize the behavior of the hadron-to-quark transition with quantities introduced in the "Constant-Sound-Speed (CSS)" approach in ref. [AHP13]. This approach can be viewed as the lowest-order Taylor expansion of the high-density EOS about the transition pressure, P_{trans}, by specifying the discontinuity in energy density, $\Delta\varepsilon$, at the transition and the density-independent squared sound speed, c^2_{QM}, in quark matter.

MS-A + vMIT (stiff → soft/stiff)

Fixing the hadronic EOS to be the stiff model MS-A, six parameter sets of $(B^{1/4}, a)$ in the vMIT model. Here, B is the bag constant and the parameter $a = (G_v/m_v)^2$ measures the strength of the vector interactions between quarks, are explored in this case. The Bag constant is adjusted so that the transition to quark matter occurs at $n_{\mathrm{trans}} = 1.5 - 2.4\,n_0$ and the finite vector coupling a stiffens the quark matter EOS. Soft hadronic EOSs are not applied, as they either (with softer quark EOSs) violate the $M_{\max} \geq 2\,\mathrm{M}_\odot$ constraint or (with stiffer quark EOSs) cannot establish a valid first-order phase transition, i.e., there is no intersection between the two phases in the P-μ plane. We note that this limitation

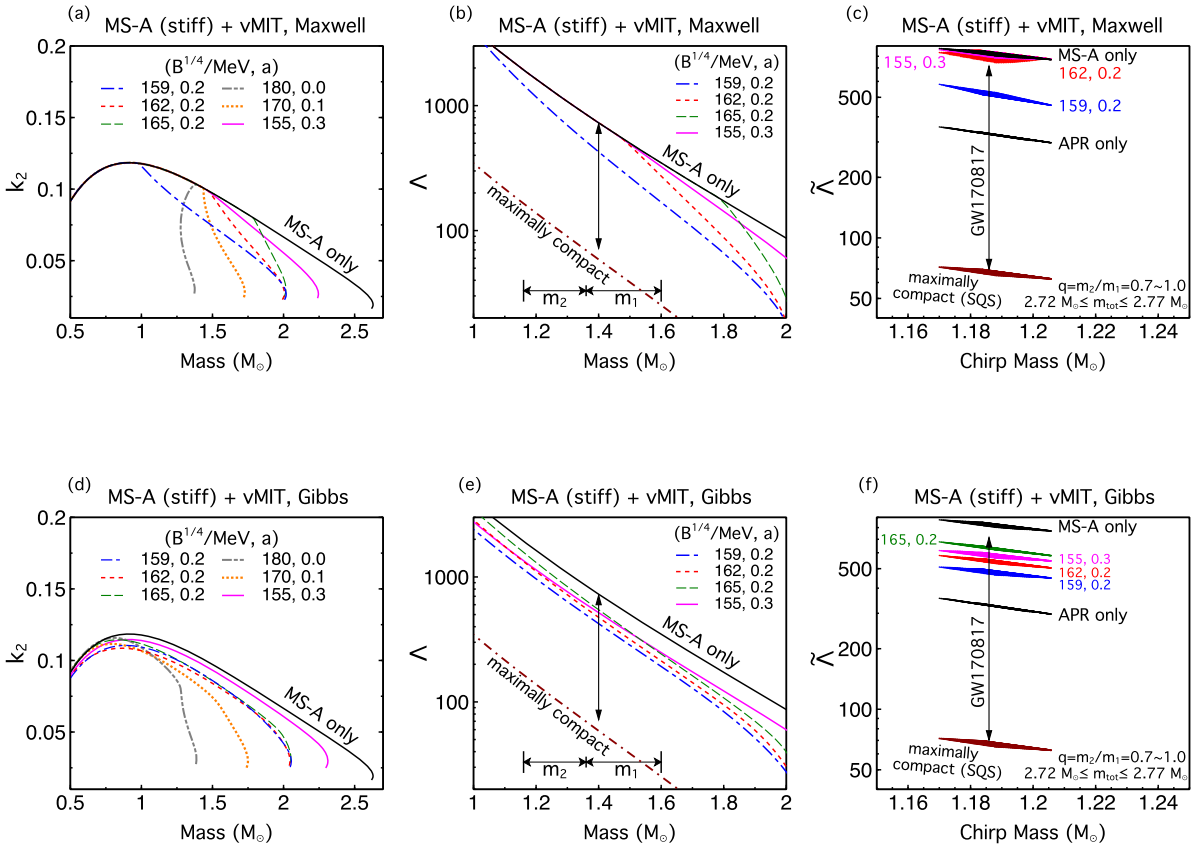

Figure 4.3: Tidal deformability parameters k_2 (Love number), Λ and $\tilde{\Lambda}$ in eqs. (4.27) and (4.28) as functions of the indicated masses. For comparison, results of $\tilde{\Lambda}$ for the EOS of the APR model are also shown.

(hadronic matter being stiff) does not necessarily hold if a generic parameterization such as CSS is utilized instead of specific quark models to perform first-order transitions.

In the vMIT model, the sound speed varies little even with the inclusion of vector repulsive interactions within the star (see fig. 4.2 (b) and (e)) and can be approximated as being density independent. The mass-radius topology with the Maxwell construction is determined by the three parameters $(P_{\rm trans}/\varepsilon_{\rm trans}, \Delta\varepsilon/\varepsilon_{\rm trans}, c^2_{\rm QM})$ at the phase transition, giving rise to either connected, disconnected or both branches of stable hybrid stars. Here, $P_{\rm trans}$ and $\varepsilon_{\rm trans}$ are the pressure and energy density in hadronic matter at the transition,

respectively, $\Delta\varepsilon$ is the discontinuity in energy density at $P_{\rm trans}$, and $c^2_{\rm QM}$ is the squared sound speed in quark matter just above $P_{\rm trans}$. The threshold value $\Delta\varepsilon_{\rm crit}$ below which there is always a stable hybrid branch connected to the purely hadronic branch is given by $\Delta\varepsilon_{\rm crit}/\varepsilon_{\rm trans} = \frac{1}{2} + \frac{3}{2}P_{\rm trans}/\varepsilon_{\rm trans}$ [Sei71, SZH83, Lin98]. The relevant quantities for the mapping between the stiff MS-A+vMIT model (Maxwell) and the CSS parametrization are listed in Table 4.5.

After extensively varying all parameters and calculating the corresponding mass-radius relations, we find that $a = 0.18$ is most likely the smallest value (corresponding to $c^2_{\rm QM} \approx 0.4$) that barely ensures $M_{\rm max} \simeq 2\,{\rm M}_\odot$. When a is increased from zero, the energy density discontinuity becomes progressively smaller ($\Delta\varepsilon/\varepsilon_{\rm trans} \lesssim 0.5$) and eventually the twin-star solutions disappear, roughly at $a \geq 0.15$. Within the range $a = 0.18 - 0.3$, the $M(R)$ curves of stable hybrid stars obtained are continuous, and quarks can appear at $1.0 \leq M_{\rm trans} \leq 1.8\,{\rm M}_\odot$, pertinent to the range of component masses in binary neutron star (BNS) mergers. For too large vector interaction couplings, e.g., $a = 0.5$, the onset for quarks is beyond the central density of the maximum-mass hadronic star, and thus no stable quark cores would be present even though QM is sufficiently stiff.

fig. 4.2 (c) shows that requiring $M_{\rm max} \geq 2\,{\rm M}_\odot$ excludes certain twin-star solutions obtained from EOSs with zero (gray dash-dot-dotted) and small (orange dotted) repulsive vector interactions between quarks, mainly due to the insufficient stiffness of the quark matter EOS. Moreover, the typical neutron star radius $R_{1.4}$ can be observationally constrained by radius estimates from x-ray emission and/or tidal deformability (Λ) measurements in pre-merger gravitational-wave detections. For hybrid EOSs with a sharp phase transition, the value of $R_{1.4}$ or $\Lambda_{1.4}$ is sensitive to the onset density $n_{\rm trans}$, above which $M(R)$ and $\Lambda(M)$ deviate from normal hadronic EOSs without a sharp transition. We demonstrate this effect in fig. 4.3 by confronting calculated tidal deformations with inferred bounds from the first BNS event GW170817 [A$^+$17c, A$^+$18, DFL$^+$18].

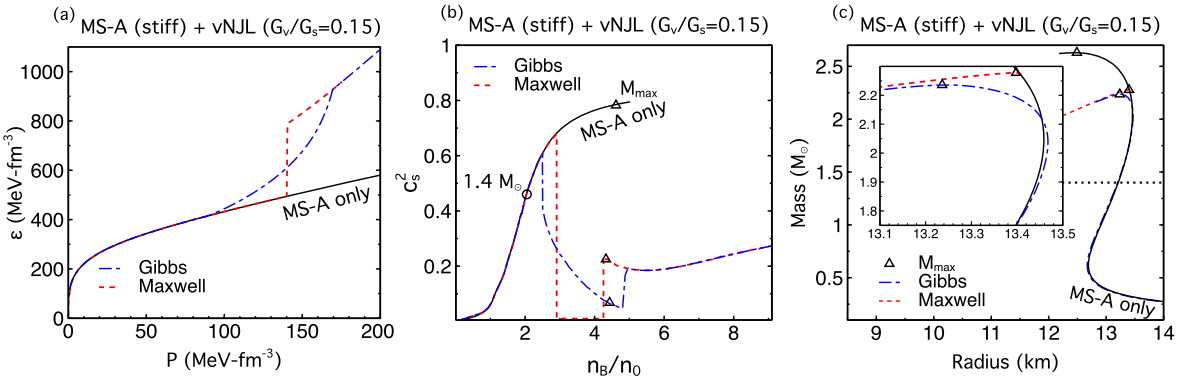

Figure 4.4: As in fig. 4.2, but for Maxwell and Gibbs constructions in MS-A (stiff) + vNJL (soft) models. Here, BNS merger observables with $m_1, m_2 = 1.0-1.6\,\mathrm{M}_\odot$ only constrain the hadronic matter EOS as the onset density for quarks is too high ($M_{\rm trans} \gtrsim 1.7\,\mathrm{M}_\odot$). Since the stiff MS-A is ruled out by $\tilde{\Lambda}(\mathcal{M})$ of GW170817 (see fig. 4.3), this indicates that vNJL model (or NJL-type models) is ruled out in the first-order transition scenario. Resorting to the crossover scenario is inevitable for it to survive.

With high accuracy, the chirp mass $\mathcal{M} = (m_1 m_2)^{3/5}/(m_1 + m_2)^{1/5}$, where $m_{1,2}$ are the masses of the merging neutron stars, was determined to be $\mathcal{M} = 1.186^{+0.001}_{-0.001}\mathrm{M}_\odot$ in GW170817 [A$^+$19]. This event also revealed information on the binary tidal deformability, $\tilde{\Lambda}(\mathcal{M} = 1.186^{+0.001}_{-0.001}\mathrm{M}_\odot) = 300^{+420}_{-230}$ for low-spin priors (using a 90% highest posterior density interval). Furthermore, by assuming a linear expansion of $\Lambda(M)$, which holds fairly well for normal hadronic stars without sharp transitions, limits on the dimensionless tidal deformability of a $1.4\,\mathrm{M}_\odot$ NS were derived [A$^+$18]: $70 \leq \Lambda_{1.4} \leq 580$ for low spin priors (at 90% confidence level). This single detection of GW170817 rules out purely hadronic EOSs that are too stiff and correlated with large tidal deformabilities, as shown in fig. 4.3 (b) and (c). The stiff MS-A model by itself is incompatible with the estimated ranges of $\Lambda_{1.4}$ and $\tilde{\Lambda}$. The only solution to rescue such a stiff hadronic EOS is to introduce a phase transition at not-too-high densities, e.g., a possible smaller Λ can be achieved in a hybrid star that already exists in the pre-merger stage. For Maxwell constructions, one of the six parameter sets, $(B^{1/4}, a) = (159, 0.2)$ (blue dash-dotted) with $n_{\rm trans}/n_0 = 1.77$ (see

Table 4.5: CSS phase transition parameters [AHP13] for the stiff MS-A+vMIT/vNJL hybrid EOSs with Maxwell construction; see also fig. 4.2, panels (a)-(c). Meanings of the various entries are explained in the associated text.

$\left(\frac{B^{1/4}}{\mathrm{MeV}}, a\right)$	$\frac{n_{\mathrm{trans}}}{n_0}$	$\frac{P_{\mathrm{trans}}}{\varepsilon_{\mathrm{trans}}}$	$\frac{\Delta\varepsilon}{\varepsilon_{\mathrm{trans}}}$	c^2_{QM}	$\frac{\Delta\varepsilon_{\mathrm{crit}}}{\varepsilon_{\mathrm{trans}}}$	$M(R)$
(159, 0.2)	1.77	0.084	0.33	0.407	0.626	Connected
(162, 0.2)	2.10	0.136	0.33	0.416	0.704	Connected
(165, 0.2)	2.34	0.180	0.38	0.424	0.77	Connected
(180, 0.0)	2.04	0.127	1.13	0.326	0.691	Disconnected
(170, 0.1)	2.08	0.133	0.63	0.380	0.70	Both
(155, 0.3)	2.08	0.134	0.13	0.442	0.701	Connected
$\left(\frac{B_{\mathrm{eff}}^{1/4}}{\mathrm{MeV}}, \frac{G_v}{G_s}\right)$	$\frac{n_{\mathrm{trans}}}{n_0}$	$\frac{P_{\mathrm{trans}}}{\varepsilon_{\mathrm{trans}}}$	$\frac{\Delta\varepsilon}{\varepsilon_{\mathrm{trans}}}$	c^2_{QM}	$\frac{\Delta\varepsilon_{\mathrm{crit}}}{\varepsilon_{\mathrm{trans}}}$	$M(R)$
(295.4, 0.15)	2.91	0.284	0.594	0.236	0.926	Connected[a]

[a] This connected branch is tiny $(M_{\mathrm{max}} - M_{\mathrm{trans}}) \lesssim 10^{-3}\,\mathrm{M}_\odot$ (invisible on the magnified $M(R)$ plot; see fig. 4.4 (c)) and thus hybrid stars are undetectable.

Table 4.5) is successful to survive the LIGO constraint. Together with the maximum-mass constraint, the parameter space for sharp phase transitions is severely limited.

The panels (e)-(f) of figs. 4.2-4.3 represent results for the stiff MS-A+vMIT model with Gibbs constructions, for which the model parameters remain the same as in their Maxwell counterparts (panels (a)-(c)). The smooth feature of the Gibbs construction advances the appearance of quarks in the mixed phase to lower densities, while it defers the region of the purely quark phase to higher densities. These features are also manifested in the corresponding $\varepsilon(P)$ relation and its finite speed-of-sound behavior

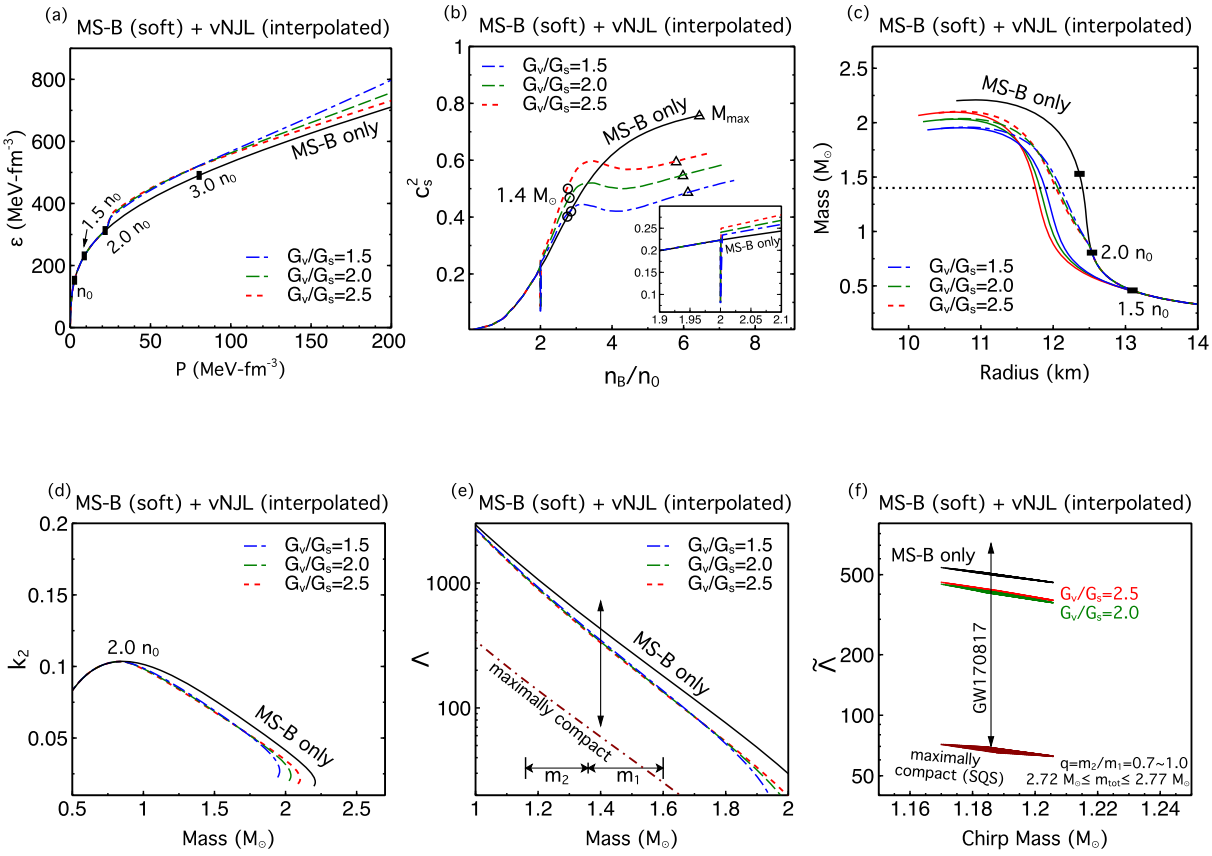

Figure 4.5: The EOS MS-B is a soft version within MS models, but can be stiffer than normal hadronic EOSs based on other models such as Skyrme or APR; MS-A is not applied here because its stiff hadronic part leads to violation of the tidal deformability constraint $\tilde{\Lambda}(\mathcal{M} = 1.186\,\mathrm{M}_\odot) \leq 720$ [A$^+$19]. In the $\tilde{\Lambda}(\mathcal{M})$ plot, only EOSs that satisfy $M_{\max} \geq 2\,\mathrm{M}_\odot$ are shown. In the interpolation picture, although the maximum mass is mostly determined by the high-density quark part and increases with its stiffness, changes in radii are flexible depending on e.g., the choice of window parameters and the low-density hadronic part (for an extensive exploration, see ref. [MHT13]). Panel (c) also shows $M(R)$ for a lower cutoff density $n_{\mathrm{trans}} = 1.5\,n_0$ (solid colored curves).

(fig. 4.2 (e) and (f)). Effectively, the softening due to the phase transition occurs earlier, smoothly decreasing the NS radii (and tidal deformabilities) for a broader range of masses which gives rise to increased compatibility with observational constraints. Three more parameter sets of the stiff MS-A+vMIT model that satisfy $M_{\max} \geq 2\,\mathrm{M}_\odot$ are all consistent with the tidal deformability constraint (fig. 4.3 (e) and (f)), in contrast to the only

candidate that qualifies in Maxwell constructions. In this respect, applying Gibbs construction is advantageous to enlarging the quark model parameter space that suitably satisfies the current constraints from observation (and also revives previously-excluded stiff hadronic models). However, the clear-cut distinction between hybrid and purely hadronic branches in terms of $M(R)$ and $\Lambda(M)$ diminishes: the drastic effect from a sharp hadron/quark transition is toned down, and thus distinguishability of quarks with regard to global observables becomes less feasible if they take the form of a mixture with hadrons. This feature accentuates the significance of dynamical properties such as NS cooling and spin-down, and the evolution of merger products.

MS-A + vNJL (stiff → soft)

In the vNJL model, pressures at $\lesssim 2\,n_0$ exhibit an unphysical behavior (being negative and/or decreasing with density) which forbids attempts to shift $n_{\rm trans}$ to low densities. If a finite vector coupling G_v is introduced, the onset of quarks is typically reached at $n_{\rm trans} \gtrsim 2.3\,n_0$ ($M_{\rm trans} \gtrsim 1.7\,{\rm M}_\odot$), leading to a short stable hybrid branch that obeys $M_{\rm max} \geq 2\,{\rm M}_\odot$ because of the stiff hadronic EOS. We display one such example in fig. 4.4 for both Maxwell and Gibbs constructions. Note that the speed of sound in the quark phase remains small, restricted by the fact that a too large G_v (correlated with stiffer QM) delays the onset significantly which yields no stable hybrid stars. Some relevant points to note are:

(i) $M_{\rm trans} \gtrsim 1.7\,{\rm M}_\odot$ indicates that most likely there will be no quarks in e.g., the component neutron stars of a binary before they coalesce. Thus, tidal properties are not shown in fig. 4.4 due to the high onset density for quarks: i.e., in this case BNS observables are irrelevant;

(ii) A small G_v has little effect on stiffening quark matter ($c^2_{\rm QM} \lesssim 1/3$), which is not desirable in terms of supporting $2\,{\rm M}_\odot$ mostly by quarks; and

(iii) Gibbs construction helps maintaining slightly more quark content than Maxwell in the most massive stars, but quarks are effectively "invisible" even if they exist.

Note that the tidal deformability constraint rules out a very stiff hadronic EOS, e.g., MS-A. This stiffness in the hadronic EOS is nevertheless a prerequisite for vNJL to construct a valid first-order transition; stable hybrid stars that are consistent with observation do not exist in this scenario. There is no solution other than an alternative treatment, such as a crossover transition to which we turn below.

Crossover transitions: Interpolatory procedures and quarkyonic matter

In obtaining the results shown below in figs. 4.5 and 4.6, we have followed the methods detailed in Sec. 4.3 for constructing crossover hadron-to-quark transitions. Although the generalization of the quarkyonic matter model to beta-equilibrated stars is presented in that section, results shown here for this case are for pure neutron matter only to provide a direct comparison with the results of ref. [MP07].

Interpolated EOSs

The results shown for this case correspond to a smooth interpolation in the window $(\bar{n}, \Gamma) = (3\,n_0, n_0)$ between the soft hadronic EOS MS-B and stiff quark EOSs in the vNJL model with $G_v/G_s = 1.5, 2.0, 2.5$. Outside this window in density, pure hadronic and pure quark phases are expected to exist. Due to the abrupt cutoff imposed in the boundary condition, there is a finite jump in c_s^2 at the lower-end of the crossover window $\bar{n} - \Gamma = 2\,n_0 \equiv n_{\rm trans}$ below which only pure hadronic phase is present. At the higher-end and above, we continue to use the interpolated form. This is different from ref. [MHT13], where the interpolated form extended to all densities. As we will see below, the cutoffs are important to typical radii and thus could be significant.

Effects of introducing quarks above $n_{\rm trans} = 2\,n_0$ through smooth interpolations in the EOS are shown in fig. 4.5 (a)-(c). The maximum mass is primarily determined by the

stiffness above $4\,n_0$, hence the use of large vector-coupling strengths in vNJL. Consequently, one can derive a constraint on G_v/G_s from $M_{\rm max} \geq 2\,{\rm M}_\odot$ if other parameters are fixed, e.g., $G_v/G_s = 1.5$ is probably ruled out. On the other hand, typical radii for $1.0 - 1.6\,{\rm M}_\odot$ stars are sensitive to the stiffness in the hadronic phase for $n_{\rm B} \lesssim 2\,n_0$, as well as to the choice of the threshold density. For instance, we have found that for $n_{\rm trans} = 1.5\,n_0$ instead of $2\,n_0$, $R_{1.4}$ decreases by about 0.3 km. If, however, a stiff hadronic matter EOS such as MS-A in Sec. 4.3 is applied, the resulting radius and tidal deformability are too large and violates the condition $\tilde{\Lambda}(\mathcal{M} = 1.186\,{\rm M}_\odot) \leq 720$ [A$^+$19].

As can be seen from fig. 4.5 (d)-(f), the softer MS-B EOS is by itself compatible with the current constraint on the binary tidal deformability. Implementing the crossover region through interpolation further enhances the compatibility. Better measurements of $\tilde{\Lambda}(\mathcal{M})$ from multiple merger detections in the future might help in limiting the relevant interpolation parameters. Recall that such "soft HM $\rightarrow$ stiff QM" combination is usually forbidden in a first-order transition, given the absence of an intersection in the P-μ plane between pure hadronic and pure quark phases.

Quarkyonic matter

In this case, we present results obtained by using the hadronic EOSs MS-B/C for pure neutron matter and two-flavor quark EOSs with and without interactions between quarks when they appear. The main reason for the rapid increase in pressure at supra-nuclear densities and the attendant behavior of c_s^2 vs $n_{\rm B}$ is also elucidated in more detail than was done in ref. [MP07].

In the quarkyonic picture, both the maximum mass and typical radii are larger than those obtained by EOSs with neutrons only. In fact, some EOSs that are too soft to survive the $M_{\rm max} \geq 2\,{\rm M}_\odot$ constraint can be rescued by the boost in stiffness once quarkyonic matter appears; see e.g., MS-C (PNM) in fig. 4.6 (a)-(c). However, for a stiff neutrons-only EOS, if a transition into quarkyonic matter takes place, compatibility with

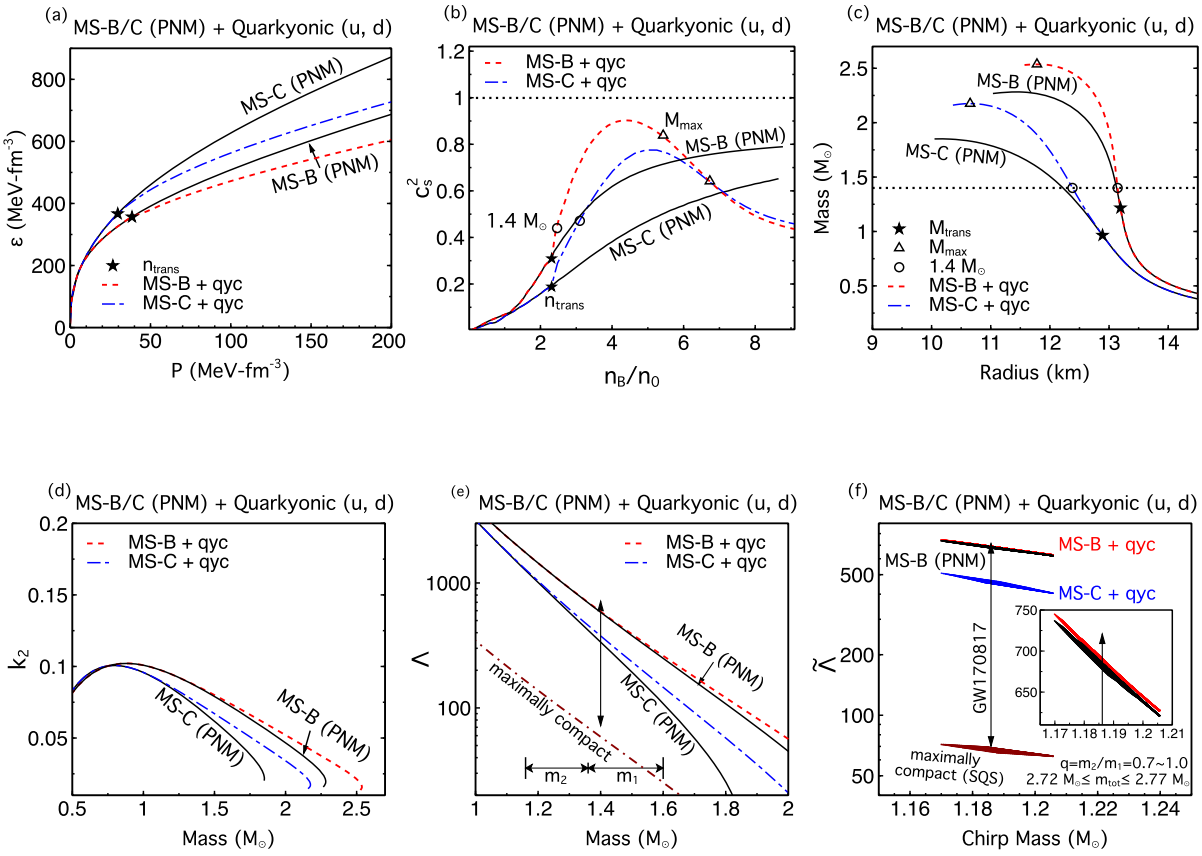

Figure 4.6: The EOS MS-C is an example of even softer EOSs within the same model that cannot support $2\,M_\odot$ stars by themselves; MS-A is not applied here because its stiff hadronic part leads to violation of the tidal deformability constraint $\tilde{\Lambda}(\mathcal{M} = 1.186\,M_\odot) \leq 720$ [A$^+$19]. In the two-flavor quarkyonic picture, switching to the smooth crossover region increases both the maximum masses and typical radii (hence the tidal deformabilities). Note that here quark masses are dynamically generated here with vNJL ($G_v/G_s = 0.5$) instead of the original assumption that $M_q = M_n/3$ as in the Fermi gas model of ref. [MP07]. In the $\tilde{\Lambda}(\mathcal{M})$ plot, only EOSs that satisfy $M_{\rm max} \geq 2\,M_\odot$ are shown.

binary tidal deformability constraint from GW170817 becomes reduced, because of the tendency to increase R and therefore Λ. These increases put the model at more risk of breaking the upper limit on Λ. This is evident in fig. 4.6 (d)-(f), where the MS-B (PNM) EOS is at the edge of exclusion and with quarkyonic matter the situation is slightly worse.

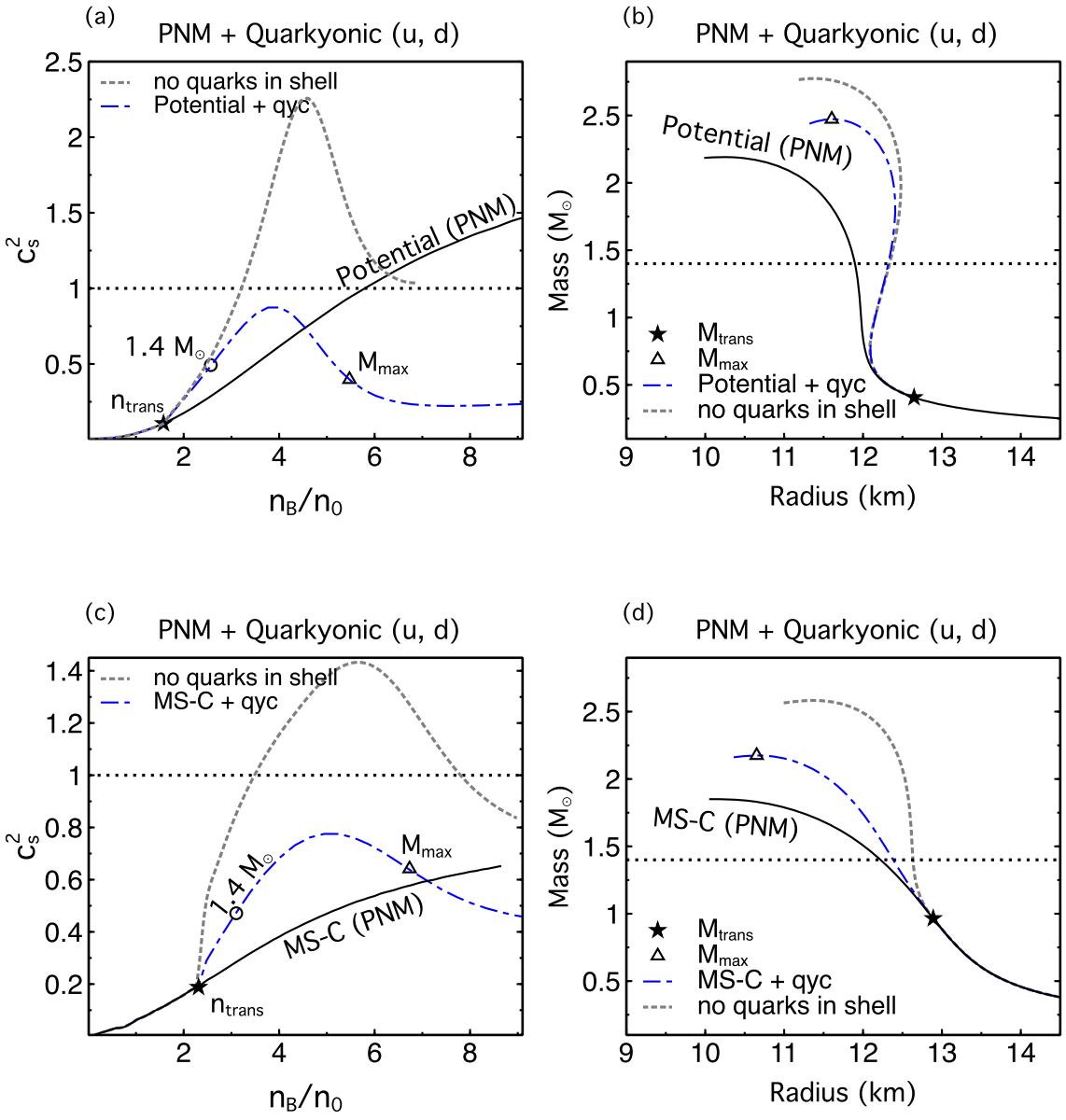

Figure 4.7: In panels (a) and (c), the squared speed of sound vs baryon density in PNM for the EOS models of ref. [MP07] and MS-C (PNM) of this work. The right panels (b) and (d) show the corresponding *M*-*R* curves. The different curves illuminate the influence of the shell on the results.

An examination of the behavior of c_s^2 vs $n_{\rm B}$ with and without quarks offers insights into the role played the presence of the shell for $k_{Fn} > \Delta$ in the quarkyonic model. fig. 4.7 shows results of c_s^2 for the cases in which there is no shell (i.e., neutrons only throughout

the star), neutrons only below and above Δ, and with the inclusion of quarks for $k_{Fn} > \Delta$. The results in this figure correspond to the neutron matter EOSs used in ref. [MP07] and the MS-C+vNJL model of this work with G_v/G_s. For the former EOS, values of $\Lambda_Q = 420$ MeV and $\kappa = 1$ were used to calculate the shell width Δ. The onset of quarks in this case occurs at $n_{\rm trans} = 0.37$ fm^{-3}. This is to be compared with $n_{\rm trans} = 0.24$ fm^{-3} with $\Lambda_Q = 380$ MeV and $\kappa = 0.3$ in the EOS of ref. [MP07]. For the two-flavor vNJL model used in this connection, values of the parameters used were $\Lambda = 631.4$ MeV, $G_s\Lambda^2 = 1.835$ and $G_v/G_s = 0.5$ as in ref. [HK94].

The main differences between the models in ref. [MP07] and this work are:
(i) For pure neutron matter (no quarks), the EOS of ref. [MP07] becomes acausal for $n_{\rm B}/n_0 \simeq 6$ owing to the term proportional to n_n^3 in its interacting part. As the central density of the star is $\simeq 6.74\, n_0$, this feature may be of some concern. However, the MS-B/C+vNJL models - being relativistically covariant - remain causal for all densities, and
(ii) Interactions between quarks are not included in the EOS of ref. [MP07] except in the kinetic energy term with the use of $M_q = M_n/3$, whereas the MS-B/C+vNJL model uses density-dependent dynamically generated u, d quark masses that steadily decrease with increasing density from their vacuum values of $\simeq M_n/3$. In addition, repulsive vector interactions between quarks were used in the vNJL models.

The above differences notwithstanding, the inner workings of the quarkyonic model - particularly, the influence of quarks - are apparent from fig. 4.7 (a) and (c). Without the presence of quarks in the shell, the EOSs in both models are very stiff even to the point of being substantially acausal. The presence of quarks in the shell abates this undesirable behavior by softening the overall EOS (dash-dotted blue curves) relative to the case when only nucleons are present (dotted gray curves). With progressively increasing density, the density of nucleons is depleted within the shell whereas that of the quarks becomes

predominant. As $c_s^2 \to 1/3$ for quarks at asymptotically high densities, it exhibits a maximum (as well as a minimum) at some intermediate density. Note, however, that compared to the neutron-matter only case everywhere (black solid curves), the overall EOS of the quarkyonic matter is stiffer within the central densities of the corresponding stars.

Insofar as c_s^2 is a measure of the stiffness of the EOS, the M-R curves shown in fig. 4.7 (b) and (d) reflect the behavior of the corresponding c_s^2 vs $n_{\rm B}$. The presence of quarkyonic matter (dash-dotted blue curve) causes an increase in the $M_{\rm max}$ for both models. If only the neutron content of quarkyonic matter is considered (dotted gray curve), then the increase in $M_{\rm max}$ is more substantial. Similarly, the radii of both the maximum mass and $1.4\,{\rm M}_\odot$ stars are significantly larger in quarkyonic matter. Quantitative differences between the two cases can be attributed to the presence of interactions between quarks in the MS-B+vNJL model.

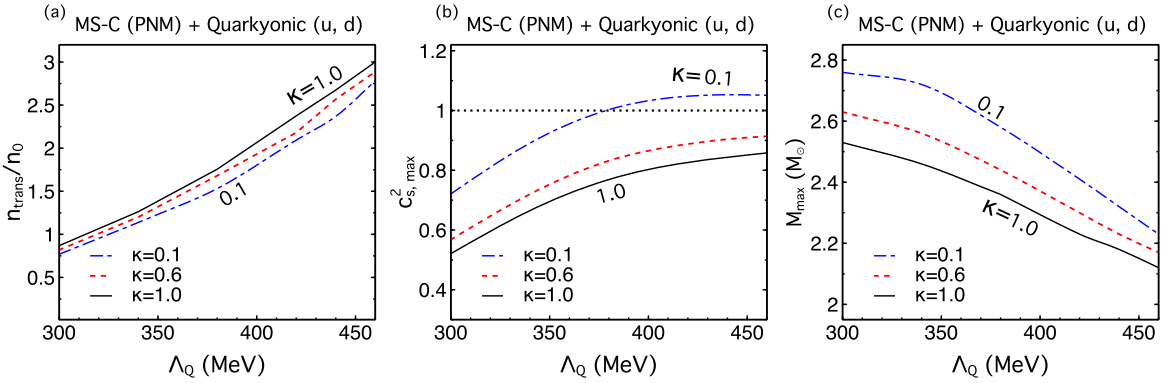

Figure 4.8: Variation of the hadron-to-quark transition density (in units of n_0), the squared speed of sound and the maximum mass as functions of the parameters Λ_Q and κ that determine the shell width Δ.

The hadron-to-quark transition density $n_{\rm trans}$, the peak value of the squared speed of sound $c^2_{s,\rm max}$, and the maximum mass $M_{\rm max}$ all depend on the choice of Λ_Q and κ used to calculate the shell width Δ. fig. 4.8 shows the variation of these quantities as a function of

Λ_Q for values $\kappa = 0.1, 0.6$ and 1 for the MS-C+vNJL model chosen here. Intermediate values of κ lead to results that lie within the boundaries shown in this figure. Note that high values of both Λ_Q and κ are required to ensure that $n_{\rm trans} \gtrsim 1.5\, n_0$ and $c_s^2 < 1$. This requirement, however, decreases $M_{\rm max}$ but masses above the current constraint of $\gtrsim 2\,{\rm M}_\odot$ can be still obtained. In the absence of interactions between quarks, as in ref. [MP07], the window of Λ_Q and κ values that are usable is very small. We stress, however, that the optimum choice of these parameters is model dependent in that if a different hadronic or quark EOS is used, the values of Λ_Q and κ can change.

Table 4.6: Summary of different treatments with the introduction of quarks in the dense matter EOS. For a sharp first-order transition with Maxwell construction, the most readily compatible scenario is stiff hadronic matter undergoes phase transition into stiff ($c^2_{\rm QM} \gtrsim 0.4$) quark matter. For a crossover transition, soft HM $\rightarrow$ stiff QM is necessary.

HM $\rightarrow$ QM	First-order Transition (Maxwell)[a]	Crossover Transition
stiff to soft	✗ vMIT: cannot support $M_{\rm max} \geq 2\,{\rm M}_\odot$ ✗ vNJL: $M_{\rm trans} \gtrsim 1.7\,{\rm M}_\odot$, $\tilde{\Lambda}(\mathcal{M} = 1.186\,{\rm M}_\odot) > 720$	✗ unphysical decreasing function of $P(n_{\rm B})$
soft to stiff	✗ no intersection for $P(\mu)$[b]	✓ interpolation: $M_{\rm trans} \lesssim 1.0\,{\rm M}_\odot$, $R_{1.4} < 13\,{\rm km}$ ✓ quarkyonic: $M_{\rm max} \geq 2\,{\rm M}_\odot$; $R_{1.4}$ and $M_{\rm trans}$ vary
soft to soft	✗ cannot support $M_{\rm max} \geq 2\,{\rm M}_\odot$	✗ cannot support $M_{\rm max} \geq 2\,{\rm M}_\odot$
stiff to stiff	✓ vMIT: $M_{\rm max} \geq 2\,{\rm M}_\odot$; $R_{1.4}$ and $M_{\rm trans}$ vary ✗ vNJL: onset for quarks too high; immediately destabilize	✗ $\tilde{\Lambda}(\mathcal{M} = 1.186\,{\rm M}_\odot) > 720$, $R_{1.4} > 13\,{\rm km}$

[a] See text for details if the Gibbs construction is applied. Gibbs construction satisfies many observational constraints such as $R_{1.4}$ and $M_{\rm max}$ due to the earlier onset of quarks. However, distinguishability from purely hadronic stars is lost.

[b] Limited by the specific quark models applied here; in a generic parametrization (e.g. CSS) the soft HM $\rightarrow$ stiff QM is possible.

On a physical level, low values of Λ_Q and κ lead to a substantial quark content in the star, but at the expense of $n_{\rm trans} \rightarrow n_0$ – a disturbing trend. Although quarks soften the overall EOS, the presence of the shell and the redistribution of baryon number between

nucleons and quarks causes a substantial stiffening of the overall EOS which in turn leads to very high values of $M_{\rm max}$. Conversely, very high values of Λ_Q and κ decrease the quark content which makes the overall EOS to be nearly that without quarks. This feature is generic to the quarkyonic model, which enables it to achieve maximum values consistent with the observational mass limit even when the EOS with hadrons only fails to meet this constraint.

The low transition densities and the extreme stiffening of the EOS caused by the shell in quarkyonic matter bear further investigation. Although inspired by QCD and large N_c physics, the width of the shell is independent of the EOSs in the both hadronic and quark sectors, at least in the initial stage of the development of the model. The energy cost in creating such a shell in dense matter is another issue that warrants scrutiny.

4.5 Conclusion and Outlook

In this work, we have performed a detailed comparison of first-order phase transition and crossover treatments of the hadron-to-quark transition in neutron stars. For first-order transitions, results of both Maxwell and Gibbs constructions were examined. Also studied were interpolatory schemes and the second-order phase transition in quarkyonic matter, which fall in the class of crossover transitions. In both cases, sensitivity of the structural properties of neutron stars to variations in the EOSs in the hadronic as well as in the quark sectors were explored. The ensuing results were then tested for compatibility with the strict constraints imposed by the precise measurements of $2\,\mathrm{M}_\odot$ neutron stars, the available limits on the tidal deformations of neutron stars in the binary merger GW170817 and the radius estimates of $1.4\,\mathrm{M}_\odot$ stars inferred from x-ray observations. These independent constraints from observations are significant in that the lower limit on the maximum mass reflects the behavior of the dense matter EOS for densities $\gtrsim 4\,n_0$, whereas bounds on binary tidal deformability $\tilde{\Lambda}$ and estimates of $R_{1.4}$ depend on the EOS

for densities $\gtrsim 2-3\,n_0$, respectively. Table 4.6 provides a summary of the generic outcomes of our study.

If the hadron-to-quark transition is strongly first-order, as is the case for standard quark models such as vMIT and vNJL that we used, then the hadronic part needs to be relatively stiff to guarantee a proper intersection in the P-μ plane. For a hadronic EOS as stiff as MS-A, this combination brings tension with $\Lambda_{1.4}$ or $R_{1.4}$ estimates. Concomitantly, a too-high transition density that yields $M_{\rm trans} \gtrsim 1.7\,\mathrm{M}_\odot$ results in either very small quark cores or completely unstable stars that are indistinguishable from those resulting from a stiff purely hadronic EOS. Thus, such hybrid EoSs can easily be ruled out. This is typical for NJL-type models; see, e.g., fig. 4.4. In contrast, lower transition densities (that yield $M_{\rm trans} \lesssim 1.0-1.6\,\mathrm{M}_\odot$) are capable of decreasing radii. If accompanied by a stiff quark matter EOS with sizable repulsive interactions, these hybrid EOSs produce $M_{\rm max} \geq 2\,\mathrm{M}_\odot$. figs. 4.2 and 4.3 show examples in which the vMIT model was used with Maxwell/Gibbs constructions.

Our analysis indicates that use of the Gibbs construction is beneficial in satisfying the current constraints from observation for many stiff hadronic EOSs as it enlarges the parameter space of quark models. As similar $M(R)$ and $\Lambda(M)$ relations for hybrid and purely hadronic stars can be obtained, the distinction between the two is, however, lost. This feature underscores the significance of dynamical properties such as neutron star cooling and spin-down, and the evolution of merger products.

To sum up the part about first-order phase transitions, current observational constraints disfavor weakly-interacting quarks at the densities reached in neutron star cores. Should a first-order transition into strongly-interacting quark matter (as described by the vMIT bag model or vNJL-type models) take place, the onset density is likely of relevance also to canonical neutron star masses in the range $1.0-1.6\,\mathrm{M}_\odot$.

One should keep in mind, however, that perturbative approaches to the quark matter EOS are not expected to hold in the density range $\approx 2 - 4\, n_0$. This limitation brings the validity of first-order phase transitions caused by such EOSs into question. In this regard, model-independent parameterizations circumvent the issue and have the advantage of translating observational constraints more generically. For instance, specific QM models prohibit the transition into soft hadronic matter, but in the CSS parameterization this restriction disappears and a much larger parameter space can be explored including soft HM $\rightarrow$ stiff QM [HS19]. However, such parameterizations lack a physical basis and beg for the invention of a non-perturbative approach.

If the hadron-to-quark transition is a smooth crossover, as in the case of interpolatory schemes and in quarkyonic matter, the pressure in the transition region is stiffened unlike the sudden softening of pressure caused by a first-order transition. This stiffening is also reflected in a local peak in the sound velocity before the pure quark phase is entered. This stiffening is responsible for supporting massive stars that are compatible with the current lower limit of $2\,\mathrm{M}_\odot$.

It is also common that the onset density for quarks is somewhat low ($M_{\mathrm{trans}} \lesssim 1.0 - 1.6\,\mathrm{M}_\odot$) in these crossover approaches. This feature implies that all neutron stars we observe should contain some quarks admixed with hadrons. We find that at low densities soft hadronic EOSs are necessary, but above the transition changes in radii rely heavily on the methods of implementing the crossover in both the interpolation approach and in quarkyonic matter. Consequently, it is difficult to obtain physical constraints on the crossover EOSs from a better determination of the radius, e.g., $R_{1.4}$, or improved tidal deformability measurements. It is promising, however, in limiting parameters, e.g., the vector coupling strength G_v/G_s in vNJL or κ and Λ in the quarkyonic model, pertinent to the required stiffening to satisfy the limits imposed by mass measurements of heavy neutron stars.

Regardless of the phase transition being first-order or crossover, our results suggest that quarks likely exist in the pre-merger component neutron stars of GW170817. If quarks only appear after the merger (before the remnant collapsing into a black hole), there is a valid soft HM $\rightarrow$ stiff QM first-order transition that cannot be captured by the vMIT bag or vNJL models. Numerical simulations that involve quarks [MPD$^+$19, BBB$^+$19] will assist in identifying them during post-merger gravitational-wave evolution. Better understanding and progress in theory, experiments and observations are required to clarify the situation.

Although the presence of quarks in neutron stars is not ruled out by currently available constraints, it is nearly impossible to confirm it even with improved determinations of radii from x-ray observations and tidal deformabilities from gravitational wave detections. Similarly, it will be difficult to identify the nature of the phase transition on the basis of M and R observations only, unless there is a sufficiently strong first-order transition that gives rise to separate branches of twin stars with discontinuous M-R and/or $\tilde{\Lambda}$-$\mathcal{M}$ relations. Dynamical observables such as thermal/spin evolution, global oscillation modes, continuous gravitational waves etc. that are sensitive to transport properties would potentially provide more distinct signatures of exotic matter in neutron stars. In future work, it is worthwhile to achieve consistency with dynamical observables, particularly for the crossover scenarios of the transition to quark matter.

Acknowledgements

We thank Larry McLerran and Sanjay Reddy for helpful discussions relating to quarkyonic matter. This work was performed with research support from the National Science Foundation Grant PHY-1630782 and the Heising-Simons Foundation Grant 2017-228 for S.H., the U.S. Department of Energy Grant No. DE-FG02-93ER-40756 for

M.A.A.M., S.L. and M.P. The research of C.C. is supported by the National Science Foundation Grant PHY-1748621.

Appendix

Thermodynamics of nucleons in the shell of quarkyonic matter

In this Appendix, we provide some details of the evaluation of the kinetic parts of the energy density, chemical potential and energy density and pressure for nucleons in the shell. The expressions we obtain will then be used to establishing the thermodynamic identity (TI) in the presence of a shell. For the evaluation of these quantities the relation

$$\begin{aligned}\frac{d}{d\alpha}\int_{\phi_1(\alpha)}^{\phi_2(\alpha)} F(x,\alpha)\,dx &= \int_{\phi_1(\alpha)}^{\phi_2(\alpha)} \frac{\partial F(x,\alpha)}{\partial\alpha}\,dx \\ &+ F(\phi_2,\alpha)\frac{\partial\phi_2}{\partial\alpha} - F(\phi_1,\alpha)\frac{\partial\phi_1}{\partial\alpha}\,,\end{aligned} \tag{4.30}$$

where α is a parameter in the functions ϕ_1, ϕ_2 and F will be useful.

Energy density

The kinetic energy density of nucleons, neutrons to be specific, in the shell is

$$\begin{aligned}\varepsilon_n^{(\mathrm{kin})} &= \frac{1}{\pi^2}\left(\int_0^{k_{Fn}} - \int_0^{k_{Fn}-\Delta}\right) dk\,k^2\sqrt{k^2+M_n^2}\,, \\ &= F_1(k_{Fn}) - F_2(k_{Fn}-\Delta)\,,\end{aligned} \tag{4.31}$$

where $\Delta = \Lambda_Q^3/k_{Fn}^2 + \kappa\Lambda_Q/N_c^2$. In analytical form,

$$\varepsilon_n^{(\mathrm{kin})} = \frac{1}{4\pi^2}\left[k^3 e_k + \frac{M_n^2}{2}k e_k - \frac{M_n^4}{2}\ln(k+e_k)\right]_L^U\,. \tag{4.32}$$

For $k_{Fn} < \Delta$, the upper limit $U = k_{Fn}$, the lower limit $L = 0$ and $e_k = \sqrt{k^2+M_n^2}$, which leads to the familiar expression for spin-$\frac{1}{2}$ relativistic particles of mass M_n. For neutrons in the shell with $k_{Fn} > \Delta$, however, $U = k_{Fn}$ and $L = (k_{Fn}-\Delta)$ with $e_k = \sqrt{(k-\Delta)^2+M_n^2}$.

Chemical potential

The associated chemical potential ensues from

$$\begin{aligned} \mu_n^{(\mathrm{kin})} &= \frac{d\varepsilon_n^{(\mathrm{kin})}}{dk_{Fn}} \frac{dk_{Fn}}{dn_n} \\ &= \left(\frac{dF_1}{dk_{Fn}} - \frac{dF_2}{dk_{Fn}} \right) \frac{dk_{Fn}}{dn_n} \,. \end{aligned} \tag{4.33}$$

For the neutrons in the shell,

$$\begin{aligned} n_n &= \frac{1}{3\pi^2} \left[k_{Fn}^3 - (k_{Fn} - \Delta)^3 \right] , \\ \frac{dn_n}{dk_{Fn}} &= \frac{1}{\pi^2} \left[k_{Fn}^2 - (k_{Fn} - \Delta)^2 \left(1 - \frac{\partial \Delta}{\partial k_{Fn}} \right) \right] \\ &= \frac{1}{\pi^2} \left[k_{Fn}^2 - (k_{Fn} - \Delta)^2 \left(1 + \frac{2\Lambda_Q^3}{k_{Fn}^3} \right) \right] . \end{aligned} \tag{4.34}$$

For evaluating dF_1/dk_{Fn}, use of the relations

$$\begin{aligned} \phi_1(k_{Fn}) &= 0, \;\; \phi_2(k_{Fn}) = k_{Fn} \\ \frac{\partial \phi_1}{\partial k_{Fn}} &= 0 \,, \;\; \frac{\partial \phi_2}{\partial k_{Fn}} = 1 \end{aligned} \tag{4.35}$$

in eq. (4.30) yields

$$\frac{dF_1}{dk_{Fn}} = \frac{1}{\pi^2} k_{Fn}^2 \sqrt{k_{Fn}^2 + M_n^2} \,. \tag{4.36}$$

The evaluation of dF_2/dk_{Fn} proceeds along similar lines, but with

$$\begin{aligned} \phi_1(k_{Fn}) &= 0, \;\; \phi_2(k_{Fn}) = k_{Fn} - \Delta \\ \frac{\partial \phi_1}{\partial k_{Fn}} &= 0 \,, \;\; \frac{\partial \phi_2}{\partial k_{Fn}} = 1 - \frac{\partial \Delta}{\partial k_{Fn}} \end{aligned} \tag{4.37}$$

with the result

$$\frac{dF_2}{dk_{Fn}} = \frac{1}{\pi^2} (k_{Fn} - \Delta)^2 \sqrt{(k_{Fn} - \Delta)^2 + M_n^2} \left(1 + \frac{2\Lambda_Q^3}{k_{Fn}^3} \right) \tag{4.38}$$

Putting these results together, we obtain after some simplification

$$\begin{aligned}\mu_n^{(\mathrm{kin})} &= \frac{\sqrt{k_{Fn}^2+M_n^2}-\mathcal{R}\sqrt{(k_{Fn}-\Delta)^2+M_n^2}}{1-\mathcal{R}} \\ \mathcal{R} &= \left(1-\frac{\Delta}{k_{Fn}}\right)^2\left(1+\frac{2\Lambda_Q^3}{k_{Fn}^3}\right).\end{aligned} \tag{4.39}$$

Pressure

The kinetic theory expression for a single species of spin-$\frac{1}{2}$ fermions is

$$P = 2\,T\int_L^U \frac{d^3k}{(2\pi)^3}\ln[1+e^{(\mu-e)\beta}]\,, \tag{4.40}$$

where $\beta = 1/T$, e is the single particle spectrum and μ the chemical potential. A partial integration on the right hand side yields

$$P = T\left[\frac{1}{3\pi^2}k^3\ln[1+e^{(\mu-e)\beta}]\right]_L^U + \frac{1}{3}\,2\int_L^U \frac{d^3k}{(2\pi)^3}\,k\frac{de_k}{dk}\frac{1}{1+e^{(\mu-e)\beta}}\,. \tag{4.41}$$

At finite T, the first term vanishes when $U=\infty$ and $L=0$ leaving the second term as the kinetic pressure. For $T\to 0$, and finite L and U, however, we have

$$P = \frac{1}{3\pi^2}\left[k^3(\mu-e)\right]_L^U + \frac{1}{3}\,2\int_L^U \frac{d^3k}{(2\pi)^3}\,k\frac{de_k}{dk}\,. \tag{4.42}$$

The expressions for $P_n^{(\mathrm{kin})}$, thus take different forms in the regions $k_{Fn}<\Delta$ and $k_{Fn}>\Delta$. For $k_{Fn}<\Delta$, the limits $U=k_{Fn}$ and $L=0$ yield the familiar kinetic theory expression

$$\begin{aligned}P_n^{(\mathrm{kin})} &= \frac{1}{3}\,2\int_L^U \frac{d^3k}{(2\pi)^3}\,k\frac{de_k}{dk} \\ &= \frac{1}{12\pi^2}\left[k^3e_k-\frac{3}{2}M_n^2ke_k+\frac{3}{2}M_n^4\ln(k+e_k)\right]_L^U,\end{aligned} \tag{4.43}$$

where $e_k = \sqrt{k^2+M_n^2}$. The last two terms in eqs. (4.32) and (4.43) cancel, and thus in this region, $\varepsilon_n^{(\mathrm{kin})}+P_n^{(\mathrm{kin})} = n_n\mu_n^{\mathrm{kin}}$ (the TI) with $n_n = k_{Fn}^3/(3\pi^2)$ and $\mu_n^{(\mathrm{kin})} = \sqrt{k_{Fn}^2+M_n^2}$.

In the region $k_{Fn} > \Delta$ with $U = k_{Fn}$ and $L = (k_{Fn} - \Delta)$, the kinetic theory pressure becomes

$$P_n^{(\mathrm{kin})} = \frac{1}{3\pi^2}\left[k^3(\mu_n^{\mathrm{kin}} - e_k)\right]_L^U + \frac{1}{3}\,2\int_L^U \frac{d^3k}{(2\pi)^3}\,k\frac{de_k}{dk}\,. \tag{4.44}$$

The first term above gives the contribution from the boundaries of the shell. Inserting the appropriate limits for the shell, this term reads as

$$\frac{1}{3\pi^2}\Big[\mu_n\left(k_{Fn}^3 - (k_{Fn}-\Delta)^3\right) - \left(k_{Fn}^3\sqrt{k_{Fn}^2 + M_n^2} - (k_{Fn}-\Delta)^3\,\sqrt{(k_{Fn}-\Delta)^2 + M_n^2}\right)\Big]. \tag{4.45}$$

Thermodynamic identity

Collecting the results in eqs. (4.44) and (4.45) and evaluating $\varepsilon_n^{(\mathrm{kin})}$ in Eq. (4.32) for the shell, we obtain the TI (after many cancellations)

$$\begin{aligned} \varepsilon_n^{(\mathrm{kin})} + P_n^{(\mathrm{kin})} &= n_n\mu_n^{\mathrm{kin}} \quad \text{with} \\ n_n &= \frac{1}{3\pi^2}\left[k_{Fn}^3 - (k_{Fn}-\Delta)^3\right], \end{aligned} \tag{4.46}$$

the last relation giving the number density of neutrons in the shell. The neutron chemical μ_n^{kin} here is independently calculated from Eq. (4.39). We have verified that numerical calculations of $\mu_n^{\mathrm{kin}} = d\varepsilon_n^{(\mathrm{kin})}/dn_n$ and $P_n^{(\mathrm{kin})} = n_n^2 d(\varepsilon_n^{(\mathrm{kin})}/n_n)/dn_n$ in the shell yield the same results as evaluations from the analytical formulas above which provide additional physical insight concerning the role played by the shell.

All expressions in this appendix apply also to protons so that a generalization to a 2-component system consisting of neutrons and protons is straightforward.

4.6 Specific Contributions of the Author

The work documented in this chapter has been largely derived from the paper, “Treating quarks within neutron stars” which has been the effort of a team including

myself (Sudhanva Lalit), Md. Abdullah Al Mamun and Drs. Sophia Han, Constantinos Constantinou and Madappa Prakash. The project of constructing "Treating quarks within neutron stars" using multiple species was conceived by my advisor Dr. Madappa Prakash. The completion of this project involved significant new developments in both theoretical formalisms and numerical techniques. All analytic equations used in this chapter were independently derived by me and crosschecked with those derived by other members of the team. The FORTRAN codes written to produce the results presented in this chapter were written solely by me and the ensuing results were crosschecked by others with results from their own codes. The writing of this paper was a team effort with the work being divided such that each member wrote the first draft of a given section, then passed it to another member to be augmented and improved. The process of passing the work between the team members was iterated until all members agreed on the final version. For the first draft, my focus was on the sections containing equation of state models and results, but I was actively involved in developing each section during the iteration process.

5 Outlook

The original research reported in this dissertation is concerned with microphysical aspects of hot and dense matter encountered in astrophysical situations such as core-collapse supernovae, neutron stars and their mergers. The final sections of the published papers reproduced in this thesis contain the findings and conclusions. Rather than repeating them here, I will outline the future projects suggested by those investigation in what follows.

5.1 Applications of Next-To-Leading Order Fermi Liquid Theory

The advantage of Fermi Liquid Theory and its next-to-leading order extension is that the thermal properties of interacting fermions can be calculated for entropies per baryon up to 2 down to subnuclear densities from the zero-temperature single-particle energy spectrum. As the Landau effective mass function and its derivatives are easily calculated from the zero-temperature single-particle energy spectrum, application of this technique to microscopic models in which calculations are either cumbersome or too time-consuming is straightforward. Examples include Monte Carlo calculations in which finite temperature calculations are beset with the fermion sign problem and effective field theories in which such calculations are somewhat cumbersome. We are forging collaborations in this regard and will report results when they become available.

5.2 Subnuclear Density Equation of State with Multiple Clusters

In simulations of binary neutron star mergers, the dense matter equation of state (EOS) is required over wide ranges of density and temperature as well as under conditions in which neutrinos are trapped, and the effects of magnetic fields and rotation prevail. In the subnuclear region ($n_B \leq 0.1\text{fm}^{-3}$), nucleons coexist with light ($A \leq 4$) and heavy ($A > 4$) nuclei as well as other nonshperical nucleonic configurations, known as the pasta

phase. For a sufficiently dilute and/or hot system, heavy nuclei and pasta are absent because their formation and longevity are inhibited by the effects of low density and high temperature. Thus, there exists a range of (n_B, Y_l, T), where Y_l is the lepton fraction, in which only nucleons and light nuclear clusters, survive. In chapter 3 we assessed the status of dense matter theory and pointed out the successes and limitations of approaches currently in use. A comparative study of the excluded volume (EV) approach of Lattimer et al.[LS91, LLPR85] and virial approach [HS06] for the $np\alpha$ system using the equation of state of Akmal, Pandharipande and Ravenhall (APR)[APR98] for interacting nucleons was presented in the sub-nuclear density regime. Owing to the excluded volume of the α-particles, their mass fraction vanishes in the EV approach below the baryon density 0.1 fm^{-3}, whereas it continues to rise due to the predominantly attractive interactions in the virial approach. The EV approach was extended to include clusters of light nuclei such as d, ^{3}H and ^{3}He in addition to α-particles. Results of the relevant state variables from this development were presented which enabled comparisons with related but slightly different approaches in the literature.

The potential model approach

The EV approach mentioned above accounts for hard-core repulsive interactions between nucleons and nuclei which become significant as the density increases but ignores attractive interactions which are known to be present from phase shift data. As a consequence of the hard-core repulsion, the light nuclear species disappear at varying densities below 0.1 fm^{-3}. On the other hand, the virial approach uses the available phase shift data as input and as a result, includes both attractive and repulsive interactions. However, due to the lack of phase shift data at high-enough energies to probe the nuclear hard core, interactions, as included in this approach, are predominantly attractive. Consequently, the mass fractions of light nuclei continue to increase beyond the nuclear

saturation density n_s in the regions of (n_B, Y_l, T) where they should be absent. Furthermore, the virial approach is valid only when the fugacities $z = \exp(\mu/T)$ of the various constituents are less than unity which is not always the case for nucleons.

From a theoretical standpoint, the region with light nuclear clusters presents the situation of fermion-boson mixtures which is an active area of research in the context of cold atoms[PS08]. The development of a method based on the HF approximation from which the single-particle spectra of the participants (all of which are treated as point-particles) can be extracted using experimentally-fitted, two-particle, position-space potentials is currently underway. For the nucleon-light nucleus system, such an approach has not been used so far in the literature. Preliminary calculations indicate that the limitations of the EV and virial approaches can be overcome. A follow up to this project will be the calculation of the EOS in this region based on fermion-boson potentials derived from effective field theory[PS08].

5.3 Beyond Mean Field Theory

In the long-wavelength limit, $\lambda k_F > 1$, where λ is the wavelength of oscillations of the meson fields and k_F the baryon Fermi momentum, fluctuations of the meson fields mediating interactions between the fermions become important. In this region, meson oscillations couple strongly to macroscopic baryon density fluctuations, and can no longer be described within the framework of mean field theory (MFT). They are, instead, genuine many-body effects, more appropriately identified as collective modes and can be obtained by solving an eigenvalue equation involving the polarization tensor $\Pi_{\mu\nu}$. The poles of the meson propagator can be calculated by summing the set of ring diagrams which consist of repeated insertions of the lowest-order polarization part. The same eigenvalue equation can be derived from the requirement that the 4-current density fluctuation $\delta J_\mu(q)$ is self-consistently sustained.

Extensive studies of collective modes have been made for (i) the dense electron gas (see, e.g., [BS10], and references therein) in which long-range interactions occur through the exchange of massless photons and (ii) nuclear systems in which short-range interactions are mediated by the exchange of massive bosons, but only in the asymptotically high density limit, at zero temperature and for isospin-symmetric matter (ref. [Chi77], and references therein). In both cases, point-particle field theory was used.

The above observations suggest several avenues for further investigation beyond MFT which are listed below.

1. For densities of relevance to astrophysical applications, an examination of the ring energy contributions (the dominant part of the so-called correlation energy in many-body perturbation theory) at near nuclear and slightly above densities, resulting from massive bosons, is required. This task will likely involve extensive numerical studies with analytical checks in various limiting situations (low and high densities, massless bosons).

2. In nuclear systems with unequal numbers of neutrons and protons commonly encountered in astrophysical settings, the contributions from pseudo-scalar (π-meson) and iso-vector (ρ-meson) exchanges in addition the vector (ω-meson) and scalar (σ-meson) ones are needed. These contributions have not been considered in the literature, and can be calculated in both non-relativistic and relativistic field-theoretical approaches. Of particular interest here is the density dependence of the symmetry energy which determines the radius of a neutron star and whether neutrino emission via the rapid direct Urca process [LPPH91b] occurs or not.

3. The above studies for the ground state energy can then be extended to finite temperatures of relevance to astrophysical applications.

4. Attempts to go beyond point-particle field theory can also be made following ref. [PEK92] in which form-factors at each vertex of interaction were used to account for the finite size of nucleons. This procedure may likely avoid the divergent nature of density-dependent coupling constants inherited in evaluating contributions from correlation energies at very high densities in point-particle field theory. This work will also involve extensive numerical studies and analytical checks wherever possible.

5. The extent to which collective effects influence astrophysical phenomena can be studied using the simulations for these phenomena.

5.4 Quarkyonic matter

In the studies done in chapter 4, we extended the quarkyonic model of McLerran and Reddy [MR19] for pure neutron matter to include realistic hadronic (MS) and quark (vNJL) equations of state. It was found that including these realistic EOSs improve the estimates of radii. The onset of quarks is found to be at $\sim 2n_0$ and models within the quarkyonia formalism remain causal for all densities. However, these studies lack inclusion of leptons. Thus, our next step would be to study beta-equilibrated matter which includes leptons (e^-, μ). This can be done by including individual shells for both protons and neutrons, and by including leptons as non interacting Fermi gases. An obvious extension to the beta-equilibrated EOS is to finite temperatures. Leptons play an important role in understanding the cooling mechanism of proto-neutron stars, isolated neutron stars or the remnants of binary mergers. Finite temperature EOS is also an input to calculations involving crustal cooling and long-term cooling. The corresponding mass-radius curves will be useful to compare with those obtained from data of cooling and spin-down rates of neutron stars.

References

[A+08] A. Arcones et al. Influence of light nuclei on neutrino-driven supernova outflows. *Phys. Rev. C*, 78:015806, 2008.

[A+16] B. P. Abbott et al. Observation of gravitational waves from a binary black hole merger. *Phys. Rev. Lett.*, 116:061102, 2016.

[A+17a] B. P. Abbott et al. Gravitational waves and gamma-rays from a binary neutron star merger: Gw170817 and grb 170817a. *Astro. Phys. J. Lett.*, 848:L12, 2017.

[A+17b] B. P. Abbott et al. Multi-messenger Observations of a Binary Neutron Star Merger. *Astrophys. J.*, 848(2):L12, 2017.

[A+17c] Benjamin P. Abbott et al. GW170817: Observation of Gravitational Waves from a Binary Neutron Star Inspiral. *Phys. Rev. Lett.*, 119(16):161101, 2017. doi:10.1103/PhysRevLett.119.161101

[A+18] B. P. Abbott et al. GW170817: Measurements of neutron star radii and equation of state. *Phys. Rev. Lett.*, 121(16):161101, 2018.

[A+19] B. P. Abbott et al. Properties of the binary neutron star merger GW170817. *Phys. Rev. X*, 9(1):011001, 2019.

[ABPR05] Mark Alford, Matt Braby, M.W. Paris, and Sanjay Reddy. Hybrid stars that masquerade as neutron stars. *Astrophys. J.*, 629:969–978, 2005.

[AFW+13] John Antoniadis, Paulo C.C. Freire, Norbert Wex, Thomas M. Tauris, Ryan S. Lynch, et al. A Massive Pulsar in a Compact Relativistic Binary. *Science*, 340:6131, 2013.

[AHP13] Mark G. Alford, Sophia Han, and Madappa Prakash. Generic conditions for stable hybrid stars. *Phys. Rev. D*, 88(8):083013, 2013.

[And02] J. B. Anderson. *Diffusion and Greens Function Quantum Monte Carlo Methods*, volume 10 of *NIC*. John von Neumann Institute for Computing, Jülich, 2002.

[AP97] A. Akmal and V. R. Pandharipande. Spin - isospin structure and pion condensation in nucleon matter. *Phys. Rev. C*, 56:2261–2279, 1997.

[APR98] A. Akmal, V. R. Pandharipande, and D. G. Ravenhall. The Equation of state of nucleon matter and neutron star structure. *Phys. Rev. C*, 58:1804–1828, 1998.

[ARRW01] Mark G. Alford, Krishna Rajagopal, Sanjay Reddy, and Frank Wilczek. The Minimal CFL nuclear interface. *Phys. Rev. D*, 64:074017, 2001.

[AS72] M. Abramowitz and I. A. Stegun. *Handbook of Mathematical Functions*. National Bureau of Standards, Applied Mathematics Series 55, 10, 1972.

[ASRS08] Mark G. Alford, Andreas Schmitt, Krishna Rajagopal, and Thomas Schäfer. Color superconductivity in dense quark matter. *Rev. Mod. Phys.*, 80:1455–1515, 2008.

[BB77] J. Boguta and A. R. Bodmer. Relativistic calculation of nuclear matter and the nuclear surface. *Nucl. Phys. A*, 292(3):413, 1977.

[BBAL79] H. A. Bethe, G. E. Brown, J. Applegate, and J. M. Lattimer. Equation of state in the gravitational collapse of stars. *Nucl. Phys. A*, 324 (2-3):487–533, 1979.

[BBB+19] Andreas Bauswein, Niels-Uwe F. Bastian, David B. Blaschke, Katerina Chatziioannou, James A. Clark, Tobias Fischer, and Micaela Oertel. Identifying a first-order phase transition in neutron star mergers through gravitational waves. *Phys. Rev. Lett.*, 122(6):061102, 2019.

[BBGN95] M. Bocquet, S. Bonazzola, E. Gourgoulhon, and J. Novak. Rotating neutron star models with magnetic field. *Astron. Astrophys.*, 301:757, 1995.

[BBP71] G. Baym, H. A. Bethe, and C. J Pethick. Neutron star matter. *Nucl. Phys.*, A175(2):225, 1971.

[BC76a] G. Baym and S. A. Chin. Can a Neutron Star Be a Giant MIT Bag? *Phys. Lett. B*, 62:241–244, 1976.

[BC76b] Gordon Baym and Siu A. Chin. Landau Theory of Relativistic Fermi Liquids. *Nucl. Phys. A*, 262:527–538, 1976.

[BD80] Sidney A. Bludman and C. B. Dover. EXTRAPOLATION OF THE PHENOMENOLOGICAL NUCLEAR EQUATION OF STATE TO HIGH DENSITIES. *Phys. Rev. D*, 22:1333–1336, 1980.

[BHK+18] Gordon Baym, Tetsuo Hatsuda, Toru Kojo, Philip D. Powell, Yifan Song, and Tatsuyuki Takatsuka. From hadrons to quarks in neutron stars: a review. *Rept. Prog. Phys.*, 81(5):056902, 2018.

[BJ12] A. Bauswein and H. T Janka. Measuring neutron-star properties via gravitational waves from neutron-star mergers. *Phys. Rev. Lett*, 108:0111101, 2012.

[BL84] A. Burrows and J. M. Lattimer. On the accuracy of the single-nucleus approximation in the equation of state of hot, dense matter. *Astrophys. J.*, 285:294, 1984.

[BL86] A. Burrows and J. M. Lattimer. The birth of neutron stars. *Astrophys. J.*, 307:178, 1986.

[BMG10] Abhijit Bhattacharyya, Igor N. Mishustin, and Walter Greiner. Deconfinement Phase Transition in Compact Stars : Maxwell vs. Gibbs Construction of the Mixed Phase. *J. Phys.*, G37:025201, 2010. arXiv:0905.0352, doi:10.1088/0954-3899/37/2/025201

[BO99] M. Buballa and M. Oertel. Strange quark matter with dynamically generated quark masses. *Phys. Lett. B*, 457(4):261 – 267, 1999. doi:https://doi.org/10.1016/S0370-2693(99)00533-X

[BP91] G. Baym and C. J. Pethick. *Landau Fermi-Liquid Theory*. Wiley Interscience, New York, 1991.

[BPL00] A. Broderick, M. Prakash, and J. M. Lattimer. The equation of state of neutron star matter in strong magnetic fields. *Astrophys. Jl.*, 537:351, 2000.

[BPL02] A. Broderick, M. Prakash, and J. M Lattimer. Effects of strong magnetic fields in strange baryonic matter. *Phys. Lett. B*, 531:167, 2002.

[BPS71] G. Baym, C. Pethick, and P. Sutherland. The ground state of matter at high densities: Equation of state and stellar models. *Astrophys. J.*, 170:299, 1971. doi:10.1086/151216

[BR16] Cosima Breu and Luciano Rezzolla. Maximum mass, moment of inertia and compactness of relativistic stars. *Mon. Not. R. Astron. Soc.*, 459(1):646–656, 2016.

[BR17] L. Baiotti and L. Rezzolla. Binary neutron star mergers: a review of einstein's richest laboratory. *Reports on Progress in Physics*, 80:1, 2017.

[BRO+16] Sebastiano Bernuzzi, David Radice, Christian D. Ott, Luke F. Roberts, Philipp Msta, and Filippo Galeazzi. How loud are neutron star mergers? *Phys. Rev. D*, 94:024023, 2016.

[BS10] T. W. Baumgarte and S. L. Shapiro. *Numerical Relativity*. Cambridge University Press, New York, 2010.

[BSB18] G. Bozzola, N. Sterigoulas, and A. Bauswein. Universal relations for differentially rotating relativistic stars at the threshold to collapse. *MNRAS*, 474:3557, 2018.

[BSJ16] A. Bauswein, N. Stergioulas, and H.-T. Janka. Exploring properties of high-density matter through remnants of neutron-star mergers. *Eur. Phys. J. A*, 52 : 56:1–22, 2016.

[BSS00] T. W. Baumgarte, S. Shapiro, and M. Shibata. On the maximum mass of differentially rotating neutron stars. *Astrophys. Jl.*, 528:L29, 2000.

[BU37] E. Beth and G. E. Uhlenbeck. The quantum theory of the non-ideal gas. ii. behaviour at low temperatures. *Physica*, 4:915, 1937.

[Bub05] Michael Buballa. NJL model analysis of quark matter at large density. *Phys. Rept.*, 407:205–376, 2005.

[BZ34a] W. Baade and F. Zwicky. On super-novae. *Proceedings of the National Academy of Sciences*, 20(5):254–259, 1934. doi:10.1073/pnas.20.5.254

[BZ34b] W. Baade and F. Zwicky. Remarks on super-novae and cosmic rays. *Phys. Rev.*, 46:76–77, Jul 1934. URL: https://link.aps.org/doi/10.1103/PhysRev.46.76.2, doi:10.1103/PhysRev.46.76.2

[C+17] R. Chornock et al. The electromagnetic counterpart of the binary neutron star merger ligo/virgo GW170817. IV. detection of near-infrared signatures of r-process nucleosynthesis with gemini-south. *Astro. Phys. J. Lett.*, 848(2):L19, oct 2017. doi:10.3847/2041-8213/aa905c

[C+19] H. Thankful Cromartie et al. A very massive neutron star: relativistic Shapiro delay measurements of PSR J0740+6620. *arXiv e-prints*, 2019. arXiv:1904.06759.

[Cha32] James Chadwick. The existence of a neutron. *Proc. R. Soc. Lond. A.*, 136:692, May 1932.

[Chi77] S. A. Chin. A relativistic many-body theory of high density matter. *Ann. Phys.*, 108:301–367, 1977.

[CLP17a] C. Constantinou, S. Lalit, and M. Prakash. Thermal effects in dense matter beyond mean field theory. *Int. J. Mod. Phys. E*, 26:1740005, 2017.

[CLP17b] C. Constantinou, S. Lalit, and M. Prakash. *Thermal Effects in Dense Matter Beyond Mean Field Theory*. World Scientific, Singapore, 2017.

[CMPL14] Constantinos Constantinou, Brian Muccioli, Madappa Prakash, and James M. Lattimer. Thermal properties of supernova matter: The bulk homogeneous phase. *Phys. Rev. C*, 89(6):065802, 2014.

[CMPL15a] C. Constantinou, B. Muccioli, M. Prakash, and J. M. Lattimer. Degenerate limit thermodynamics beyond leading order for models of dense matter. *Ann. Phys.*, 363:533–555, 2015.

[CMPL15b] C. Constantinou, B. Muccioli, M. Prakash, and J. M. Lattimer. Thermal properties of hot and dense matter with finite range interactions. *Phys. Rev. C*, 92:025801, 2015.

[CP75] John C. Collins and M. J. Perry. Superdense Matter: Neutrons Or Asymptotically Free Quarks? *Phys. Rev. Lett.*, 34:1353, 1975. doi:10.1103/PhysRevLett.34.1353

[CP14] Wei-Chia Chen and J. Piekarewicz. Building relativistic mean field models for finite nuclei and neutron stars. *Phys. Rev. C*, 90(4):044305, 2014.

[CP17] C. Constantinou and M. Prakash. Enforcing causality in nonrelativistic equations of state at finite temperature. *Phys. Rev. C*, 95:055802, 2017.

[CPL01] C. Cardall, M. Prakash, and J. M. Lattimer. Effects of strong magnetic fields on neutron star structure. *Astro. Phys. J.*, 554:322, 2001.

[CST94] G. B. Cook, S. L. Shapiro, and S. L. Teukolsky. Rapidly rotating neutron stars in general relativity: Realistic equations of state. *Astrophys. Jl.*, 422:227, 1994.

[DFL+18] Soumi De, Daniel Finstad, James M. Lattimer, Duncan A. Brown, Edo Berger, and Christopher M. Biwer. Tidal Deformabilities and Radii of Neutron Stars from the Observation of GW170817. *Phys. Rev. Lett.*, 121(9):091102, 2018.

[DH01] F. Douchin and P. Haensel. A unified equation of state of dense matter and neutron star structure. *Astron. Astrophys.*, 380:151, 2001.

[DN09] Thibault Damour and Alessandro Nagar. Relativistic tidal properties of neutron stars. *Phys. Rev. D*, 80:084035, 2009.

[DNS15] V. Dexheimer, R. Negreiros, and S. Schramm. Role of strangeness in hybrid stars and possible observables. *Phys. Rev. C*, 91(5):055808, 2015.

[DPR+10] Paul Demorest, Tim Pennucci, Scott Ransom, Mallory Roberts, and Jason Hessels. Shapiro Delay Measurement of A Two Solar Mass Neutron Star. *Nature*, 467:1081–1083, 2010.

[DS10] V. A. Dexheimer and S. Schramm. A Novel Approach to Model Hybrid Stars. *Phys. Rev. C*, 81:045201, 2010.

[ELPS89] D. Eichler, M. Livio, T. Piran, and D. N. Schramm. Nucleosynthesis, neutrino bursts and γ-rays from coalescing neutron stars. *Nature*, 340:126–128, 1989.

[EOHJ+96] L. Engvik, E. Osnes, M. Hjorth-Jensen, G. Bao, and E. Ostgaard. Asymmetric nuclear matter and neutron star properties. *Astrophys. Jl.*, 469:794, 1996.

[Eps78] R. Epstein. The generation of gravitational radiation by escaping supernova neutrinos. *Astrophys. J.*, 223:1037–1045, August 1978. doi:10.1086/156337

[Fav14] Marc Favata. Systematic parameter errors in inspiraling neutron star binaries. *Phys. Rev. Lett.*, 112:101101, 2014.

[FH08] Eanna E. Flanagan and Tanja Hinderer. Constraining neutron star tidal Love numbers with gravitational wave detectors. *Phys. Rev. D*, 77:021502(R), 2008.

[FHS19] Eduardo S. Fraga, M. Hippert, and Andreas Schmitt. Surface tension of dense matter at the chiral phase transition. *Phys. Rev. D*, 99(1):014046, 2019.

[FJ84] Edward Farhi and R. L. Jaffe. Strange Matter. *Phys. Rev. D*, 30:2379, 1984. doi:10.1103/PhysRevD.30.2379

[FK16] Kenji Fukushima and Toru Kojo. The Quarkyonic Star. *Astrophys. J.*, 817(2):180, 2016.

[FM78] Barry Freedman and Larry D. McLerran. Quark Star Phenomenology. *Phys. Rev. D*, 17:1109, 1978.

[Foc30a] V. Fock. Näherungsmethode zur lösung des quantenmechanischen mehrkörperproblem. *Zeitschrift für Physik*, 61(1):126–148, Jan 1930. doi:10.1007/BF01340294

[Foc30b] V. Fock. "selfconsistent field" mit austausch für natrium. *Zeitschrift für Physik*, 62(11):795–805, Nov 1930. doi:10.1007/BF01330439

[FPH18] F. J. Fattoyev, J. Piekarewicz, and C. J. Horowitz. Neutron Skins and Neutron Stars in the Multimessenger Era. *Phys. Rev. Lett.*, 120(17):172702, 2018.

[FR12] J. A. Faber and F. A. Rasio. Binary neutron star mergers. *Living Rev Relativ*, 15: 8:1–83, 2012.

[FS13] J. L. Friedman and N. Stergioulas. *Rotating Relativistic Stars*. Cambridge University Press, Cambridge, 2013.

[Gau28] J. A. Gaunt. A theory of hartree's atomic fields. *Math. Proc. Camb. Philos. Soc.*, 24(2):328–342, 1928. doi:10.1017/S0305004100015851

[GCS19] R. O. Gomes, Prasanta Char, and S. Schramm. Constraining strangeness in dense matter with GW170817. *Astrophys. J.*, 877(2):139, 2019.

[GGR19] D. Gonzalez-Caniulef, S. Guillot, and A. Reisenegger. Neutron star radius measurement from the ultraviolet and soft X-ray thermal emission of PSR J0437-4715. *arXiv e-prints*, April 2019. arXiv:1904.12114.

[GKR+18] Tyler Gorda, Aleksi Kurkela, Paul Romatschke, Matias Säppi, and Aleksi Vuorinen. Next-to-Next-to-Next-to-Leading Order Pressure of Cold Quark Matter: Leading Logarithm. *Phys. Rev. Lett.*, 121(20):202701, 2018.

[Gle92] Norman K. Glendenning. First order phase transitions with more than one conserved charge: Consequences for neutron stars. *Phys. Rev. D*, 46:1274–1287, 1992. doi:10.1103/PhysRevD.46.1274

[Gle01] N. K. Glendenning. Phase transitions and crystalline structures in neutron star cores. *Phys. Rept.*, 342:393–447, 2001. doi:10.1016/S0370-1573(00)00080-6

[H+87] K. Hirata et al. Observation of a neutrino burst from the supernova sn1987a. *Phys. Rev. Lett.*, 58:1490–1493, Apr 1987. URL: https://link.aps.org/doi/10.1103/PhysRevLett.58.1490, doi:10.1103/PhysRevLett.58.1490

[Har28] D. R. Hartree. The wave mechanics of an atom with a non-coulomb central field. part i. theory and methods. *Math. Proc. Camb. Philos. Soc.*, 24(1):89–110, 1928. doi:10.1017/S0305004100011919

[HBP+68] A. Hewish, S. J. Bell, J. D. H. Pilkington, P. F. Scott, and R. A. Collins. Observation of a rapidly pulsating radio source. *Nature*, 217:709–713, 1968.

[Hin08] Tanja Hinderer. Tidal Love numbers of neutron stars. *Astrophys. J.*, 677:1216–1220, 2008.

[HK64] P. Hohenberg and W. Kohn. Inhomogeneous electron gas. *Phys. Rev. B*, 76:6062, 1964.

[HK94] Tetsuo Hatsuda and Teiji Kunihiro. QCD phenomenology based on a chiral effective Lagrangian. *Phys. Rept.*, 247:221–367, 1994.

[HLLR10a] T. Hinderer, B. D. Lackey, R. N. Lang, and J. S. Read. Tidal deformability of neutron stars with realistic equations of state and their gravitational wave signatures in binary inspiral. *Phys. Rev. D*, 81:123016, 2010.

[HLLR10b] Tanja Hinderer, Benjamin D. Lackey, Ryan N. Lang, and Jocelyn S. Read. Tidal deformability of neutron stars with realistic equations of state and their gravitational wave signatures in binary inspiral. *Phys. Rev. D*, 81:123016, 2010.

[HLPS10] K. Hebeler, J. M. Lattimer, C. J. Pethick, and A. Schwenk. Constraints on neutron star radii based on chiral effective field theory interactions. *Phys. Rev. Lett.*, 105:161102, 2010.

[HLPS13] K. Hebeler, J. M. Lattimer, C. J. Pethick, and A. Schwenk. Equation of state and neutron star properties constrained by nuclear physics and observation. *Astophys. Jl*, 773:11, 2013.

[HML+19] Sophia Han, Md. Abdullah Al Mamun, Sudhanva Lalit, Constantinos Constantinou, and Madappa Prakash. Treating quarks within neutron stars. *arXiv e-prints*, page arXiv:1906.04095, Jun 2019. arXiv:1906.04095.

[HP01a] C. J. Horowitz and J. Piekarewicz. Neutron star structure and the neutron radius of Pb-208. *Phys. Rev. Lett.*, 86:5647, 2001.

[HP01b] Charles J. Horowitz and Jorge Piekarewicz. The Neutron radii of Pb-208 and neutron stars. *Phys. Rev. C*, 64:062802, 2001.

[HS06] C. J. Horowitz and A. Schwenk. Cluster formation and the virial equation of state of low-density nuclear matter. *Nucl. Phys. A*, 776:55, 2006.

[HS19] Sophia Han and Andrew W. Steiner. Tidal deformability with sharp phase transitions in (binary) neutron stars. *Phys. Rev. D*, 99(8):083014, 2019.

[HSM+01] M. Hanauske, L. M. Satarov, I. N. Mishustin, Horst Stoecker, and W. Greiner. Strange quark stars within the Nambu-Jona-Lasinio model. *Phys. Rev. D*, 64:043005, 2001. arXiv:astro-ph/0101267, doi:10.1103/PhysRevD.64.043005

[HSUU15] O. Hamil, J. R. Stone, M. Urbanec, and G. Urbancová. Braking index of isolated pulsars. *Phys. Rev. D*, 91(6):063007, 2015.

[Jas55] Robert Jastrow. Many-body problem with strong forces. *Phys. Rev.*, 98:1479–1484, Jun 1955. doi:10.1103/PhysRev.98.1479

[JK17] Simon Johnston and Aris Karastergiou. Pulsar braking and the P?$\dot{P}$ diagram. *Mon. Not. Roy. Astron. Soc.*, 467(3):3493–3499, 2017.

[Kal62] M. H. Kalos. Monte carlo calculations of the ground state of three- and four-body nuclei. *Phys. Rev.*, 128:1791–1795, Nov 1962. URL: https://link.aps.org/doi/10.1103/PhysRev.128.1791, doi:10.1103/PhysRev.128.1791

[KF15] Thomas Klähn and Tobias Fischer. Vector interaction enhanced bag model for astrophysical applications. *Astrophys. J.*, 810(2):134, 2015.

[KJ95] W. Keil and H.T. Janka. Hadronic phase transitions at supranuclear densities and the delayed collapse of newly formed neutron stars. *Astron. & Astrophys.*, 296:145, 1995.

[KMS+87] W. Kunkel, B. Madore, I. Shelton, O. Duhalde, F. M. Bateson, A. Jones, B. Moreno, S. Walker, G. Garradd, B. Warner, and J. Menzies. Supernova 1987A in the Large Magellanic Cloud. *IAUCIRC*, 4316, February 1987.

[KPSB15] Toru Kojo, Philip D. Powell, Yifan Song, and Gordon Baym. Phenomenological qcd equation of state for massive neutron stars. *Phys. Rev. D*, 91:045003, Feb 2015. doi:10.1103/PhysRevD.91.045003

[KRV10] Aleksi Kurkela, Paul Romatschke, and Aleksi Vuorinen. Cold Quark Matter. *Phys. Rev. D*, 81:105021, 2010.

[KS65] W. Kohn and L. J. Sham. Self-consistent equations including exchange and correlation effects. *Phys. Rev. A*, 140:1133, 1965.

[Kun89] T. Kunihiro. Effects of the U(a)(1) Anomaly on the Quark Condensates and Meson Properties at Finite Temperature. *Phys. Lett. B*, 219:363–368, 1989.

[KV16] Aleksi Kurkela and Aleksi Vuorinen. Cool quark matter. *Phys. Rev. Lett.*, 117(4):042501, 2016.

[Lan57a] L. D. Landau. Oscillations in a fermi liquid. *JETP (Sov. Phys.)*, 5:101, 1957. [ZhETF (USSR) **32**, 59 (1957)].

[Lan57b] L. D. Landau. The theory of a fermi liquid. *JETP (Sov. Phys.)*, 3:920, 1957. [ZhETF (USSR) **30**, 1058 (1956)].

[Lat12] James M. Lattimer. The nuclear equation of state and neutron star masses. *Ann. Rev. Nucl. Part. Sci.*, 62(1):485–515, 2012. arXiv:https://doi.org/10.1146/annurev-nucl-102711-095018, doi:10.1146/annurev-nucl-102711-095018

[LGAA13] G. Lugones, A. G. Grunfeld, and M. Al Ajmi. Surface tension and curvature energy of quark matter in the Nambu-Jona-Lasinio model. *Phys. Rev. C*, 88(4):045803, 2013.

[LIG] Ligo and virgo detect neutron star smash-ups. https://www.ligo.org/news/pr-O3NSmergerMay2019.pdf. Accessed: 2019-05-22.

[Lin98] Lee Lindblom. Phase transitions and the mass radius curves of relativistic stars. *Phys. Rev. D*, 58:024008, 1998.

[LL80a] L. D. Landau and E. M. Lifshitz. *Statistical Physics Part 1*. Butterworth Heinemann, Oxford, third edition, 1980.

[LL80b] L. D. Landau and E. M. Lifshitz. *Statistical Physics Part 2*. Butterworth Heinemann, Oxford, third edition, 1980.

[LL13] James M. Lattimer and Yeunhwan Lim. Constraining the Symmetry Parameters of the Nuclear Interaction. *Astrophys. J.*, 771:51, 2013.

[LLPR83] D. Q. Lamb, J. M. Lattimer, C. J. Pethick, and D. G. Ravenhall. Phase transitions in cold and warm dense matter. *Nucl. Phys. A*, 411:449–473, 1983.

[LLPR85] D. Q. Lamb, J. M. Lattimer, C. J. Pethick, and D. G. Ravenhall. Physical properties of hot, dense matter: The general case. *Nucl. Phys.*, A432:646, 1985.

[LMCP19] S. Lalit, M. A. A. Mamun, C. Constantinou, and M. Prakash. Dense matter equation of state for neutron star mergers. *Eur. Phys. J. A*, 55:10, 2019.

[Lov09] A. E. H. Love. The yielding of the earth to disturbing forces. *Proc. R. Soc. A*, 82:73, 1909.

[LP01] J. M. Lattimer and M. Prakash. Neutron star structure and the equation of state. *Astrophys. J.*, 550:426, 2001.

[LP07] J. M. Lattimer and M. Prakash. Neutron star observations: Prognosis for equation of state constraints. *Phys. Rep.*, 442:109, 2007.

[LP11] J. M. Lattimer and M. Prakash. What a two solar mass neutron star means. In S Lee, editor, *From Nuclei to Neutron Stars*, page 275. Singapore: World Scientific, 2011.

[LP16] James M. Lattimer and Madappa Prakash. The Equation of State of Hot, Dense Matter and Neutron Stars. *Phys. Rept.*, 621:127–164, 2016.

[LPMY90] James M. Lattimer, Madappa Prakash, Dieter Masak, and Amos Yahil. Rapidly rotating pulsars and the equation of state. *Astrophys. J.*, 355:241–254, 1990.

[LPPH91a] J. M. Lattimer, M. Prakash, C. J. Pethick, and P. Haensel. Direct URCA process in neutron stars. *Phys. Rev. Lett.*, 66:2701–2704, 1991. doi:10.1103/PhysRevLett.66.2701

[LPPH91b] James M. Lattimer, C. J. Pethick, Madappa Prakash, and Pawel Haensel. Direct URCA process in neutron stars. *Phys. Rev. Lett.*, 66:2701–2704, 1991. doi:10.1103/PhysRevLett.66.2701

[LS74] J. M. Lattimer and D. N. Schramm. Black-hole-neutron-star collisions. *Astrophys. J*, 192:L145–L147, September 1974. doi:10.1086/181612

[LS76] J. M. Lattimer and D. N. Schramm. The tidal disruption of neutron stars by black holes in close binaries. *Astrophys. J.*, 210:549–567, December 1976. doi:10.1086/154860

[LS91] J. M. Lattimer and F. Swesty. A generalized equation of state for hot, dense matter. *Nucl. Phys. A*, 535:331, 1991.

[MDK+18] Zach Meisel, Alex Deibel, Laurens Keek, Peter Shternin, and Justin Elfritz. Nuclear physics of the outer layers of accreting neutron stars. *Journal of Physics G: Nuclear and Particle Physics*, 45(9):093001, jul 2018. URL: https://doi.org/10.1088%2F1361-6471%2Faad171, doi:10.1088/1361-6471/aad171

[MFPSB10] B. W. Mintz, E. S. Fraga, G. Pagliara, and J. Schaffner-Bielich. Nucleation of quark matter in protoneutron star matter. *Phys. Rev. D*, 81:123012, 2010.

[MHT13] Kota Masuda, Tetsuo Hatsuda, and Tatsuyuki Takatsuka. Hadronquark crossover and massive hybrid stars. *Prog. Theor. Exp. Phys.*, 2013(7), 07 2013. doi:10.1093/ptep/ptt045

[Mil16] M. Coleman Miller. The case for PSR J1614-2230 as a NICER target. *Astrophys. J.*, 822(1):27, apr 2016.

[ML16] M. Coleman Miller and Frederick K. Lamb. Observational constraints on neutron star masses and radii. *European Physical Journal A*, 52:63, Mar 2016. arXiv:1604.03894, doi:10.1140/epja/i2016-16063-8

[MM17] Ben Margalit and Brian D. Metzger. Constraining the Maximum Mass of Neutron Stars From Multi-Messenger Observations of GW170817. *Astrophys. J.*, 850(2):L19, 2017.

[MMF12] Nadja S. Magalhaes, Thaysa A. Miranda, and Carlos Frajuca. Predicting Ranges for Pulsars' Braking Indices. *Astrophys. J.*, 755:54, 2012.

[MP07] Larry McLerran and Robert D. Pisarski. Phases of cold, dense quarks at large N(c). *Nucl. Phys. A*, 796:83–100, 2007.

[MPA87] H. Müther, M. Prakash, and T. L. Ainsworth. The nuclear symmetry energy in relativistic brueckner-hartree-fock calculations. *Phys. Lett.*, B199:469, 1987.

[MPD+19] Elias R. Most, L. Jens Papenfort, Veronica Dexheimer, Matthias Hanauske, Stefan Schramm, Horst Stöcker, and Luciano Rezzolla. Signatures of quark-hadron phase transitions in general-relativistic neutron-star mergers. *Phys. Rev. Lett.*, 122(6):061101, 2019.

[MR19] Larry McLerran and Sanjay Reddy. Quarkyonic matter and neutron stars. *Phys. Rev. Lett.*, 122:122701, Mar 2019. doi:10.1103/PhysRevLett.122.122701

[MS76] Gerald A Miller and James E Spencer. A survey of pion charge-exchange reactions with nuclei. *Ann. Phys.*, 100(1):562 – 606, 1976. doi:https://doi.org/10.1016/0003-4916(76)90073-7

[MS96] Horst Müller and Brian D. Serot. Relativistic mean-field theory and the high-density nuclear equation of state. *Nuclear Physics A*, 606(3):508 – 537, 1996. doi:https://doi.org/10.1016/0375-9474(96)00187-X

[NC73] M. Nauenberg and G. Chapline. Determination of properties of cold stars in general relativity by a variational method. *Astrophys. J.*, 179(1):277, 1973.

[NDS10] Rodrigo Negreiros, V. A. Dexheimer, and S. Schramm. Modeling Hybrid Stars with an SU(3) non-linear sigma model. *Phys. Rev. C*, 82:035803, 2010.

[Neg82] J. W. Negele. The mean-field theory of nuclear structure and dynamics. *Rev. Mod. Phys.*, 54, 4:913, 1982.

[NJL61] Yoichiro Nambu and G. Jona-Lasinio. Dynamical Model of Elementary Particles Based on an Analogy with Superconductivity. 1. *Phys. Rev.*, 122:345–358, 1961.

[NV73] J. W. Negele and D. Vautherin. Neutron star matter at sub-nuclear densities. *Nucl. Phys. A*, 207:298, 1973.

[OGH+07] E. O'Connor, D. Gazit, C. J. Horowitz, A. Schwenk, and N. Barnea. Neutrino breakup of $a = 3$ nuclei in supernovae. *Phys. Rev. C*, 75:055803, 2007.

[OHKT17] M. Oertel, M. Hempel, T. Klähn, and S. Typel. Equations of state for supernovae and compact stars. *Rev. Mod. Phys.*, 89:015007, 2017.

[ÖPA+16] Feryal Özel, Dimitrios Psaltis, Zaven Arzoumanian, Sharon Morsink, and Michi Baubock. Measuring Neutron Star Radii via Pulse Profile Modeling with NICER. *Astrophys. J.*, 832(1):92, 2016.

[P+97] M. Prakash et al. Composition and structure of protoneutron stars. *Phys. Rep.*, 280:1, 1997.

[PABW87] M. Prakash, T. L. Ainsworth, J. P. Blaizot, and H. Wolter. Windsurfing the fermi sea, volume ii. 1987.

[PAL88] M. Prakash, T. L. Ainsworth, and J. M. Lattimer. Equation of state and the maximum mass of neutron stars. *Phys. Rev. Lett.*, 61:2518–2521, 1988.

[PB11] R. K. Pathria and P. D. Beale. *Statistical Mechanics*. Elsevier, Oxford, third edition, 2011.

[PBP90] Manju Prakash, E. Baron, and Madappa Prakash. Rotation of stars containing strange quark matter. *Phys. Lett. B*, 243:175–180, 1990.

[PEK92] M. Prakash, P. J. Ellis, and J. I. Kapusta. Relativistic nuclear matter with composite nucleons. *Phys. Rev. C*, 45:2518–2521, 1992.

[PLPS04a] D. Page, J. M. Lattimer, M. Prakash, and A. W. Steiner. Minimal cooling of neutron stars: A new paradigm. *Astrophys. J.*, 155 (Suppl.):623, 2004.

[PLPS04b] Dany Page, James M. Lattimer, Madappa Prakash, and Andrew W. Steiner. Minimal Cooling of Neutron Stars: A New Paradigm. *Astrophys. J. Suppl.*, 155(2):623–650, Dec 2004. arXiv:astro-ph/0403657, doi:10.1086/424844

[PLPS15] D. Page, J. M. Lattimer, M. Prakash, and A. W. Steiner. Stellar superfluids, volume 2. In K. H. Benneman and J. B. Ketterson, editors, *Novel Superfluids*, page 505, Oxford, 2015. Oxford University Press.

[PLSV01] M. Prakash, J. M. Lattimer, R. F. Sawyer, and R. R Volkas. Neutrino propagation in dense astrophysical systems. *Ann. Rev. Nucl. Part. Sci.*, 51:295, 2001.

[PMPL01] J. A. Pons, J. A. Miralles, M. Prakash, and J. M. Lattimer. Evolution of protoneutron stars with kaon condensates. *Astrophys. J.*, 553:382, 2001.

[PN66] D. Pines and P. Nozières. *The Theory of Quantum Liquids, Volume I: Normal Fermi Liquids*. W. A. Benjamin, Inc., New York, 1966.

[PPL10] Sergey Postnikov, Madappa Prakash, and James M. Lattimer. Tidal Love Numbers of Neutron and Self-Bound Quark Stars. *Phys. Rev. D*, 82:024016, 2010.

[PR95] C. J. Pethick and D. G. Ravenhall. Matter at large neutron excess and the physics of neutron-star crusts. *Annu. Rev. Nucl. Part. Sci.*, 45:429, 1995.

[Pra96] M. Prakash. The nuclear equation of state and neutron stars. In A. Ansari and L. Satpathy, editors, *Nuclear equation of State*, page 229, Singapore, 1996. World Scientific.

[PRP+99] J. A. Pons, S. Reddy, M. Prakash, J. M. Lattimer, and J. A. Miralles. Evolution of proto-neutron stars. *Astrophys. J*, 513:382, 1999.

[PS08] C. J. Pethick and H. Smith. *Bose-Einstein Condensation in Dilute Gases*. Cambridge University Press, Cambridge, 2nd edition, 2008.

[PS17] V. Paschalidis and N. Stergioulas. Rotating stars in relativity. *Living Rev Relativ*, 20: 7:1–169, 2017.

[PSPL01] J. A. Pons, A. W. Steiner, M. Prakash, and J. M. Lattimer. Evolution of proto-neutron stars with quarks. *Phys. Rev. Lett.*, 86:5223, 2001.

[PT17] H. Pais and S. Typel. Comparison of equation of state models with different cluster dissolution mechanisms. In W. U. Schröder, editor, *Nuclear Particle Correlations and Cluster Physics*, page 95. Singapore: World Scientific Publishing Co. Pte. Ltd., 2017.

[Rai19] C. A. Raithel. Constraints on the Neutron Star Equation of State from GW170817. *arXiv e-prints*, April 2019. arXiv:1904.10002.

[RMRR18] A. Roggero, J. Margueron, L. F. Roberts, and S. Reddy. Nuclear pasta in hot dense matter and its implications for neutrino scattering. *Phys. Rev. C*, 97:045804, 2018.

[RMW18] Luciano Rezzolla, Elias R. Most, and Lukas R. Weih. Using gravitational-wave observations and quasi-universal relations to constrain the maximum mass of neutron stars. *The Astrophysical Journal Letters*, 852(2):L25, 2018. URL: http://stacks.iop.org/2041-8205/852/i=2/a=L25

[RPW83] D. G. Ravenhall, C. J. Pethick, and J. R. Wilson. Structure of matter below nuclear saturation density. *Phys. Rev. Lett.*, 50:2066, 1983.

[RPZB18] David Radice, Albino Perego, Francesco Zappa, and Sebastiano Bernuzzi. GW170817: Joint Constraint on the Neutron Star Equation of State from Multimessenger Observations. *Astrophys. J.*, 852(2):L29, 2018. arXiv:1711.03647, doi:10.3847/2041-8213/aaa402

[RSC+12] L. F. Roberts, G. Shen, V. Cirigliano, J. A. Pons, S. Reddy, and S. E. Woosley. Protoneutron star cooling with convection: The effect of the symmetry energy. *Phys. Rev. Lett.*, 108:1103, 2012.

[Sch88] J. Schwinger. *Particles, Sources and Fields, vol. 3*. Addison Wesley, Redwood City, 1988.

[SCMP19] A. S. Schneider, C Constantinou, B Muccioli, and M. Prakash. The apr equation of state for simulations of supernovae, neutron stars and binary mergers. *arXiv:1901.09652*, 2019.

[Sei71] Z. F. Seidov. The Stability of a Star with a Phase Change in General Relativity Theory. *Sov. Astron.*, 15:347, October 1971.

[Shi15] M. Shibata. *Numerical Relativity*. World Scientific, Singapore, 2015.

[SHT10] G. Shen, C. J. Horowitz, and S. Teige. Equation of state of nuclear matter in a virial expansion of nucleons and nuclei. *Phys. Rev. C*, 82:045802, 2010.

[Sla28] J. C. Slater. The self consistent field and the structure of atoms. *Phys. Rev.*, 32(3):339–348, Sep 1928.

[SLB16] A. W. Steiner, J. M. Lattimer, and E. F. Brown. Neutron Star Radii, Universal Relations, and the Role of Prior Distributions. *Eur. Phys. J. A*, 52(2):18, 2016.

[SPL00] A. Steiner, M. Prakash, and J. M. Lattimer. Quark-hadron phase transitions in young and old neutron stars. *Phys. Lett. B*, 486:239–248, 2000.

[SPLE05] Andrew W. Steiner, Madappa Prakash, James M. Lattimer, and Paul J. Ellis. Isospin asymmetry in nuclei and neutron stars. *Phys. Rept.*, 411:325–375, 2005.

[SRO17] A. S. Schneider, L. F. Roberts, and C. D. Ott. Open-source nuclear equation of state framework based on the liquid-drop model with skyrme interaction. *Phys. Rev. C*, 96:065802, 2017.

[SZH83] R Schaeffer, L Zdunik, and P Haensel. Phase transitions in stellar cores. i-equilibrium configurations. *Astron. Astrophys.*, 126:121–145, 1983.

[SZKF19] Masaru Shibata, Enping Zhou, Kenta Kiuchi, and Sho Fujibayashi. Constraint on the maximum mass of neutron stars using GW170817 event. *arXiv e-prints*, 2019. arXiv:1905.03656.

[TC67] K. S. Thorne and A. Campolattaro. Non-Radial Pulsation of General-Relativistic Stellar Models. I. Analytic Analysis for L $\geq$ 2. *Astrophys. J.*, 149:591, September 1967. doi:10.1086/149288

[TC99] S. E. Thorsett and D. Chakrabarty. Neutron Star Mass Measurements. I. Radio Pulsars. *Astrophys. J.*, 512:288–299, February 1999. arXiv:astro-ph/9803260, doi:10.1086/306742

[tH86] Gerard 't Hooft. How Instantons Solve the U(1) Problem. *Phys. Rept.*, 142:357–387, 1986.

[Tho97] Kip S. Thorne. Gravitational radiation: A New window onto the universe. *arXiv:gr-qc/9704042*, 1997.

[TKHS13] I. Tews, T. Krüger, K. Hebeler, and A. Schwenk. Neutron matter at next-to-next-to-next-to-leading order in chiral effective field theory. *Phys. Rev. Lett.*, 110(3):032504, 2013.

[Typ16] S. Typel. Variations on the excluded-volume mechanism. *Eur. Phys. J. A*, 52:16, 2016.

[VP97] R. Venugopalan and M. Prakash. Thermal properties of interacting hadrons. *Nucl. Phys. A*, 546:718, 1997.

[Wal74] J. D. Walecka. A theory of highly condensed matter. *Ann. Phys.*, 83 (2):491, 1974.

[Wil85] J. R. Wilson. Supernovae and Post-Collapse Behavior. In J. M. Centrella, J. M. Leblanc, and R. L. Bowers, editors, *Numerical Astrophysics*, page 422, 1985.

[WITJ18] W. Wei, B. Irving, Klähn T., and P. Jaikumar. Camouflage of the Phase Transition to Quark Matter in Neutron Stars. *arXiv:*, 1811.09441, 2018.

[WMR18] Lukas R. Weih, Elias R. Most, and Luciano Rezzolla. On the stability and maximum mass of differentially rotating relativistic stars. *Mon. Not. R. Astron. Soc.*, 473:L126, 2018.

[X+19] Y. Q. Xue et al. A magnetar-powered x-ray transient as the aftermath of a binary neutron-star merger. *Nature*, 568:198–201, 2019.

[ZBR+18] Francesco Zappa, Sebastiano Bernuzzi, David Radice, Albino Perego, and Tim Dietrich. Gravitational-wave luminosity of binary neutron stars mergers. *Phys. Rev. Lett.*, 120:111101, 2018.

[ZL18] Tianqi Zhao and James M. Lattimer. Tidal deformabilities and neutron star mergers. *Phys. Rev. D*, 98:063020, Sep 2018. doi:10.1103/PhysRevD.98.063020

[ZP16] Xilin Zhang and Madappa Prakash. Hot and dense matter beyond relativistic mean field theory. *Phys. Rev. C*, 93:055805, May 2016. doi:10.1103/PhysRevC.93.055805

Thesis and Dissertation Services